Solar Energy Conversion via Photovoltaics and Photocatalysis

by

Won Jun Jo

S.B. Chemical Engineering, Pohang University of Science and Technology, 2011

Submitted to the Department of Chemical Engineering
in partial fulfillment of the requirements for the degree of

Doctor of Philosophy in Chemical Engineering

at the

MASSACHUSETTS INSTITUTE OF TECHNOLOGY

January 2017 [FEB 2017]

Signature redacted

Author:_____
Department of Chemical Engineering
January 15, 2017

Signature redacted

Certified by:_____
Karen K. Gleason
Associate Provost and Alexander and I. Michael Kasser Professor of Chemical Engineering
Thesis Supervisor

Signature redacted

Accepted by:_____
Daniel Blankschtein
Graduate Officer, Department of Chemical Engineering

Solar Energy Conversion via Photovoltaics and Photocatalysis

by

Won Jun Jo

Submitted to the Department of Chemical Engineering
in partial fulfillment of the requirements for the degree of
Doctor of Philosophy in Chemical Engineering

ABSTRACT

Due to the forthcoming shortage of natural resources, the demand for more efficient and eco-friendly chemical processes for the conversion of energy and matter, especially with respect to carbon management, is growing rapidly. Therefore, a search for high-performance solar energy conversion systems to end the current carbon economy era is of paramount importance in both academic and industrial sectors. In this regard, we have studied organic photovoltaics and solar water splitting by using oCVD (Oxidative Chemical Vapor Deposition) polymers and doping-treated bismuth vanadate ($BiVO_4$), respectively.

oCVD is a solvent-free conformal vacuum-based technique to enable thin-film fabrication of insoluble polymers at moderate vacuum (~ 0.1 Torr) and low temperature (25 – 150 °C). Moreover, oCVD carries the well-cited processing benefits of vacuum processing, such as parallel and sequential deposition, well-defined thickness control, large-area uniformity, and inline integration with other standard vacuum processes (e.g., vacuum thermal evaporation). Based on the abovementioned technical advantages from oCVD, polyselenophene and poly(3,4-dimethoxythiophene) have been successfully applied to organic photovoltaics.

Cost-effective solar hydrogen production requires catalytic materials that have earth-abundant element composition, suitable photoelectrochemical properties, and broad technological applicability. To create this versatile catalytic material, controlling the catalyst's atomic structure is of primary importance since their functionalities (e.g., electronic band structure, catalytic activity, chemical stability, etc.) are governed by its atomic structure. According to the strategy, $BiVO_4$'s atomic structure has been engineered via phosphorus, indium and molybdenum doping. The improved photocatalytic behavior of doping-treated $BiVO_4$ has been studied within experimental and computational domains.

Thesis Supervisor: Karen K. Gleason
Title: Associate Provost and Alexander and I. Michael Kasser Professor of Chemical Engineering

Acknowledgments

I would like to express my sincere appreciation to all of those who have helped me complete my doctoral study at MIT with their generous help, guidance, support, and encouragement. Above all, I want to thank my thesis advisor, Professor Karen Gleason. She has been a fantastic advisor giving me significant guidance and encouragement for achievement, creativity, and hard work. I also want to thank my committee members, Professor Vladimir Bulović, Professor Michael Strano, and Professor Tonio Buonassisi. They offered useful support, comments, and questions that helped me conduct more original and insightful studies.

It has been wonderful to work with such a great researchers in the Gleason research group. In particular, David Borrelli was incredibly helpful. From when I joined the group to when he graduated, he generously dedicated a significant amount of time training and guiding me. I appreciate Sunghwan Kim, Do Han Kim, and Asli Ugur Katmis for many insightful discussions. I also would like to thank the administrative assistants in the Department of Chemical Engineering: Gwen Wilcox, Anthee Traver, Alina Haverty, and Suzanne Maguire.

I am truly grateful to all of the collaborators: Joel Jean, Parick Brown, Justin Nelson, Professor Silvija Gradečak, Dr. Sehoon Chang, Professor Jae Sung Lee, Dr. Hyun Joon Kang, Dr. Ki-jeong Kong, Dr. Yun Seog Lee, Hunmin Park, Younghye Lee. I am also extremely thankful to my family: Mom, Dad, Moon Chul, and Won Hyung. I have felt their support from near and far. Special thanks as well to my friends: Jae Jung Kim, Hye Jin Kim, Evan Piephoff, Kyung Tae Kang, Jongmin Park, Young Kwan Kim, Bonggeun Shong, Shinhyun Choi, Intak Jeon, Yun Seob Kim, and Dong Hwan Kim.

This work was supported by Eni S.p.A under the Eni-MIT Solar Frontiers Center and by a Samsung fellowship from the Samsung Foundation of Culture. This work was also supported in part by the U.S. Army Research Laboratory and the U.S. Army Research Office through the Institute for Soldier Nanotechnologies, under contract number W911NF-13-D-0001.

Table of Contents

List of Figures

List of Tables

List of Acronyms and Abbreviations

AFM	atomic force microscopy
Ag	silver
BCP	bathocuproine
$BiVO_4$	bismuth vanadate
C_{60}	fullerene
CVD	chemical vapor deposition
DBP	dibenzo-tetraphenyl-periflanthene
ε_0	vacuum permittivity
e^-	electron
E_B	binding energy
E_g	band gap energy
EHS	Environment health and safety
EQE	external quantum efficiency
$FeCl_3$	iron(III) chloride
FF	fill factor
FTIR	Fourier transform infrared spectroscopy
h^+	hole
HTL	hole transporting layer
HOMO	highest occupied molecular orbital
ITO	indium tin oxide
I_{SC}	short circuit current
J_{SC}	short-circuit current density
k (ε_r)	dielectric constant (relative permittivity)
LUMO	lowest unoccupied molecular orbital
MoO_X	thermally evaporated molybdenum oxide
oCVD	oxidative chemical vapor deposition
OPV	organic photovoltaic device
PCE	power conversion efficiency
PDMT	poly(3,4-dimethoxythiophene)
PEDOT:PSS	poly(3,4-ethylenedioxy-thiophene):polystyrene sulfonate
PSe	polyselenophene
PT	polythiophene
UV-Vis	ultraviolet-visible spectroscopy
V_{OC}	open circuit voltage

CHAPTER ONE

Introduction

Abstract

Due to the forthcoming shortage of natural resources, the demand for more efficient and eco-friendly chemical processes for the conversion of energy and matter, especially with respect to carbon management, is growing rapidly. Therefore, a search for high-performance solar energy conversion systems as carbon-neutral energy solutions is of paramount importance in both academic and industrial sectors. In this regard, we have studied organic photovoltaics and solar water splitting by using oCVD (Oxidative Chemical Vapor Deposition) polymers and doping-treated bismuth vanadate ($BiVO_4$), respectively. The insights gained from this work will provide an important contribution to the general understanding of how to design and develop innovative energy materials and fully operational devices, which play important roles for future energy technologies.

1.1. Motivation

The demand for more efficient and eco-friendly energy conversion technology is growing rapidly, especially in response to global warming and natural resource depletion. Therefore, high-performance solar energy conversion systems toward a fossil fuel-free and sustainable future are of paramount importance in both academia and industry. In this regard, we have conducted a variety of studies to design and develop novel materials and fully operational devices that convert the energy from sunlight into stored energy in the form of chemical fuels or electricity. The solar energy conversion in this study was achieved through organic photovoltaics and photocatalysis, main principles of which are described in the following sections, respectively.

1.2. Organic Photovoltaics

Organic Photovoltaics has been attracting great attention as one of the most promising energy technologies to convert sunlight energy into electricity, because it carries an excellent combination of advantages for commercialization such as low build-up cost, flexibility, large area applicability, and lightweight. However, organic photovoltaic devices (OPVs) are not efficient and stable enough to achieve commercialization worldwide.[1,3] The following five important processes should be improved to produce OPVs with higher power conversion efficiency (PCE):

1. Absorption of light and generation of excitons
2. Diffusion of excitons to an active interface
3. Charge separation
4. Charge transport
5. Charge collection

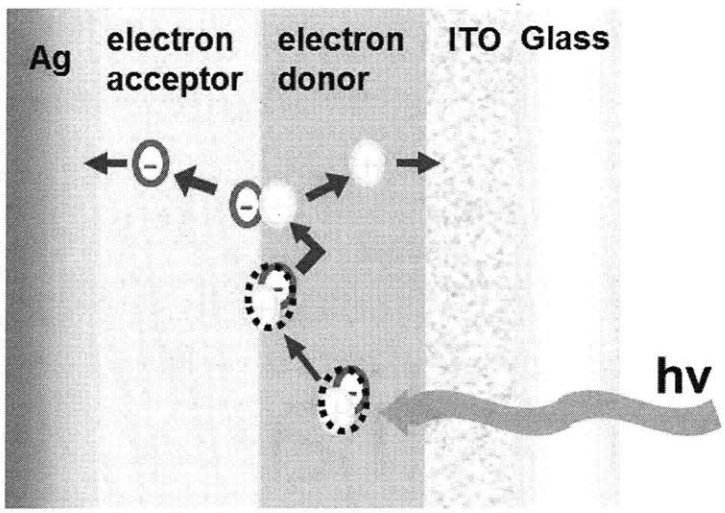

Figure 1-1. Schematic drawing of how OPVs to convert sunlight energy into electricity

As **Figure 1-1** describes, the photoactive materials (donor and acceptor materials) are sandwiched between two metallic electrodes to fabricate working OPVs. One of metallic electrodes needs to be transparent for light absorption. Illumination through the transparent electrode (ITO) activates a donor material (in blue) to create an exciton. The exciton diffuses to the interface between the donor material and an acceptor material (in green), and it is decomposed to a hole and an electron. The hole and electron are transported toward anode (ITO) and cathode (Ag), respectively. When the hole and electron are collected by anode and cathode, electric current can be generated.

In general, the five central steps demand different conditions for their optimization. For "absorption of light and generation of excitons", the donor material needs to have high absorption coefficient and small bandgap energy (E_g). For "diffusion of excitons to an active interface", the longer exciton diffusion length is favorable. For "charge separation", proper difference in electron affinity between the donor materials and acceptor materials is required. For "charge transport", the film thicknesses of photoactive materials need to be manipulated according to their charge mobility. Since the charge mobility of organic semiconductors is much

lower than their inorganic counterparts, the proper film thickness is usually smaller than 50 nm. However, it should be noted that when the donor material film thickness is reduced, the light absorption resulting in the formation of excitons also decreases. In other words, there is a trade-off between the two processes, which are "absorption of light and generation of excitons" and "charge transport." Thus, the absorption coefficient has to be high to optimize the both processes at the same time. For "charge collection", high-quality ohmic contact should be established.[3]

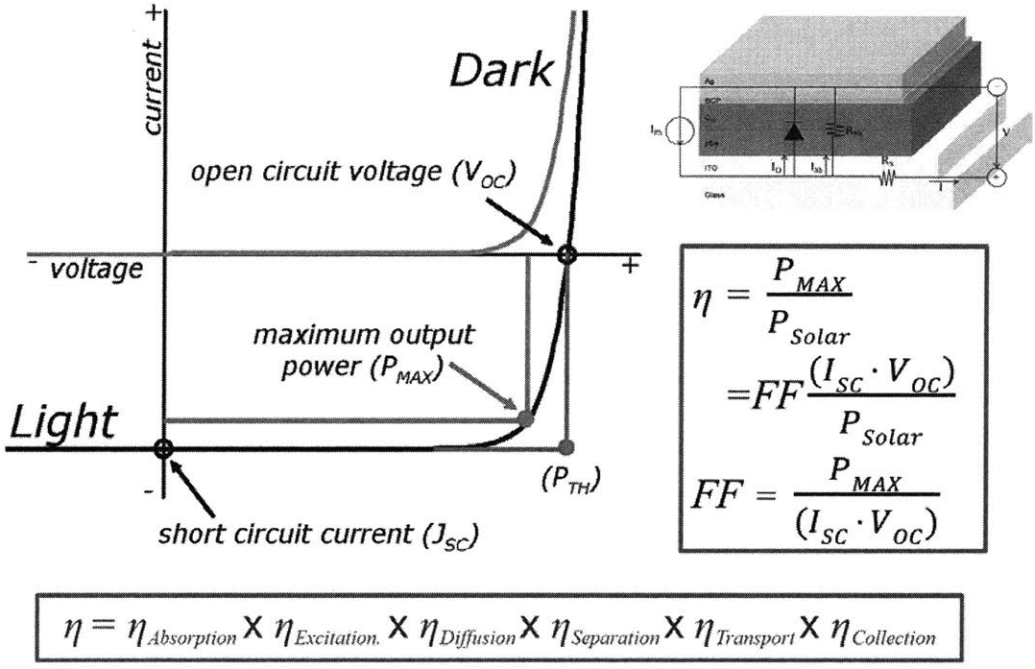

Figure 1-2. Current-voltage (I-V) curve of OPV cells

The PCE of OPVs can be evaluated by multiplying the efficiencies of the five steps for solar to electricity conversion, or using a graphical method shown in **Figure 1-2**. The product of fill factor (FF), short-circuit current (I_{SC}), and open-circuit voltage (V_{OC}) over incident power (P_{Solar}) is equal to the PCE. Based on the aforementioned principle of how OPVs work, their PCE and stability were upgraded by using oxidative chemical vapor deposition (oCVD). This is a

platform technology for this research, and its main technical benefits are explained in the next section.

1.3. Oxidative Chemical Vapor Deposition

oCVD is a versatile solvent-free vacuum technique, which Gleason and coworkers developed for the purpose of insoluble polymer thin-film fabrication.[1-3] Although there are many suitable insoluble polymers for organic electronics, their application to OPVs are limited due to their insolubility. To address these challenges, we employed oCVD (oxidative chemical vapor deposition) as a key polymer thin-film fabrication strategy.

oCVD is a vacuum (~0.15 Torr) technology enabling polymer synthesis, thin film deposition, and doping in a single operation below 150 °C. During the oCVD process, the monomer (blue vapor in **Figure 1-3**) and oxidant precursors (yellow vapor in **Figure 1-3**) are both diffused into the oCVD reactor chamber through the vapor phase. Hence, any solvents are not needed to deliver the resulting polymer and its precursors. In other words, there is no need to consider compatibility of the substrate with solvents. This key differentiator from solution-based synthesis approaches makes oCVD substrate-independent as well as scalable.[1-3] Moreover, the use of a shadow mask during the oCVD process enables patterning of the polymer thin films, a technique termed "vapor printing". In particular, this method is useful in manufacturing various polymer thin films that have desirable patterns for playing different roles in organic solar cells (OSCs). For example, we made PEDOT and polyselenophene thin films with dissimilar patterns to serve OSCs as flexible electrodes and donor layers, respectively.[1-3]

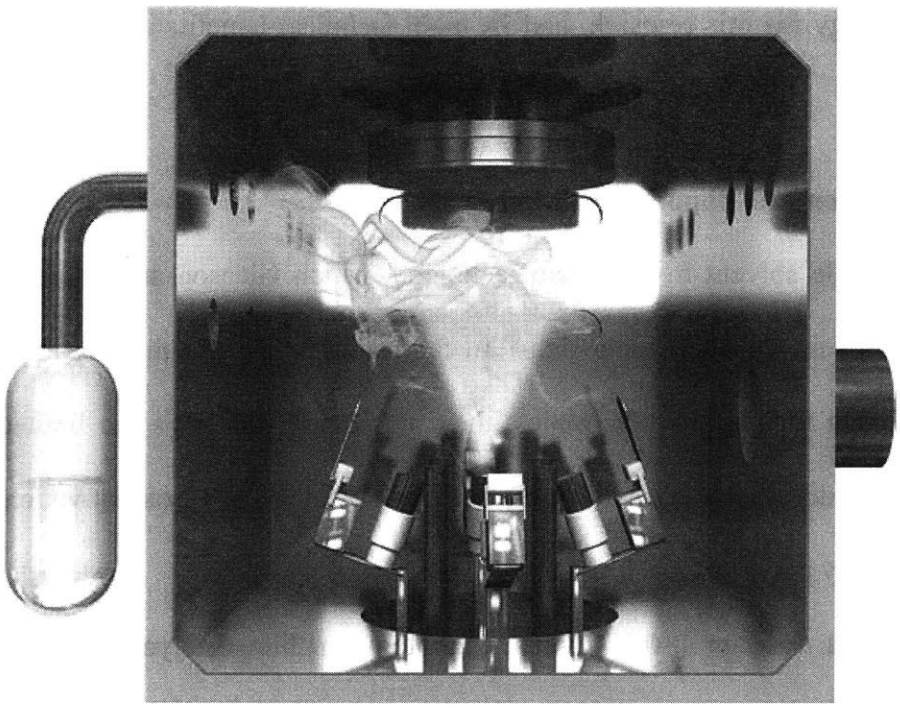

Figure 1-3. Schematic illustration of oCVD reactor

The general oCVD operation consists of the following four steps. First, oxidant powder (ex. $FeCl_3$) in a crucible vaporizes via heating under vacuum condition. Second, monomer vapor flows into an oCVD reactor chamber from an external monomer jar. Third, monomer vapor reacts with oxidant vapor to form polymers on a wide array of substrates. Finally, polymer synthesis and deposition are simultaneously achieved on the substrates. According to the application-specific goals, we can tune the properties of the resulting polymer thin films by manipulating the operational conditions of oCVD, such as the reactor chamber temperature, substrate temperature, and polymer film thickness.

1.4. Photocatalysis

Hydrogen has been recognized as one of the most promising energy carriers for the future, because it can generate enormous energy by clean combustion chemistry without any greenhouse

gas emissions. In order for hydrogen to play a key role as the next-generation energy carrier, it is required to produce hydrogen in a sustainable manner.[4-5] Water splitting under visible light irradiation is an ideal route to cost-effective, large-scale, and sustainable hydrogen production, but it is challenging, because it requires a rare photocatalyst that carries a combination of suitable band gap energy, appropriate band positions, and photochemical stability.

To create this rare photocatalyst, we need to understand the principal mechanism of how solar water splitting is achieved via photocatalysis. **Figure 1-4** illustrates the mechanism, which can be represented by 4-step photochemical reaction as follows: 1) absorbing sun light, 2) generating holes and electrons, 3) oxidizing water molecules into gaseous oxygens and hydrogen ions, and 4) reducing hydrogen ions into gaseous hydrogens. Here, it is noteworthy what is the main difference between photovoltaics and photocatalysis. While, photovoltaics aim to convert the energy in sunlight into electricity, the goal of photocatalysis is to store the energy energy in the form of chemical fuels such as H_2 and CH_3OH.

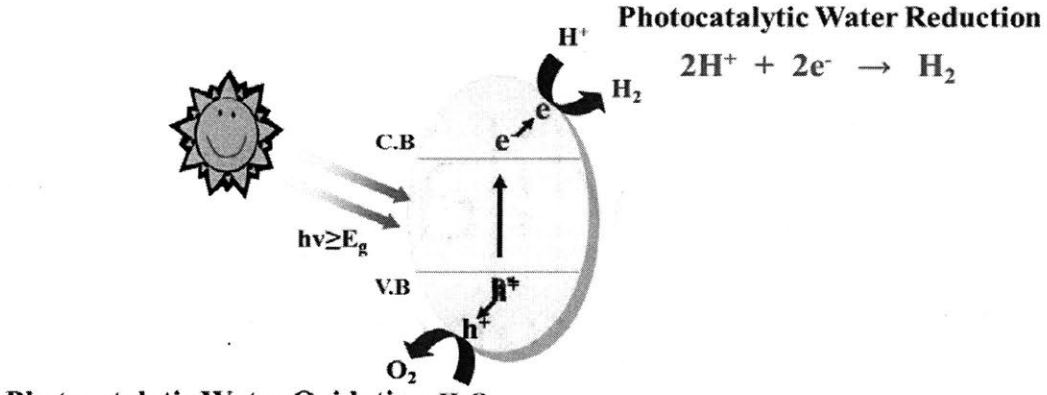

Photocatalytic Overall Water Splitting

$$H_2O + hv \rightarrow H_2 + \tfrac{1}{2}O_2 \quad (E = -1.23eV)$$

Figure 1-4. Schematic drawing of how photocatalysts split water into H_2 and O_2

Taking into account the abovementioned mechanism, we engineered the band edges of $BiVO_4$ by simultaneously substituting In^{3+} for Bi^{3+} and Mo^{6+} for V^{5+} in the host lattice of monoclinic $BiVO_4$, which induced partial phase transformation from pure monoclinic BiVO4 to a mixture of monoclinic $BiVO_4$ and tetragonal $BiVO_4$. This phase transformation sequentially leads to unit cell volume growth, compressive lattice strain increase, conduction band edge uplift, and band gap widening. Consequently, the band-edge engineered $BiVO_4$ is able to split water into H_2 and O_2 under visible light, without using any noble metals for the first time. Chapter 4 will provide a more detailed discussion about this work.

1.5. Scope of Thesis

The objective of this project is to advance the science of photovoltaics and photocatalysis for solar energy conversion. For photovoltaics, we fabricate and integrate polymer thin films to OPVs by using oCVD. The first two research chapters (Chapter 2 and 3) focus on how oCVD-conjugated polyselenophene and poly(3,4-dimethoxythiophene) work for OPVs as a donor and hole transporter, respectively. For photocatalysis, the electronic band structure of $BiVO_4$ is controlled in the atomic scale through In^{3+}/Mo^{6+} doping, in order to achieve overall water splitting using sunlight energy. This work is discussed in Chapter 4.

In Chapter 2, we have successfully integrated polyselenophene donor layers into organic photovoltaic devices for the first time. By using oCVD technique, polyselenophene thin films are simultaneously synthesized and deposited on various substrates at modest vacuum (~ 0.15 Torr), independent of material solubility and substrate properties. Bilayer heterojunction photovoltaic cells fabricated with the oCVD polyselenophene donor layers resulted in efficiency up to 0.4%. This is the highest efficiency to date achieved by polyselenophene. Furthermore, this work investigates polyselenophene's nature, which is closely linked to organic electronics for the first

time. For example, we have illuminated polyselenophene's HOMO and LOMO levels as well as the regiochemical defect generation mechanism.

Chapter 3 discusses the first demonstration of a neutral hole-transporting polymer, Cl^- doped poly(3,4-dimethoxythiophene) (PDMT). It performs better than a commercial acidic hole-transporting polymer, poly(3,4-ethylenedioxy-thiophene):polystyrene sulfonate (PEDOT: PSS), by raising the J_{SC} (short-circuit current density), FF, and PCE of single-DBP/C_{60}-planar-junction solar cells (DBP: dibenzo-tetraphenyl-periflanthene, C_{60}: fullerene). As a result, we reached the highest PCE record (4.1%) of the DBP/C_{60} solar cells. Moreover, the neutral PDMT hole transporting layer (HTL) dramatically enhances device stability. This allows 83% of initial PCE to be retained after 17 days of storage in a N_2 glove-box. In contrast, the same testing with the acidic PEDOT:PSS HTL results in only 12% retention of initial PCE. Considering that long-term device stability is a linchpin required for commercializing OSCs, the stability achieved with the neutral PDMT HTL is an overwhelming benefit over the acidic PEDOT:PSS HTL.

Chapter 4 investigates In^{3+}/Mo^{6+} doping impacts on monoclinic $BiVO_4$ by combining novel experiments with theory. Specifically, we have developed 'greenish' $BiVO_4$, $Bi_{1-x}In_xV_{1-x}Mo_xO_4$, ($GBVO_x$, x = atom ratio of In and Mo) by simultaneously substituting In^{3+} for Bi^{3+} and Mo^{6+} for V^{5+} in the host lattice of m-$BiVO_4$. This new $GBVO_x$ photocatalyst has a slightly larger band-gap energy ($E_g \sim 2.5$ eV) than usual 'yellow' m-$BiVO_4$ ($E_g \sim 2.4$ eV), as supported by the unique color change to green, and higher (more negative) conduction band than H^+/H_2 potential (0 V_{RHE} at pH 7). Consequently, $GBVO_x$ is able to split water into H_2 and O_2 under visible-light irradiation without using any sacrificial reagents (e.g. CH_3OH or $AgNO_3$). This outcome represents the first example of a pure water-splitting photocatalyst responding to visble light without any noble-metal cocatalyst.

Chapter 5 summarizes finding from each chapters, concludes this thesis, and suggests future work.

1.6. References

[1] A. M. Coclite, R. M. Howden, D. C. Borrelli, C. D. Petruczok, R. Yang, J. L. Yagüe, A. Ugur, N. Chen, S. Lee, W. J. Jo, A. Liu, X. Wang, K. K.Gleason, *Adv. Mater.* **2013**, *25*, 5392.

[2] W. J. Jo, D. C. Borrelli, V. Bulović, K. K. Gleason, J. S. Lee, *Org. Electron.* **2015**, *26*, 55.

[3] W. J. Jo, J. Nelson, S. Chang, V. Bulović, S. Gradečak, M. S. Strano, and K. K. Gleason, *Advanced Materials*, **2016**, 28, 6399-6404.

[4] W. J. Jo, J.-W. Jang, K. Kong, H. J. Kang, J. Y. Kim, H. Jun, K. P. S. Parmar, J. S. Lee, *Angew. Chem. Int. Ed.* **2012**, *51*, 3147.

[5] W. J. Jo, H. J. kang, K. Kong, Y. S. Lee, H. Park, Y. Lee, T. Buonassisi, K. K. Gleason, J. S. Lee, *Proc. Natl. Acad. Sci. U.S.A.* **2015**, *112*, 13774.

CHAPTER TWO

Photovoltaic Effect by Vapor-Printed Polyselenophene

This chapter is adapted and reprinted with permission from: Won Jun Jo, David C. Borrelli, Vladimir Bulović, and Karen K. Gleason, *Photovoltaic Effect by Vapor-Printed Polyselenophene*, **Organic Electronics**, 26, 55-60 (2015).

2.1. Abstract

Polyselenophene (PSe) donor layers are successfully integrated into organic photovoltaic devices (OPV) for the first time. Thin, patterned films of this insoluble semiconductor were fabricated using a vacuum-based vapor-printing technique, oxidative chemical vapor deposition (oCVD) combined with *in-situ* shadow masking. The vapor-printed PSe exhibits a reduced optical bandgap of 1.76 eV and enhanced photo-responsivity in the red compared to its sulfur containing analogue, polythiophene. These relative advantages are most likely explained by selenium's enhanced electron-donating character compared to sulfur. The HOMO level of PSe was determined to be at -4.85 eV. The maximum power conversion efficiency achieved was 0.4% using a bilayer heterojunction device architecture with C_{60} as the donor.

2.2. Introduction

Various solar energy conversion systems have emerged as promising candidates to establish a clean and sustainable energy network.[1-4] Organic solar cells have attracted great attention from the solar energy community due to their potential to enable lightweight, flexible, large-area and cost-effective photovoltaic technology.[5-11] It is essential for further improvements in efficiency to develop new materials carrying a combination of small bandgap, high dielectric constant, and high charge mobility.[12-16]

Previously, many studies focused on creating suitable polymer candidates by using selenophene-based homopolymers and copolymers.[17-23] While these studies found that the selenophene-based polymers are good hole transporting polymers with relatively long wavelength absorption, [17-23] the application of unsubstituted polyselenophene (PSe) has been quite limited. Unsubstituted polymers are known to be more stable because of their densely packed structures preventing oxygen permeation into the polymer bulk.[24,25] The study of PSe

has been limited due to the lack of suitable synthetic methods to create high-quality thin films displaying high charge mobility and stable electrochemical behaviors.[26] However, our previous work successfully fabricating PSe films via oxidative chemical vapor deposition (oCVD) encourages the incorporation of PSe into photovoltaic devices.[13]

Unlike other standard methods, oCVD offers an attractive substrate-independent synthesis route to insoluble or infusible polymers as it is a solvent-free, vacuum-based technique.[13,27,28] It is able to synthesize and deposit conjugated polymers simultaneously on a wide range of substrates at low temperature (25 ~ 100 °C) in a controllable fashion applying *in-situ* shadow masking. Moreover, oCVD still maintains vacuum processing benefits, such as well-defined thickness control and uniformity, conformal coverage, parallel and sequential deposition, and inline convertibility with other standard vacuum processes (e.g., thermal evaporation).[13,27,28] Recently, this versatile technique has advanced materially in its applicability to secure a facile path to the deposition of diverse semiconducting or conducting conjugated polymers. These polymers can play central roles in organic electronic and optoelectronic devices. [27]

Here, we report the photovoltaic effect by PSe, employing a novel, yet simple, vacuum-based vapor-printing technique, which represents a combination of oCVD process with shadow masking.[27] The resulting semiconducting PSe is applied into bilayer heterojunction solar cells as an electron donor with an electron accepting C_{60}. This study results in a maximum power conversion efficiency (η_p) of 0.4%, which is the first demonstration of PSe utilized for organic photovoltaics.

2.3. Experimental Methods

2.3.1. Polyselenophene Depositions

When substrates were indium tin oxide (ITO) coated glasses for the photovoltaic device fabrication, the polymer film was prepared by the vapor printing method. Otherwise, the basic oCVD process without shadow masking was employed to prepare the polymer film. The custom-built oCVD reactor consists of a vacuum chamber connected to monomer inlet ports and an exhaust to a pump. At the bottom and top of the chamber, a heating crucible for an oxidant and an inverted stage for substrates are placed, respectively.

During the deposition, the reactor body and the chamber pressure were maintained at 80 °C and 150 mTorr, respectively. Iron(III) chloride ($FeCl_3$, 97%, Sigma–Aldrich) and selenophene (97%, Sigma–Aldrich) were used as the oxidant and monomer without any further purification. $FeCl_3$ was sublimed at 330 °C. Polymer film thickness was controlled by the deposition time. Vapor-phase selenphene monomer was introduced into the reactor from a monomer jar. The jar was maintained at 25 °C and a needle valve was used to render the monomer vapor flow rate constant at around 1 sccm. After deposition, the films were rinsed in methanol (≥ 99.9%, Sigma–Aldrich) for 10 min to remove reacted oxidant.

2.3.2. Polymer Characterization

Fourier transform infrared (FTIR) measurements of PSe films on silicon wafers were performed on a Nexus 870, Thermo Electron Corp. spectrometer. The atomic compositions of the films were estimated by X-ray photoelectron spectroscopy (XPS) a PHI VersaProbe II (Physical Electronics). The film thicknesses were examined using a Veeco Dektak 150 surface profilometer. The sheet resistance of the films was measured with a Jandel four-point probe in air. Conductivity values were calculated using the measured sheet resistivity and thickness. Morphology analysis for PSe films were accomplished using an Agilent Technologies AFM in

tapping mode with a Bruker Si cantilever having a tip frequency of 330 kHz. The UV–vis spectra of PSe films on bare glasses were gained utilizaing a Varian Cary 5000 UV–vis spectrophotometer. To evaluate absorption coefficient of the films, transmission and reflection spectra were measured. For the reflection spectra, a specular reflectance accessory and an Al standard reference mirror (ThorLabs) were used.

To identify the highest occupied molecular orbital (HOMO) level of the oCVD PSe, cyclic voltammetry (CV) were conducted in a standard three-electrode cell containing tetrabutylammonium hexafluorophosphate (0.1 M) in acetonitrile as the electrolyte under a nitrogen atmosphere. The PSe film on an ITO-coated glass Ag/AgNO3 (0.01 M in acetonitrile), a Pt mesh attached to a Pt wire worked as the working electrode, reference electrode, and counter electrode, respectively. Current-voltage data were collected at a scan rate of 100 mV s^{-1} with ferrocene/ferrocenium (Fc/Fc^{+}) redox couple to calibrate the Ag/Ag^{+} reference electrode, and analyzed with a 660D potentiostat (CH Instruments).

2.3.3. Device Fabrication and Characterization

The photovoltaic devices were fabricated on 75 nm patterned ITO-coated glasses (Thin Film Devices, 50Ω/sq), cleaned by solvents (2 x DI water, 2 x acetone, and 2 x isopropanol) followed by 30 s of O_2 plasma (100W, Plasma Preen, Inc.). As described above, PSe films having different thicknesses were simultaneously synthesized and deposited on the substrates via oxidative polymerization, and then rinsed in methanol for 10 min to remove reacted oxidant. After the oCVD photoactive donor layer deposition, C_{60} (99.9%, sublimed, Sigma–Aldrich), purified once by vacuum train sublimation, bathocuproine (BCP, from Luminescence Technology Corp.), and Ag (Alfa Aesar, 1–3 mm shot, 99.9999%) were thermally evaporated at

a rate of 0.1 nm/s. C_{60} (20 ~ 40 nm), BCP (7.5 nm), and Ag (100 nm) were used as electron acceptor, exciton blocking layer, and cathode, respectively. The Ag cathode was deposited through a shadow mask for each device to obtain the well-defined device area, 1.21 mm^2, which is estimated from the overlapped area between Ag cathode and ITO anode.

Current density-voltage (J-V) measurements were conducted in nitrogen atmosphere, and recorded by a Keithley 6487 picoammeter. One sun of air mass 1.5 G (AM 1.5 G) irradiation (100 mW/cm^2) was generated by 1 kW xenon arc-lamp (Newport 91191) filtered by an AM 1.5G filter. The solar simulator intensity was estimated using a calibrated silicon photodiode. The external quantum efficiency (EQE) spectrum was recorded by a Stanford Research Systems SR830 lock-in amplifier. A focused monochromatic beam of variable wavelength light was provided by an Oriel 1 kW xenon arc lamp equipped with an Acton 300i monochromator and chopped at 43 Hz. The incident monochromatic light intensity was evaluated using a Newport 818-UV calibrated silicon photodiode.

2.4. Results and Discussion

2.4.1. Polyselenophene synthesis and characterization

Based on a previous study, PSe is simultaneously synthesized and deposited on a variety of substrates from vapor-phase selenophene monomer and sublimed $FeCl_3$ oxidant.[13] The overall oxidative polymerization with sublimated $FeCl_3$ is illustrated in **Figure 2-1**. Over oxidation makes the polymer conductive, the final state in **Figure 2-1**, by forming polarons and bipolarons.[29] As shown above, the oCVD process results in the conductive blue PSe film, where cations are charge balanced by counter anions. The conductivity of the doped PSe film was

evaluated to be from 2.6 (104.7 nm) to 35.4 S/cm (181.5 nm), roughly proportional to the film's thickness.

A methanol-rinse treatment causes the film to become semiconducting and go through an immediate color change to red. The conductivity of the PSe after rinsing was below the detection limit of the measurement system (< 10^{-4} S/cm). The observed changes in conductivity and color are entirely consistent with previous reports, and indicate the rinsing treatment dedopes the oCVD PSe.[13,28] The dedoped state of the PSe is further confirmed by XPS atomic composition measurement. The rinsed PSe film does not have any elements (Fe and Cl) from the oxidizing agent, but includes C and Se at a ratio of 5.7 to 1. The FTIR spectrum of the rinsed PSe film in **Figure 2-2a** also matches well with an earlier reported result.[13] Morphology of the rinsed PSe film was investigated using AFM. As **Figure 2-2b** illustrates, oCVD-processed PSe surface is not completely flat, but has an acceptable level of roughness. Specifically, the root mean square (RMS) roughness value is 17.0 nm.

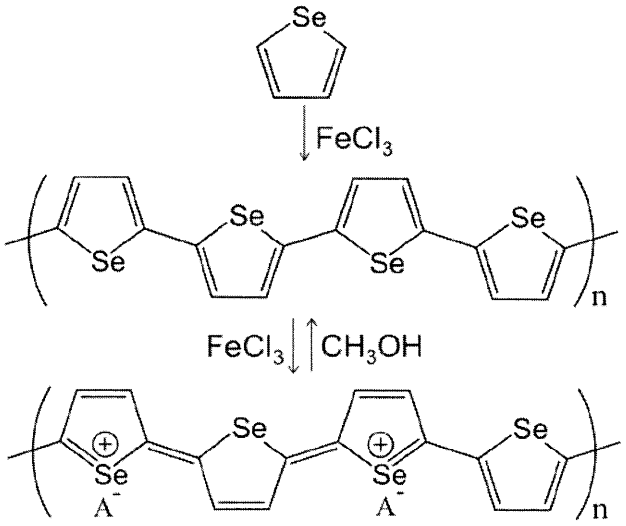

Figure 2-1. Synthetic route from selenophene to polyselenophene via oCVD.

(a)

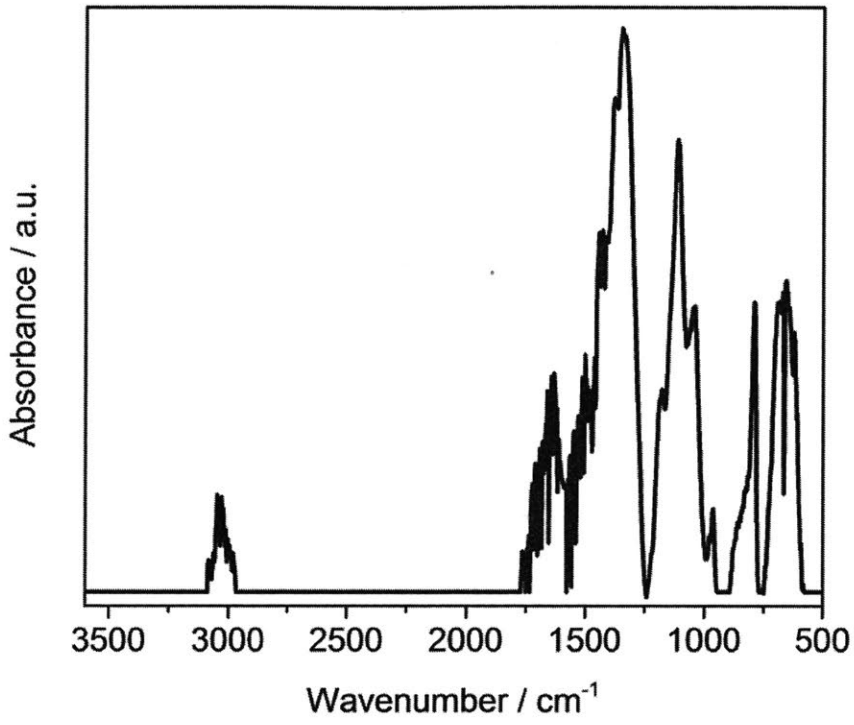
Absorbance / a.u.
3500
3000
2500
2000
1500
1000
500
Wavenumber / cm-1

(b)

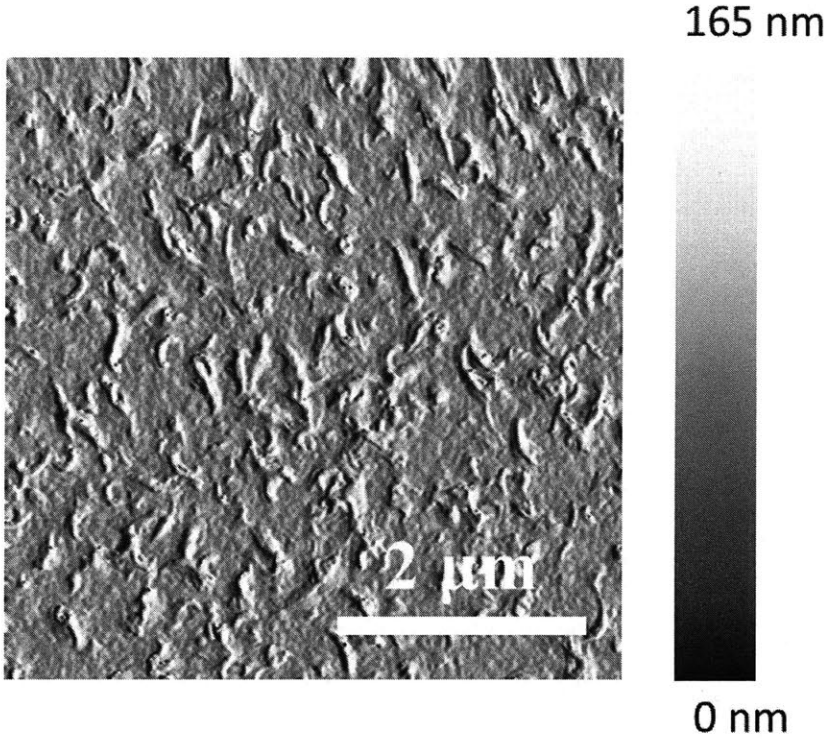
165 nm
2 µm
0 nm

(c)

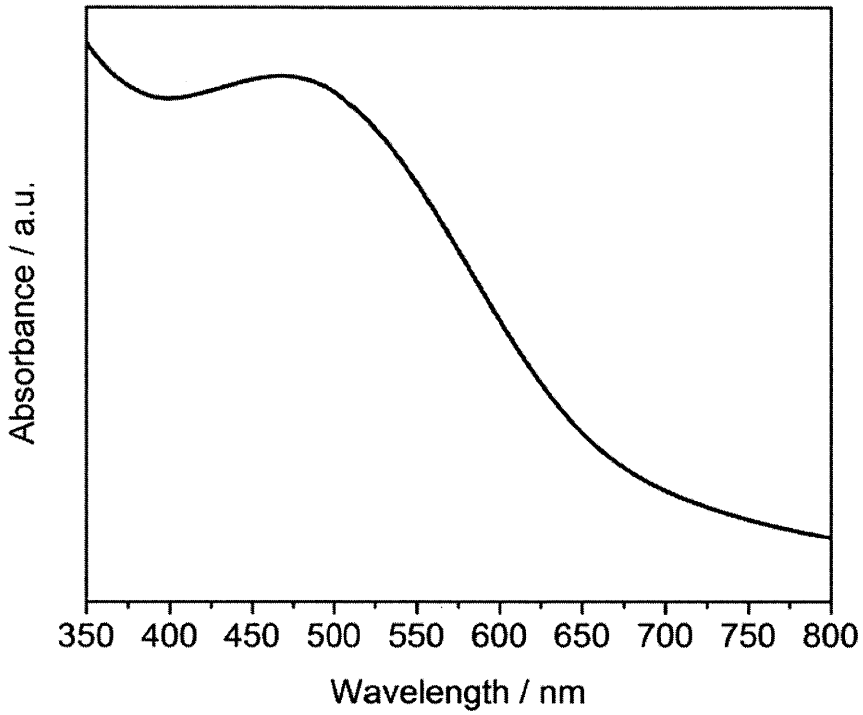

Figure 2-2. (a) FTIR spectrum (b) AFM topography image (c) UV-Vis absorption spectrum of oCVD polyselenophene film

2.4.2. Energy level alignment

The UV-Vis absorption spectrum in **Figure 2-2c** reveals that the onset of optical absorption by PSe appears at 705 nm, corresponding to the optical bandgap of 1.76 eV. To determine the HOMO level of PSe, cyclic voltammetry (CV) was used according to the standard three-electrode setup as described in the section 2.3.2. The resulting CV curve for PSe is shown in **Figure 2-3a**. Based on the curve, the HOMO level is located following previously stated procedures.[28,30] The onset of the oxidation peak is -0.25 V vs Fc/Fc^{+}. The HOMO is then

calculated by the following equation, assuming the redox potential of Fc/Fc^+ is – 5.1 eV relative to vacuum.[30]

$$E_{HOMO} = -(E_{[oxidation\ onset\ vs\ Fc/Fc+]} + 5.1)\ (eV) \quad (1)$$

The calculated HOMO level is -4.85 eV, and the lowest unoccupied molecular orbital (LUMO) level of PSe is determined to be -3.09 eV by adding the optical bandgap of 1.76 eV to the HOMO. Taking the estimated HOMO and LUMO into account, the energy level diagram of PSe solar cells is drawn in **Figure 2-3b**.

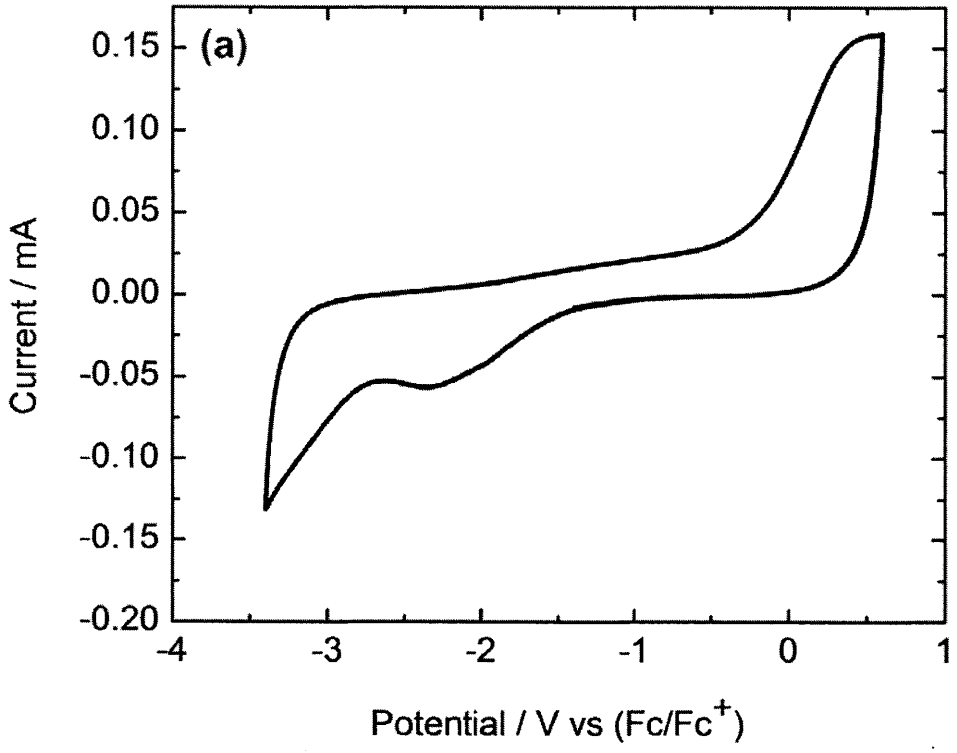

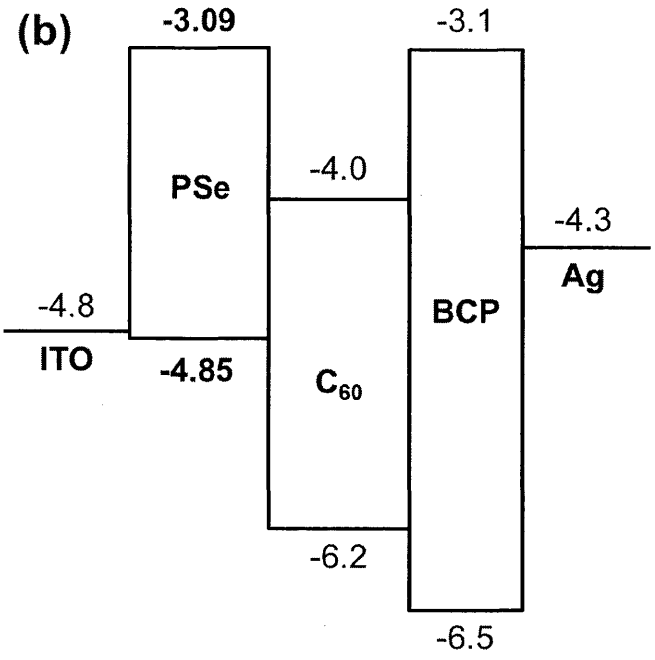

Figure 2-3. (a) Cyclic voltammetry of oCVD polyselenophene film on an ITO electrode. (b) Schematic energy level alignment of oCVD polyselenophene solar cells.

2.4.3. Photovoltaic device performance

To investigate the photovoltaic effect by vapor-printed PSe, we employed a single bilayer heterojunction architecture, as demonstrated in **Figure 2-4**, consisting of the ITO anode substrates, electron donating PSe, electron accepting C_{60}, exciton blocking BCP, and top capping Ag cathode. We also explored a range of thicknesses of the C_{60} and PSe layers to further understand how the two layers affect the device performance as well as to optimize that. **Figure 2-5** displays how the performance varies with C_{60} layer thickness under the fixed PSe layer thickness (70 nm). The optimum C_{60} layer thickness is 30 nm, a finding in agreement with a previous report.[28]

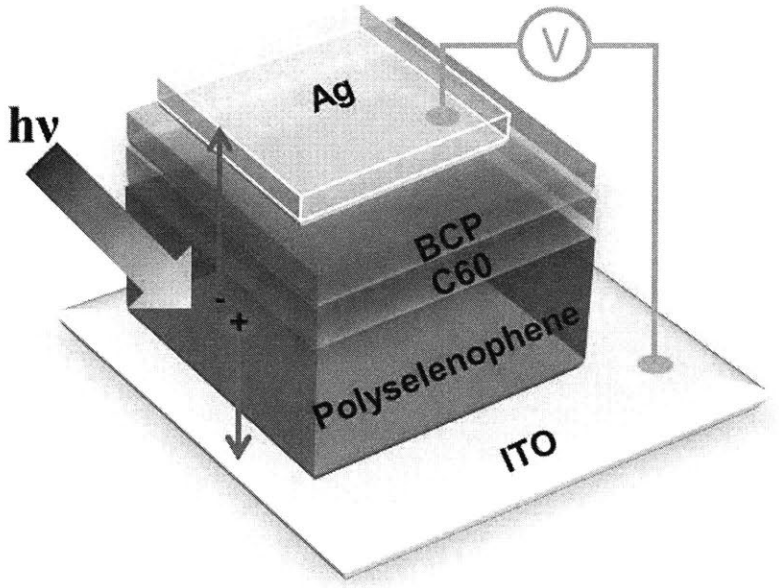

Figure 2-4. Single bilayer heterojunction architecture of oCVD polyselenophene solar cells

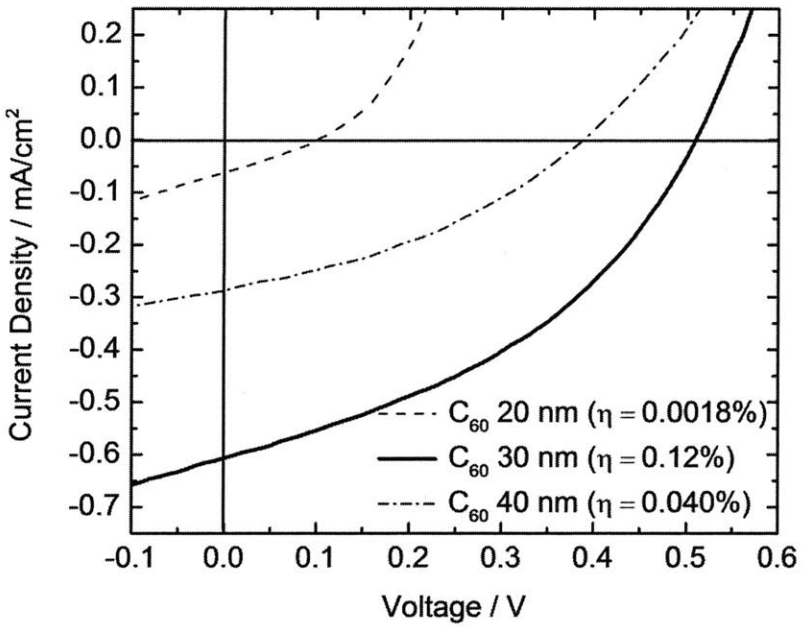

Figure 2-5. Representative J-V curves for varying C_{60} thickness with 70 nm of oCVD polyselenophene layer.

The change in short-circuit current (J_{SC}) with C_{60} layer thickness is mainly due to the variation in optical interference patterns within the device, as the reflective Ag interface moves along with C_{60} layer thickness.[31] For example, the reflective interface is displaced farther from the PSe/C_{60} interface with increasing C_{60} layer thickness. Considering the device architecture, the optical electric field for shorter wavelengths matched with C_{60} absorption peak is expected to be maximized closer to the reflective interface, whereas the field for longer wavelengths corresponding to PSe absorption peak is likely to reach its peak farther from the interface. In this sense, the alteration in C_{60} layer thickness should have an impact on the optical electric field distribution inside the device and thus exciton generation in the C_{60} and PSe layers, closely linked to J_{SC}.

The representative J-V curves for varying PSe layer thicknesses are shown in **Figure 2-6a**. The optimized device with 60 nm PSe and 30 nm C_{60} layers exhibits η_p = 0.4%, open-circuit voltage (V_{OC}) = 0.554 V, J_{SC} = 2.18 mA/cm^2, and fill factor (FF) = 0.33. OPVs utilizing polythiophene, PSe's sulfur-containing analogue, by oCVD were previously studied.[27] It should be noted that the best PSe layer thickness (60 nm) is much thicker than oCVD polythiophene's optimal thickness (25 nm).[28] A comparison of PSe's absorption coefficient (α_{PSe}) with polythiophene's (α_{PT}) illuminates why there is the difference in the optimum thickness. As **Figure 2-6b** depicts, while α_{PSe} is slightly higher than α_{PT} for longer wavelengths than 625 nm, α_{PSe} is significantly lower than α_{PT} in the other region. This suggests PSe film should be thicker than PT film to obtain sufficient light absorption for exciton generation, which is supported by Beer-Lambert equation.

(a)

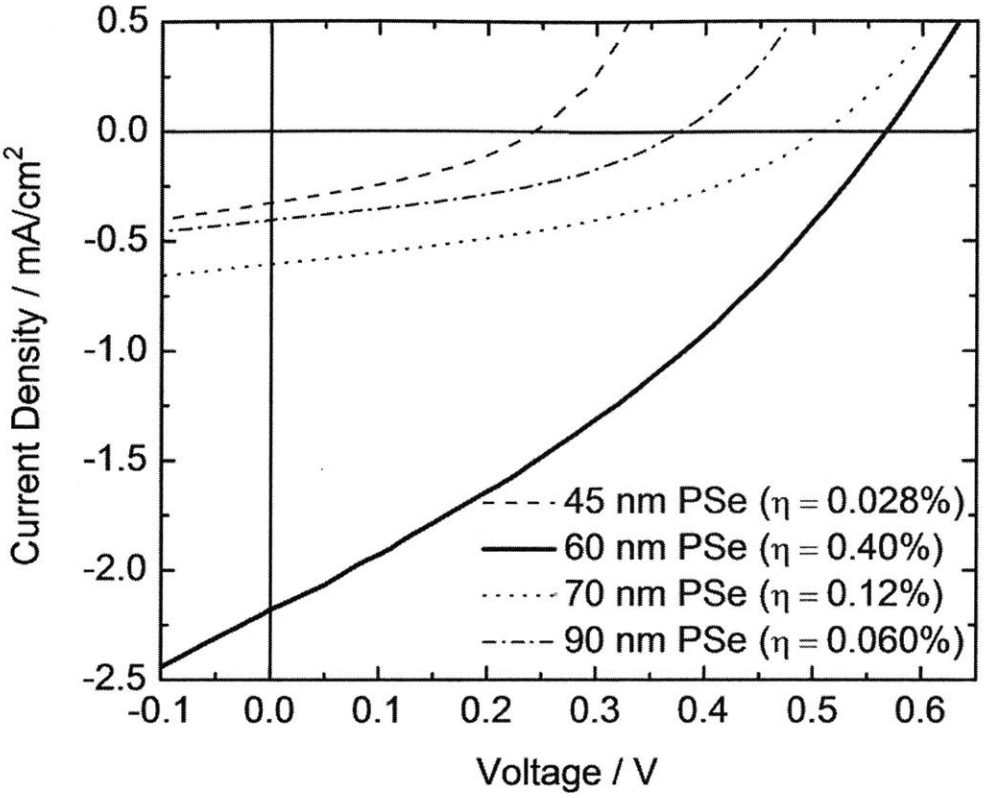
0.5
0.0
-0.5
-1.0
-1.5
-2.0
-2.5
-0.1
0.0
0.1
0.2
0.3
0.4
0.5
0.6
Current Density / mA/cm^2
Voltage / V
45 nm PSe (η = 0.028%)
60 nm PSe (η = 0.40%)
70 nm PSe (η = 0.12%)
90 nm PSe (η = 0.060%)

(b)

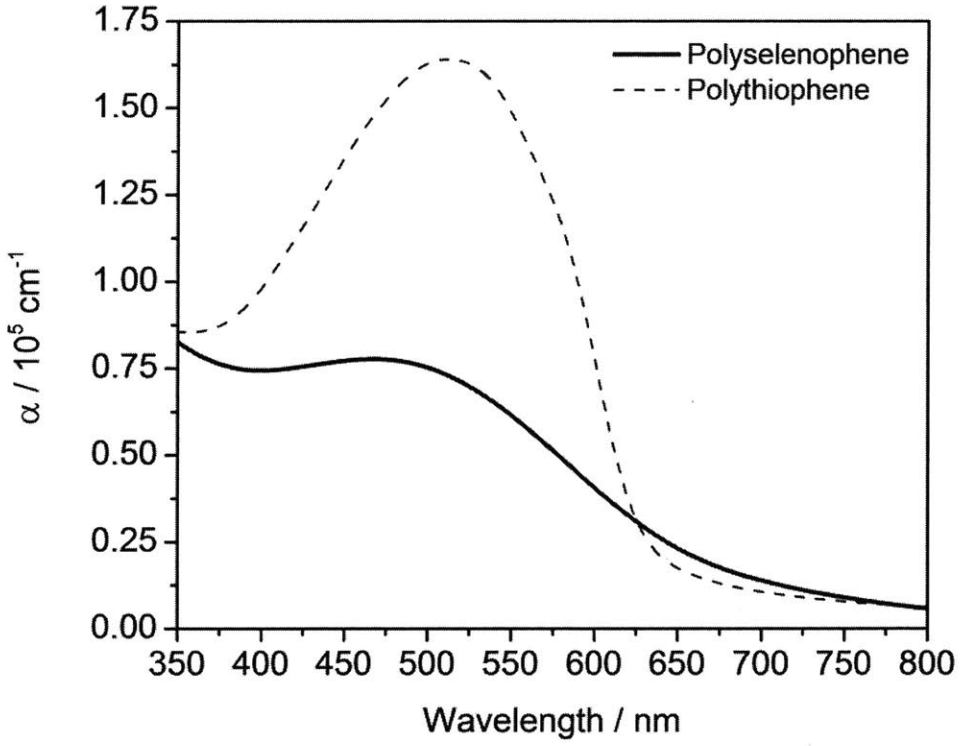
1.75
1.50
1.25
1.00
0.75
0.50
0.25
0.00
350
400
450
500
550
600
650
700
750
800
α / 10^5 cm^{-1}
Wavelength / nm
Polyselenophene
Polythiophene

(c)

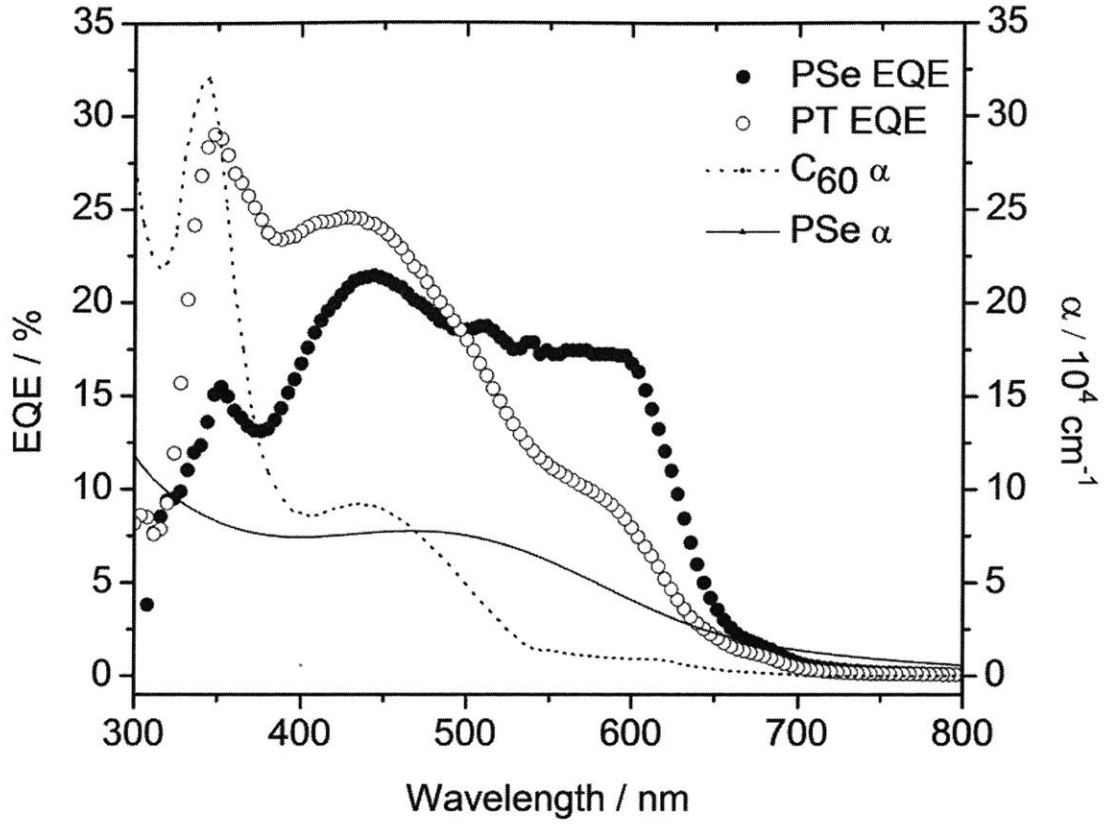

Figure 2-6. (a) Representative J-V curves for varying polyselenophene layer thickness with 30 nm of C_{60}, (b) Comparison of absorption coefficients of oCVD polyselenophene and oCVD polythiophene. (c) EQE spectra of representative photovoltaic devices using oCVD polythiophene and polyselenophene, and absorption coefficients of oCVD polyselenophene and C_{60}.

However, the increase in the polymer layer thickness must have a negative impact on hole diffusion, as holes must go through the longer path from the donor-acceptor interface after charge separation in order to be collected by anode. The longer path can cause more holes to be extinguished during the hole diffusion since oCVD PSe with imperfect regioregularity is likely

to have a relatively low hole mobility. It is strongly associated with a rise in series resistance (R_S) with increasing PSe layer thickness, observed as a lower slope at V_{OC} in the J-V curves of **Figure 2-6a**. The correlation between R_S and exciton-generating polymer layer thickness is also supported by an previous study.[28] Generally, each semiconducting polymer has a different level of trade-off between exciton generation from optical absorption and hole diffusion, deteriorating with a longer diffusion path, based on its own α, bandgap, and charge mobility. For PSe, 60 nm is the optimum thickness striking a balance between exciton generation and hole diffusion.

The EQE spectrum was measured for the optimized PSe photovoltaic device (filled circles). The spectrum in **Figure 2-6c** makes it clear how photocurrent is related to incident photon by the device quantum efficiency. Notably, the spectrum shape is well-matched with a combination of α curves of PSe and C_{60}, which confirms the photocurrent originates from photon to electron conversion by PSe and C_{60}. To attain more systematic understanding of oCVD PSe's photo-responsivity, the EQE of the PSe device is compared with that of polythiophene (PT) solar cells (open circles), adopted from our previously published data.[28] As shown in **Fig. 6c**, the PSe device exhibits a broader EQE spectrum with pronounced shoulder at 610 nm than the PT device does, which suggests oCVD PSe is more photo-sensitive in the red than oCVD PT. It is coherent with the comparison of α_{PSe} and α_{PT} in **Figure 2-6b** as well as EQE spectrum distribution patterns established by poly(3-hexylselenophene) research.[32] However, the peak EQE for PSe is smaller than for PT. It is most likely explained by reduced charge mobility in oCVD PSe compared to in oCVD PT. The cause of the degradation of charge mobility is discussed in the next section.

2.4.4. Regiochemical defects in oCVD polyselenophene

As regioregularity of semiconducting polymers is closely connected to their charge mobility, the more regioregular, the better for photovoltaic performance by realizing smaller R_S and thus larger FF.[5,19,32] According to our preceding research, the main difference between PSe and PT photovoltaic devices is FF in terms of performance parameters.[28] In other words, oCVD PSe could be less regioregular than oCVD PT. In order to gain insights into the difference in regioregularity between oCVD PSe and PT, selenium's ionization energy (IE) and sulfur's IE are compared since IE is an important chemical property affecting oxidative polymerization mechanisms.

Selenium has the lower IE (941 kJ/mole) than sulfur (999.6 kJ/mole) because selenium is in the 4^{th} row of the periodic table and thus holds more valence electrons farther from the atomic nucleus than its 3^{rd} row analogue. This indicates when selenophene is oxidized into a radical intermediate to initiate oxidative polymerization, selenium's smaller IE could render the intermediate more stable. As a result, the intermediate has an increased chance for radical migrations from carbon 2 (or 5) to carbon 3 (or 4). If the radical migrations occur, the final product, polyselenophene, should have regiochemical defects, degrading charge mobility, R_S, FF, and η_p sequentially. (See **Figure 2-7** for more details).

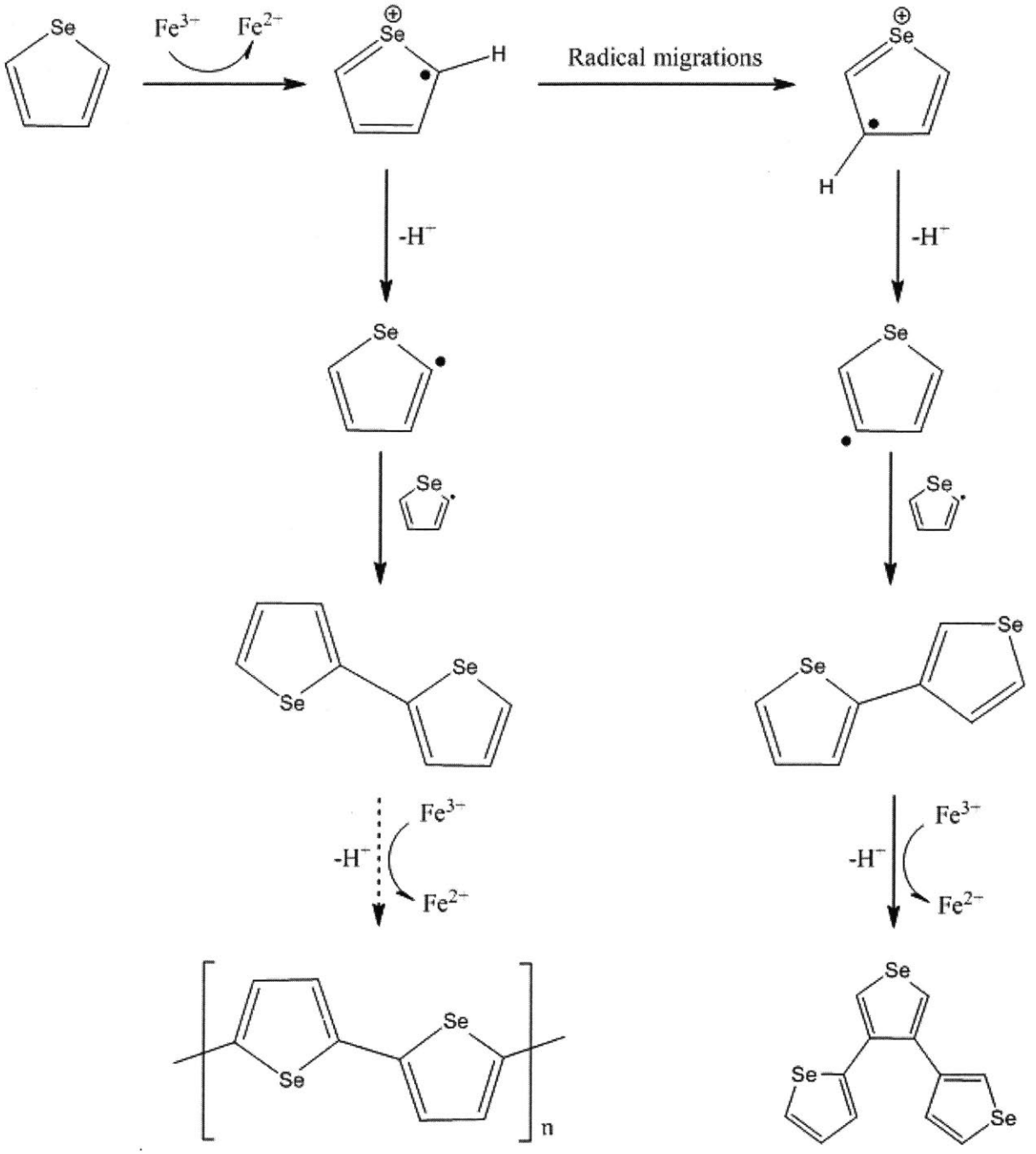

Figure 2-7. Regiochemical defects within oCVD polyselenophene caused by radical migrations.

The regionchemical defects were actually identified by FTIR analysis. The sharp FTIR peak (~ 790 cm^{-1}) and the broad FTIR peak (~ 830 cm^{-1}) in **Figure 2-2a** correspond to α-α'

coupling (i.e., regioregular structure in polymer chain) and α-β coupling (i.e., regiochemical defects in polymer chain), respectively. Hence, the replacement of sulfur by selenium has a negative influence on the regioregularity of oCVD-processed polymer, whereas the enhanced electron donating capability of selenium provides PSe with higher dielectric constant and smaller bandgap than those of PT.

2.5. Conclusions

As oCVD enables insoluble and infusible polyselenophene to be incorporated into bilayer heterojuction photovoltaic devices with C_{60}, we were able to demonstrate polyselenophene's photovoltaic effect with a maximum η_p of 0.4% for the first time using the novel, yet simple, vacuum-based vapor-printing technique. Vapor-printed polyselenophene exhibits the reduced optical bandgap of 1.76 eV as well as enhanced photo-responsivity in the red in comparison with its analogue, polythiophene. These relative advantages are most likely due to selenium's electron-donating nature, but this characteristic also causes selenium to have lower ionization energy than sulfur. As a result, more regiochemical defects form within oCVD polyselenophene than in oCVD polythiophene, which is ultimately disadvantageous for η_p. This is a remaining issue limiting the η_p of the polyselenophene solar cells.

2.6. References

[1] M. Grätzel, *Inorg. Chem.* **2005**, *44*, 6841.

[2] T. R. Cook, D. K. Dogutan, S. Y. Reece, Y. Surendranath, T. S. Teets, D. G. Nocera, *Chem. Rev.* **2010**, *110*, 6474.

[3] M. G. Walter, E. L. Warren, J. R. McKone, S. W. Boettcher, Q. Mi, E. A. Santori, N. S. Lewis, *Chem. Rev.* **2010**, *110*, 6446.

[4] W. J. Jo, J.-W. Jang, K. Kong, H. J. Kang, J. Y. Kim, H. Jun, K. P. S. Parmar, J. S. Lee, *Angew. Chem. Int. Ed.* **2012**, *51*, 3147.

[5] B. C. Thompson, J. M. J. Frechet, *Angew. Chem. Int. Ed.* **2008**, *47*, 58.

[6] R. D. McCullough, *Adv. Mater.* **1998**, *10*, 93.
[7] C. J. Brabec, S. Gowrisanker, J.J.M. Halls, D. Laird, S.J. Jia, S.P. Williams, *Adv. Mater.* **2010**, *22*, 3839.
[8] E. Bundgaard, F. C. Krebs, *Sol. Energ. Mat. Sol. C.* **2007**, *91*, 954.
[9] S.R. Forrest, *Nature* **2004**, *428*, 911.
[10] J. You, L. Dou, K. Yoshimura, T. Kato, K. Ohya, T. Moriarty, K. Emery, C.-C. Chen, J. Gao, G. Li, Y. Yang, *Nat. Commun.* **2013**, *4*, 1446.
[11] 12.0% efficienct vacuum-deposited organic small molecular solar cells (Heliatek), www.heliatek.com/newscenter/latest_news/neuer-weltrekord-fur-organische-solarzellen-heliatek-behauptet-sich-mit-12-zelleffizienz-als-technologiefuhrer/?lang=en, accessed: April, 2014.
[12] D. C. Watter, H. Yi, A. J. Pearson, J. Kingsley, A. Iraqi, D. Lidzey, *Macromol, Rapid Commun.* **2013**, *34*, 1157.
[13] D. Bhattacharyya, K. K. Gleason, *J. Mater. Chem.* **2012**, *22*, 405.
[14] L. J. A. Koster, S. E. Shaheen, J. C. Hummelen, *Adv. Energy Mater.* **2012**, *2*, 1246.
[15] R. C. Chiechi, J. C. Hummelen, *ACS Macro Lett.* **2012**, *1*, 1180.
[16] N. Camaioni, R. Po, *J. Phys. Chem. Lett.* **2013**, *4*, 1821.
[17] D. S. Chung, H. Kong, W. M. Yun, H. Cha, H.-K. Shim, Y.-H. Kim, C. E. Park, *Org. Electron.* **2010**, *11*, 899.
[18] D. J. Crouch, P. J. Skabara, M. Heeney, I. McCulloch, D. Sparrowe, S. J. Coles, M. B. Hursthouse, *Macromol. Rapid Commun.* **2008**, *29*, 1839.
[19] M. Heeney, W. Zhang, D. J. Crouch, M. L. Chabinyc, S. Gordeyev, R. Hamilton, S. J. Higgins, I. McCulloch, P. J. Skabara, D. Sparrowe, S. Tierney, *Chem. Commun.* **2007**, *47*, 5061.
[20] H. Kong, D. S. Chung, I.-N. Kang, J.-H. Park, M.-J. Park, I. H. Jung, C. E. Park, H.-K. Shim, *J. Mater. Chem.* **2009**, *19*, 3490.
[21] Y. Kunugi, K. Takimiya, K. Yamane, K. Yamashita, Y. Aso, T. Otsubo, *Chem. Mater.* **2003**, *15*, 6.
[22] D. Gao, J. Hollinger, D. S. Seferos, *ACS Nano*, **2012**, *6*, 7114.
[23] J. Hollinger, J. Sun, D. Gao, D. Karl, D. S. Seferos, *Macromol. Rapid Commun.* **2013**, *34*, 437.
[24] F. C. Krebs, H. Spanggaard, *Chem. Mater.* **2005**, *17*, 5235.
[25] S. A. Gevorgyan, F.C. Krebs, *Chem. Mater.* **2008**, *20*, 4386.
[26] A. Patra, M. Bendikov, *J. Mater. Chem.* **2010**, *20*, 422.
[27] A. M. Coclite, R. M. Howden, D. C. Borrelli, C. D. Petruczok, R. Yang, J. L. Yagüe, A. Ugur, N. Chen, S. Lee, W. J. Jo, A. Liu, X. Wang, K. K.Gleason, *Adv. Mater.* **2013**, *25*, 5392.
[28] D. C. Borrelli, M. C. Barr, V. Bulović, K. K. Gleason, *Sol. Energ. Mat. Sol. C.* **2012**, *99*, 190.
[29] T. A. Skotheim, R. L. Elsenbaumer, J. R. Reynolds, *Handbook of Conducting Polymers*, Marcel Dekker, Inc., New York **1998**, p. 225.
[30] C. M. Cardona, W. Li, A. E. Kaifer, D. Stockdale, G. C. Bazan, *Adv. Mater.* **2011**, *23*, 2367.
[31] P. Peumans, A. Yakimov, S. R. Forrest, *J. Appl. Phys.* **2003**, *93*, 3693.
[32] A. M. Ballantyne, L. Chen, J. Nelson, D. D. C. Bradley, Y. Astuti, A. Maurano, C. G. Shuttle, J. R. Durrant, M. Heeney, W. Duffy, I. McCulloch, *Adv. Mater.* **2007**, *19*, 4544.

CHAPTER THREE

Oxidative Chemical Vapor Deposition of Neutral Hole Transporting Polymer for Enhanced Solar Cell Efficiency and Lifetime

This chapter is adapted and reprinted with permission from: Won Jun Jo, Justin Nelson, Sehoon Chang, Vladimir Bulović, Silvija Gradečak, Michael S. Strano, and Karen K. Gleason, *Oxidative Chemical Vapor Deposition of Neutral Hole Transporting Polymer for Enhanced Solar Cell Efficiency and Lifetime*, **Advanced Materials**, 28, 6399-6404 (2016).

3.1. Abstract

Organic solar cells have offered great promise due to their potential to enable lightweight, flexible, large-area, and cost-effective photovoltaic technology, but they are not as efficient and stable as their inorganic counterparts. To solve this problem, the concept of a neutral polymeric hole transporting layer is realized for the first time, by integrating patterned Cl^- doped poly(3,4-dimethoxythiophene) thin films into organic solar cells via a vacuum-based polymer vapor printing technique – oxidative chemical vapor deposition (oCVD) combined with in-situ shadow masking. Due to this novel polymer's neutrality, high transparency, good conductivity, and appropriate energy levels, the efficiency and lifetime of organic solar cells are remarkably boosted compared to those of organic solar cells depending on the commercial hole transporting polymer, poly(3,4-ethylenedioxythiophene):polystyrene sulfonate (PEDOT:PSS). Thus, neutral Cl^- doped poly(3,4-dimethoxythiophene) is a suitable alternative to acidic PEDOT:PSS.

3.2. Introduction

A variety of solar energy conversion systems have emerged as attractive candidates to establish fossil fuel-free energy networks.[1-3] Among these, organic solar cells offer the promise of lightweight, flexible, large-area, and cost-effective photovoltaic technology.[4-7] But, they are not as efficient and stable as their inorganic counterparts. To solve this problem, the concept of a neutral polymeric hole transporting layer (HTL) is realized for the first time, by integrating patterned Cl^- doped poly(3,4-dimethoxythiophene) thin films into organic photovoltaic devices (OPVs) via a vacuum-based polymer vapor printing technique – oxidative chemical vapor deposition (oCVD) combined with in-situ shadow masking. Due to this novel polymer's neutrality, high transparency, good conductivity, and appropriate energy levels, the efficiency and stability of OPVs are remarkably boosted compared to those of OPVs depending on the

commercial hole transporting polymer, poly(3,4-ethylenedioxythiophene):polystyrene sulfonate (PEDOT:PSS).

In conventional OPVs, thin photoactive organic layers are sandwiched between the anode and cathode. The interlayer between photoactive organics and anode has a significant impact on the performance of OPVs.[8,9] The transparency influences the light absorption of photoactive organics while the energy levels and charge transport characteristics impact photo-generated hole extraction and collection. Consequently, the anode interlayer's properties have a direct effect on the performance parameters of OPVs, such as open-circuit voltage (V_{OC}), short-circuit current density (J_{SC}), fill factor (FF), and the final power conversion efficiency (PCE).

In order to optimize the performance parameters, HTLs of various composition have been applied to the anode interlayer.[9-11] Among them, PEDOT:PSS has been the most popular because of its deep work function (i.e., suitable highest occupied molecular orbital [HOMO] level for various organic donor materials), high transparency in the visible-light region, solubility for spin-coating, mechanical flexibility, and earth-abundant element composition (i.e., C, H, O, and S).[9,12] However, due to the PSS dopants, PEDOT:PSS has a strong acidic nature. This high acidity corrodes photoactive organics and anode materials, and finally damages the PCE and lifetime of OPVs.[13-15] In this regard, a new neutral hole transporting polymer should be developed to improve the stability of OPVs.

Poly(3,4-dimethoxythiophene) (PDMT) can be an appropriate neutral alternative to PEDOT:PSS because PDMT also has deep work function, high transparency, mechanical flexibility, and the same earth-abundant element composition (i.e., C, H, O, and S). However, PDMT has two major shortcomings limiting its incorporation into OPVs as a HTL. First, its conductivity is too low to promote photo-generated hole transport from HOMO levels of

photoactive organics to anode.[16] Second, PDMT's poor solubility prohibits solution processing, thereby rendering its thin-film fabrication on targeted substrates more complex and difficult. Although there are several previous studies to make PDMT thin-films using electrochemical polymerization, it is not easy for electrochemical polymerization to control the conductivity, uniformity, thickness, and pattern shape of polymer thin-film products.[17-21]

To resolve the abovementioned issues, we used oCVD technique integrated with in-situ shadow masking. Unlike other standard methods (e.g., spin-coating, electrochemical polymerization, etc.), oCVD offers a groundbreaking substrate-independent fabrication route to insoluble or infusible polymers because it is a solvent-free, vacuum-based technique enabling conformal thin-film coating of varied conjugated polymers in a single dry step.[13,27,28] Specifically, oCVD is a single-dry-step process to simultaneously synthesize, deposit, and dope conjugated polymers on a wide array of substrates at low temperature ($\leq$ 100 °C) in controllable patterns, aligned with in-situ shadow masking. Moreover, oCVD still maintains vacuum processing benefits, such as well-defined thickness control and uniformity, conformal coverage, parallel and sequential deposition, and inline convertibility with other standard vacuum processes (e.g., thermal evaporation).[7] Recently, this versatile technique has materially advanced its applicability to fabricate diverse semiconducting/conducting polymer thin flims for organic electronics.[21]

3.3. Experimental Methods

3.3.1. Poly(3,4-dimethoxythiophene) Depositions

When substrates were indium tin oxide (ITO) coated glass for photovoltaic device fabrication, the polymer film was prepared by the vapor printing method. Otherwise, the basic oCVD process

without shadow masking was employed to prepare the polymer films. The custom-built oCVD reactor consists of a vacuum chamber connected to monomer inlet ports and an exhaust to a pump. At the bottom and top of the chamber, a heating crucible for an oxidant and an inverted stage for substrates are placed, respectively.

During the deposition, the reactor body and inverted stage were maintained at a temperature of 120 °C and 80 °C, respectively. The chamber pressure was tuned to 150 mTorr. Iron(III) chloride ($FeCl_3$, 97%, Sigma–Aldrich) and 3,4-dimethoxythiophene (97%, Sigma–Aldrich) were used as the oxidant and monomer without any further purification. $FeCl_3$ was sublimed at 205 °C. Polymer film thickness was controlled by the deposition time. Vapor-phase 3,4-dimethoxythiophene monomer was introduced into the reactor from a monomer jar. The temperature of the monomer jar was maintained at 80 °C and a needle valve was used to render the monomer vapor flow rate constant at around 1 sccm. After deposition, the films were rinsed by immersing them into 0.25 M NaCl solution (0.25 M NaCl dissolved in methanol) for 10 min to remove unreacted oxidant and maximize Cl^- dopant concentration.

3.3.2. Polymer Characterizations

Fourier transform infrared (FTIR) measurements of PDMT films on silicon wafers were performed on a Nexus 870, Thermo Electron Corp. spectrometer. The atomic compositions of the films were estimated by X-ray photoelectron spectroscopy (XPS) a PHI VersaProbe II (Physical Electronics). The film thicknesses were examined using a Veeco Dektak 150 surface profilometer. The sheet resistances of the films were measured with a Jandel four-point probe in air. Conductivity values were calculated using the measured sheet resistivity and thickness. Morphology analysis for PDMT films were accomplished using an Agilent Technologies AFM

in tapping mode with a Bruker Si cantilever having a tip frequency of 330 kHz. The UV–vis spectra of PDMT films on bare glasses were measured with a Varian Cary 5000 UV–vis spectrophotometer. To evaluate absorption coefficient of the films, transmission and reflection spectra were measured. For the reflection spectra, a specular reflectance accessory and an Al standard reference mirror (ThorLabs) were used.

To identify the highest occupied molecular orbital (HOMO) level of the oCVD-processed PDMT, cyclic voltammetry (CV) were conducted in a standard three-electrode cell containing tetrabutylammonium hexafluorophosphate (0.1 M) in acetonitrile as the electrolyte under a nitrogen atmosphere. The PDMT film on an ITO-coated glass, $Ag/AgNO_3$ (0.01 M in acetonitrile), and a Pt mesh attached to a Pt wire worked as the working electrode, reference electrode, and counter electrode, respectively. Current-voltage data were collected at a scan rate of 100 mV s^{-1} with ferrocene/ferrocenium (Fc/Fc^+) redox couple to calibrate the Ag/Ag^+ reference electrode, and analyzed with a 660D potentiostat (CH Instruments).

3.3.3. Solar Cell Fabrication and Characterizations

The photovoltaic devices were fabricated on 75 nm patterned ITO-coated glasses (Thin Film Devices, 50Ω/sq), cleaned by solvents (2 x DI water, 2 x acetone, and 2 x isopropanol) followed by 30 s of O_2 plasma (100W, Plasma Preen, Inc.). As described above, PDMT films having different thicknesses were simultaneously synthesized and deposited on the substrates via oxidative polymerization, and then rinsed in the 0.25 M NaCl solution (0.25 M NaCl dissolved in methanol) for 10 min to remove reacted oxidant. After the oCVD PDMT hole transporting layer deposition, dibenzo-tetraphenyl-periflanthene (DBP, Luminescence Technology Corp.), C_{60} (99.9%, Sigma–Aldrich, purified once by vacuum train sublimation), bathocuproine (BCP,

Luminescence Technology Corp.), and Ag (Alfa Aesar, 1–3 mm shot, 99.9999%) were thermally evaporated at a rate of 0.1 nm/s. DBP (25 nm), C_{60} (40 nm), BCP (7.5 nm), and Ag (100 nm) were used as electron donor, electron acceptor, electron transporting layer, and cathode, respectively. The Ag cathode was deposited through a shadow mask for each device to obtain the well-defined device area, 1.21 mm^2, which is estimated from the overlapped area between Ag cathode and ITO anode.

Current density-voltage (J-V) measurements were conducted in nitrogen atmosphere, and recorded by a Keithley 6487 picoammeter. One sun of air mass 1.5 G (AM 1.5 G) irradiation (100 mW/cm^2) was generated by 1 kW xenon arc-lamp (Newport 91191) filtered by an AM 1.5G filter. The solar simulator intensity was estimated using a calibrated silicon photodiode. The external quantum efficiency (EQE) spectrum was recorded by a Stanford Research Systems SR830 lock-in amplifier. A focused monochromatic beam of variable wavelength light was provided by an Oriel 1 kW xenon arc lamp equipped with an Acton 300i monochromator and chopped at 43 Hz. The incident monochromatic light intensity was evaluated using a Newport 818-UV calibrated silicon photodiode.

3.3.4. PEDOT:PSS Spin-Coating

PEDOT:PSS (Clevios P VP AI 4083) was filtered (0.45 μm), spin-coated at 6000 rpm (20 nm films), 4500 rpm (31 nm films), and 3000 rpm (40 nm films) for 60 seconds, and annealed at 200 °C for 15 min in air.

3.4. Results and Discussion

Based on the abovementioned strengths of oCVD, we successfully made patterned PDMT thin films on non-conductive substrates for the first time. As **Figure 3-1a** shows, 3,4-

dimethoxythiophene monomer vapor is oxidatively polymerized in the presence of iron (III) chloride oxidant, and at the same time PDMT is deposited on a diversity of substrates, placed on the temperature-controlled stage of the oCVD reactor. The PDMT thin-film thickness is easily controlled by adjusting the polymer-deposition time. The FTIR spectrum of the oCVD-processed PDMT film in **Figure 3-1b** clearly identifies the representative functional groups of PDMT (alkyl C–H stretch [3000~2850 cm^{-1}], aromatic C=C stretch [1500~1400 cm^{-1}], C–O stretch [1320~1000 cm^{-1}], aromatic C–H bending [860~750 cm^{-1}], and C–H out-of-plane vibrations [~690 cm^{-1}]). Also, the Raman spectrum in **Figure 3-S1** displays the key functional groups of PDMT. These outcomes are well-matched with PDMT's previously reported characterization data,[16-19] and thus confirm that PDMT films are successfully synthesized via oCVD.

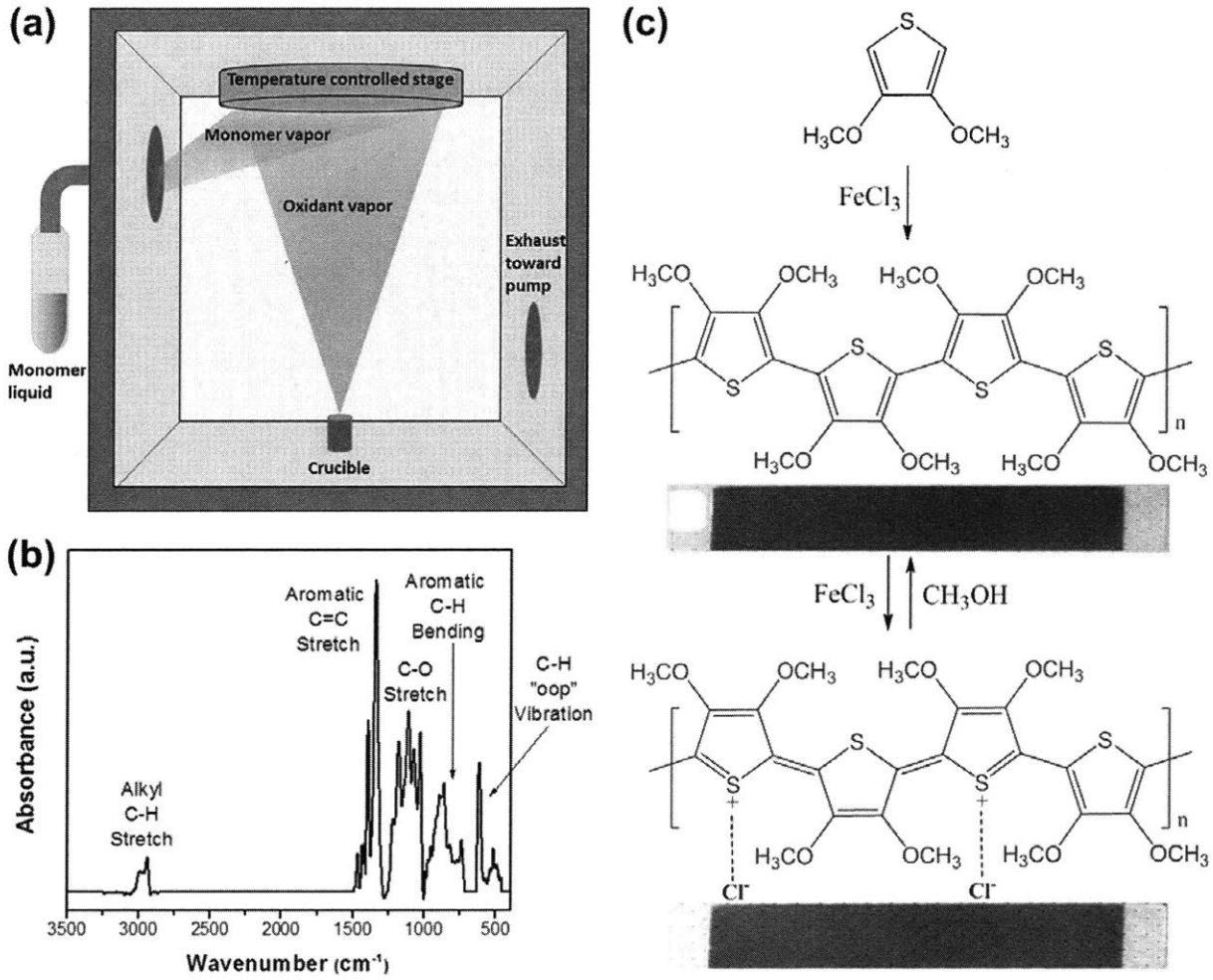

Figure 3-1. a) Schematic of oCVD reactor, b) FTIR spectrum of oCVD-processed PDMT film, c) Synthetic route from 3,4-dimethoxythiophene to over-oxidized PDMT, with undoped and doped PDMT film photos.

As the synthetic route in **Figure 3-1c** depicts, the oxidative polymerization accomplished by oCVD generates a conducting doped-form PDMT through over oxidation forming polarons and bipolarons.[22] The doped-form PDMT has cations (S^+), charge-balanced by counter anions (Cl^-). Thanks to the Cl^- anion dopants from iron (III) chloride oxidant, the doped PDMT has

good conductivity (~10 S/cm) without acidity, unlike PEDOT:PSS. Moreover, doped-PDMT thin films have as high transparency as PEDOT:PSS thin films, as illustrated in **Figure 3-2a and b**. Additionally, the transmittance data in **Figure 3-2a and b** reveal that the onset of optical absorption by doped PDMT appears at 460 nm, which corresponds to the optical bandgap of 2.7 eV. This means if doped-PDMT thin films possess a proper HOMO level, they can be deployed to OPVs as HTLs, because they are transparent enough to allow photoactive organics to have sufficient light absorption.

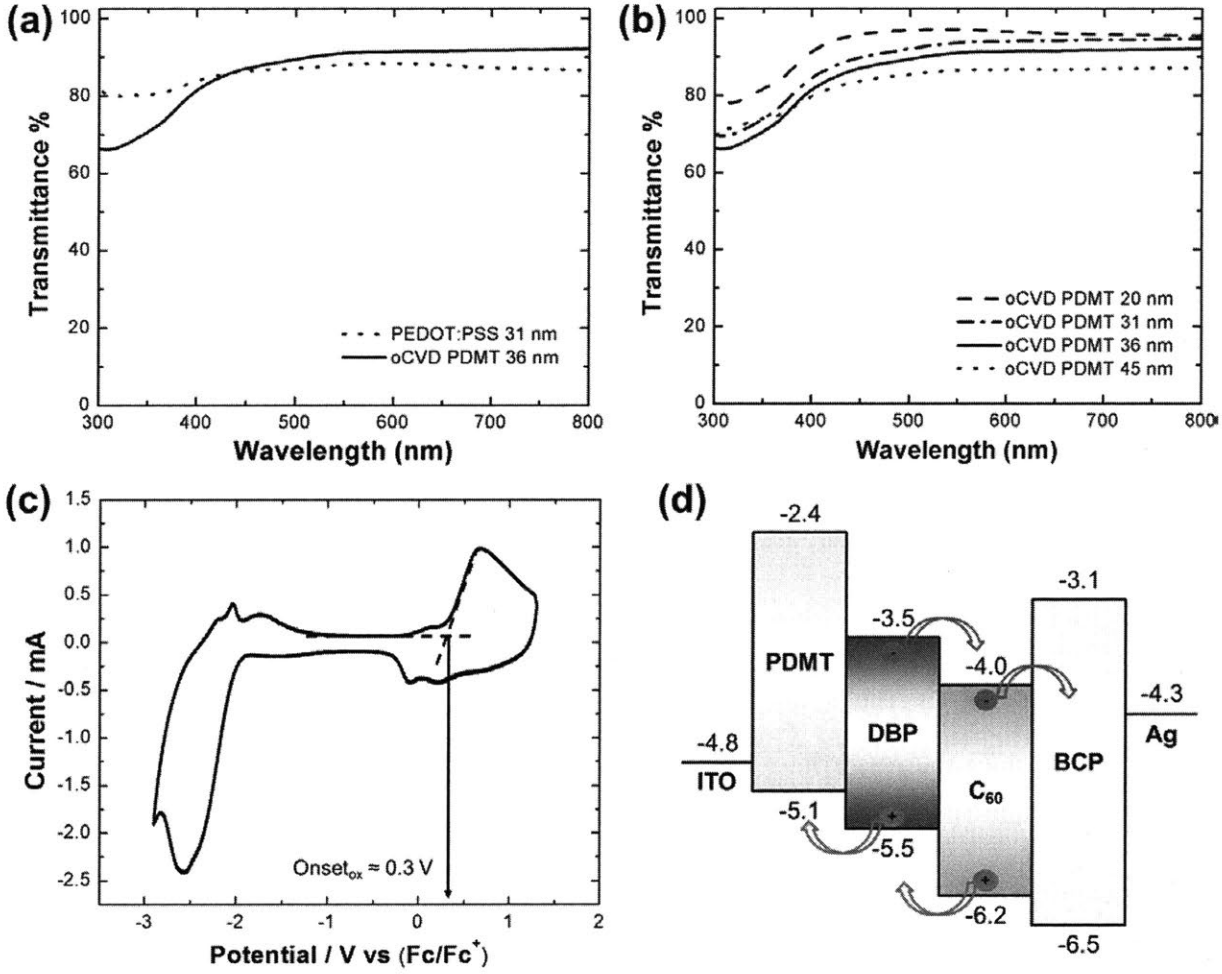

Figure 3-2. a) Transmittance of 31 nm spin-coated PEDPT:PSS film and 36 nm oCVD-processed PDMT film, b) Transmittance of 20, 31, 36, and 45 nm oCVD-processed PDMT films, c) Cyclic voltammetry of oCVD-processed PDMT film, d) Schematic energy-level alignment of DBP/C_{60} solar cells with PDMT HTLs.

To determine the HOMO level of PDMT, cyclic voltammetry (CV) was conducted using the standard three-electrode setup. The resulting CV curve for PDMT is shown in **Figure 3-2c**. Based on the curve, the HOMO level is located by following previously published procedures.[7,23] The onset of the oxidation peak is -0.3 V vs Fc/Fc^+. The HOMO is then calculated by the following equation (1), assuming the redox potential of Fc/Fc^+ is -5.1 eV, relative to vacuum.[23]

$$E_{HOMO} = -(E_{[oxidation\ onset\ vs\ Fc/Fc+]} + 4.8)\ (eV) \quad (1)$$

The calculated HOMO level is -5.1 eV, and the lowest unoccupied molecular orbital (LUMO) level of PDMT is estimated to be -2.4 eV by adding the optical bandgap of 2.7 eV to the HOMO level. Taking the estimated HOMO and LUMO levels into account, the schematic energy-level alignment of DBP (dibenzo-tetraphenyl-periflanthene)/C_{60} solar cells with PDMT HTLs is drawn in **Figure 3-2d**. The schematic alignment verifies that doped PDMT has an appropriate HOMO level for forming an ohmic contact between photoactive organics (DBP and C_{60}) and anode (ITO, indium tin oixde), thereby promoting photo-generated hole transport from the HOMO levels of DBP and C_{60} to the ITO anode. Further, the HOMO and LUMO levels of doped PDMT match well with the band structure of a variety of photovoltaic materials, including

perovskites (methylammonium lead halides), diverse types of quantum dots, and a variety of inorganic semiconductors.

In addition, thanks to the conformal and dry nature of oCVD polymer coating, PDMT films over 20 nm in thickness have smooth surfaces, as the AFM images in **Figure 3-S2** illustrate. This smoothness is vital for optimizing series and shunting resistances (R_S and R_{Sh}) within OPVs as well as preventing unwanted short circuits between the front and back surface contacts of OPVs.

All of the above physicochemical characterization results confirm the candidacy of oCVD PDMT thin films as a neutral HTL for replacing acidic PEDOT:PSS. Therefore, neutral PDMT was next integrated into OPVs for the first time using the polymer vapor-printing technique (i.e., oCVD combined with in-situ shadow masking). As the device diagram in **Figure 3-3a** exhibits, we employed the conventional single-bilayer-heterojunction architecture, consisting of glass substrate having a 75 nm thick ITO anode, a 25 nm thick electron-donating DBP layer, a 40 nm thick electron-accepting C_{60} layer, a 7.5 nm thick hole-blocking BCP layer, and a top-capping Ag cathode, 100 nm in thickness.

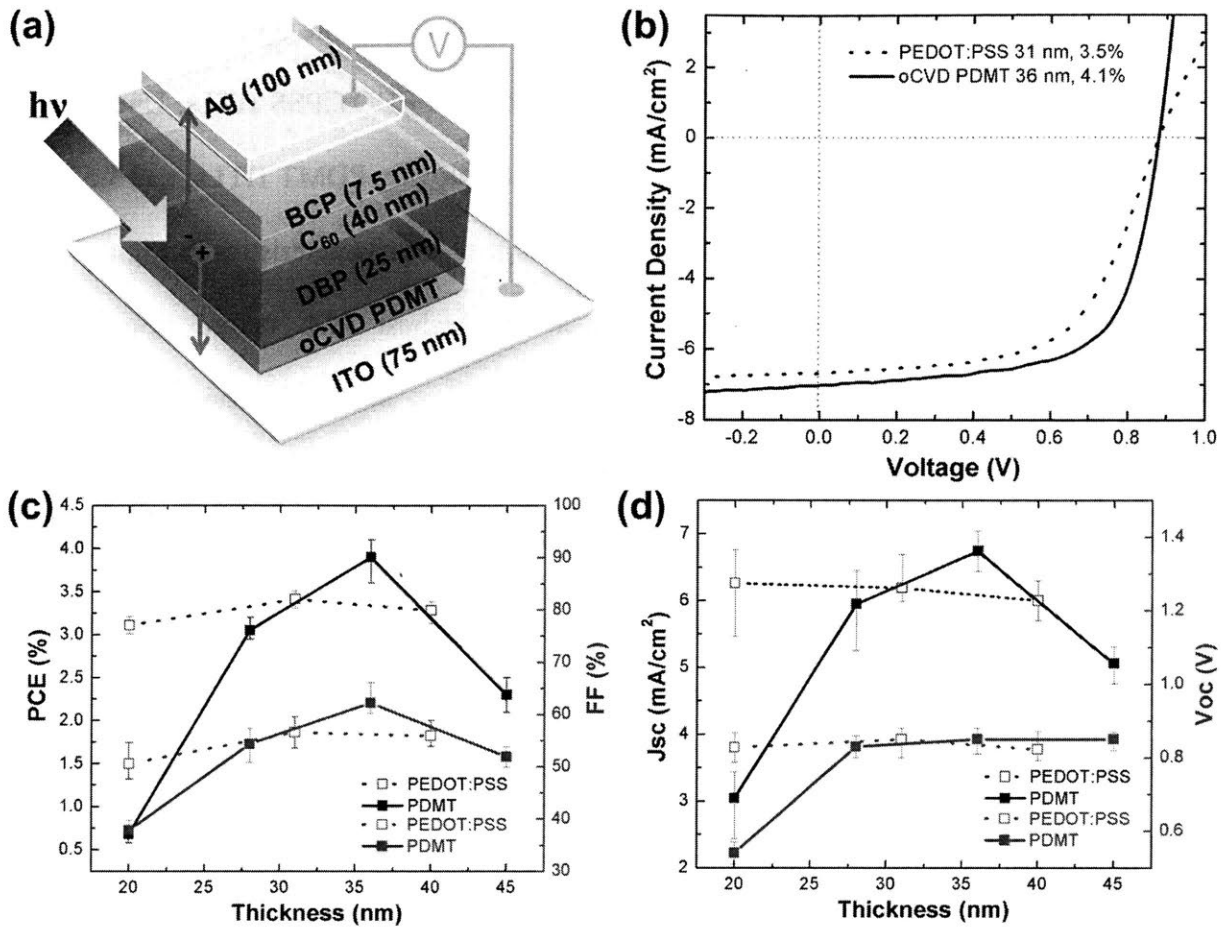

Figure 3-3. a) Device diagram of DBP/C_{60} solar cells with PDMT HTLs. b) J-V charateristics of champion devices under AM 1.5G irradiation, c) PCE and FF, d) J_{SC} and V_{OC} for varying PEDOT:PSS/PDMT HTL thickness (symbols: average values of 6-10 devices, error bar: maximum and minimum values).

We tested a range of thicknesses of PEDOT:PSS and PDMT HTLs to understand, compare, and optimize how the two HTLs affect the DBP/C_{60} solar cell function. **Figure 3-S3** displays how the DBP/C_{60} solar cell PCE varies with PEDOT:PSS and PDMT HTL thickness with all other layer thicknesses fixed. While PDMT HTL thickness change has a remarkable

influence on the PCE, PEDOT:PSS HTL thickness change does not. The optimum thickness to maximize the PCE is 36 nm for PDMT HTLs, and 31 nm for PEDOT:PSS HTLs. Under these best thickness conditions, the maximum PCE is 4.1% for employing PDMT HTLs, and 3.5% for using PEDOT:PSS HTLs, as the current density vs. voltage (J-V) characteristics in **Figure 3-3b** describe. To the best of our knowledge, 4.1% is the highest PCE record achieved by conventional DBP/C_{60} bilayer-heterojunction solar cells.[10,24,25] When comparing the performance parameters, as shown in **Figure 3-3c and d**, it becomes clear that 36 nm thick PDMT HTLs perform better than 31 nm thick PEDOT:PSS HTLs by enhancing the FF and J_{SC} of the DBP/C_{60} solar cells. Meanwhile, there is no significant difference in the V_{OC} between PEDOT:PSS and PDMT HTLs, after reaching its peak value (0.85~0.88 V). The physical mechanisms that PDMT HTLs enable the higher J_{SC} and FF than PEDOT:PSS HTLs will be discussed next.

To have more systematic understanding on the improvement in J_{SC}, dark J-V characteristics (**Figure 3-4a**) and EQE spectra (**Figure 3-4b**) were measured. Dark J-V characteristics of the champion devices are plotted on a semi-log scale. A 36 nm thick PDMT HTL generates much lower dark J under forward bias than 31 nm thick PEDOT:PSS HTL by a factor of ~100. This consequence indicates the PDMT HTL achieves better interface (ohmic) contact with less dipoles/carrier traps between DBP and ITO, thereby contributing to the reduction of carrier recombination and the suppression of leakage currents.[26] This mechanism is further supported by the EQE (external quantum efficiency) spectra, where the device quantum efficiency for PDMT is higher over the wavelength range from 375 nm to 500 nm as compared to PEDOT:PSS. This result reveals that the hole-electron pairs produced by 375 to 500 nm wavelength photons are more effectively separated, extracted, and collected with the PDMT HTL

rather than the PEDOT:PSS HTL. In addition, the EQE spectra shape is well matched with a combination of the absorption coefficient curves of DBP and C_{60}, which confirms that the photocurrent originates from photon to electron conversion by DBP and C_{60}.

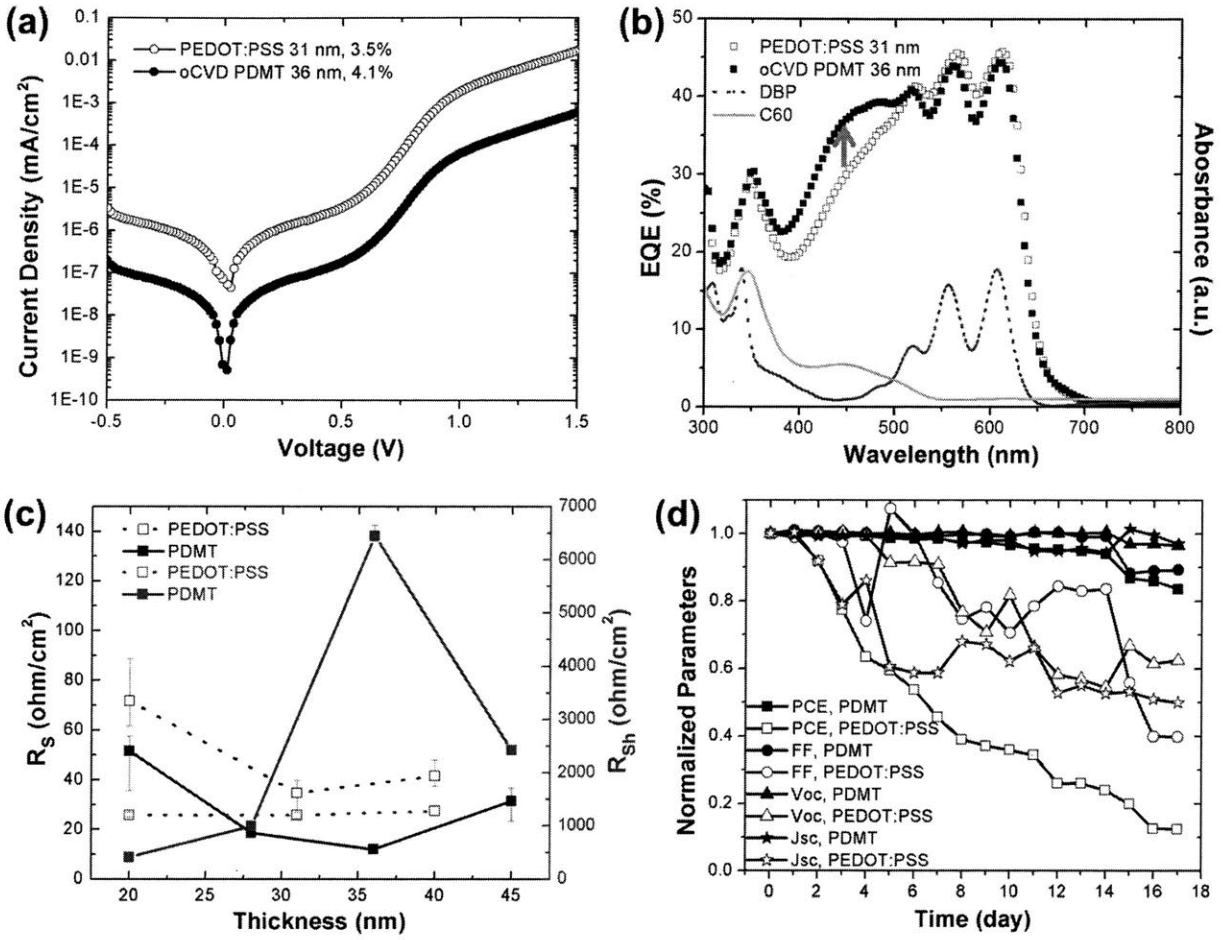

Figure 3-4. a) Dark J-V characteristics of champion devices, b) EQE spectra of champion devices with absorption coefficients of DBP and C_{60}, c) R_S and R_{Sh} for varying PEDOT:PSS/PDMT HTL thickness (symbols: average values of 6-10 devices, error bar: maximum and minimum values), d) Evolution of normalized performance parameters with respect to storage time under N_2 atmosphere.

The mechanism enabling PDMT HTLs to improve the FF is closely related to the variation of series and shunting resistances (R_S and R_{Sh}) within the DBP/C_{60} solar cells. Specifically, as R_S becomes smaller, FF increases. In contrast, the more R_{Sh} increases, the bigger FF grows. As the visualized data in **Figure 3-4c** illustrate, 36 nm thick PDMT HTLs (~12 Ω/cm^2) realize lower R_S than 31 nm thick PEDOT:PSS HTLs (~35 Ω/cm^2), and both of them hit the minimum R_S at their ideal thickness. However, there is a different trend for R_{Sh}. As PDMT HTLs approach their optimum thickness, R_{Sh} spikes to its summit (~6440 Ω/cm^2), whereas R_{Sh} with PEDOT:PSS HTLs remains almost steady (1200~1280 Ω/cm^2) irrespective of their thickness. Consequently, the contact resistance dynamics with PDMT HTLs is much more advantageous than that with PEDOT:PSS HTLs for raising the FF.

PDMT's beneficial contact resistance dynamics results from oCVD's unique merits, enabling direct anion dopant injection into conjugated polymer chains as well as conformal polymer thin-film coating on patterned target substrates in a single dry step. The PSS dopants in PEDOT:PSS generate protons (H^+), as drawn in **Figure 3-S4**. As the proton concentration increases, although the conductivity in PEDOT:PSS HTLs can increase, the photo-generated hole mobility in PEDOT:PSS HTLs can decrease due to the scattering between protons and holes. The reduced hole mobility elevates the interfacial energy barrier for photo-generated hole transport from DBP to ITO, and finally R_S grows. On the other hand, the proton-free Cl^- dopants in oCVD-processed PDMT just augment the conductivity in PDMT HTLs without any scattering effect, and thus minimize the interfacial energy barrier and R_S.

The maximized R_{Sh} by 36 nm thick PDMT HTLs is most likely explained by the conformal and dry nature of oCVD polymer coating. In the case of spin-coating method, dewetting defects (e.g., pinholes, fissures, cracks, etc.) are inevitable, and they cause unwanted

short circuits between the front and back surface contacts of OPVs. However, oCVD polymer coating technique rarely results in the dewetting defects because oCVD is a solvent-free vapor-phase polymer treatment. Hence, 36 nm thick PDMT HTL attains much higher R_{Sh} than 31 nm PEDOT:PSS HTL by a factor of ~5. PDMT HTL thicknesses over or under 36 nm have smaller R_{Sh} owing to rougher surfaces (**Figure 3-S2**). In particular, for under 36 nm thick PDMT HTLs, tunneling effects are more significant and reduce R_{Sh}.

Compared to acidic PEDOT:PSS, another overwhelming benefit is PDMT's neutrality, which improves the device lifetime (**Figure 3-4d**). Beyond the demand of high efficiency, long-term device stability is another linchpin requirement to commercialize OPVs. To evaluate the champion devices' stability as a function of time, continual and periodic PCE measurements were carried out under N_2 atmosphere. The device with the neutral PDMT HTL maintained 83% of its optimum efficiency after 17 days, while the device with the acidic PEDOT:PSS HTL retained only 12% of its best efficiency. When checking how the performance parameters changes as time goes by, it is obvious that Voc, Jsc, and FF with the acidic PEDOT:PSS HTL drops much faster than those with the neutral PDMT HTL, although there are fluctuations. This is because of the intense acidity of PSS dopants, which produce protons. The protons destroy surrounding photoactive organics and anode materials (e.g., DBP and ITO), and finally damages the device performance.[13-15] Meanwhile, the proton-free Cl^- dopants in oCVD-processed PDMT guarantee the neutral nature, where all kinds of molecular components in OPVs can play their own roles properly and sustainably as long as possible.

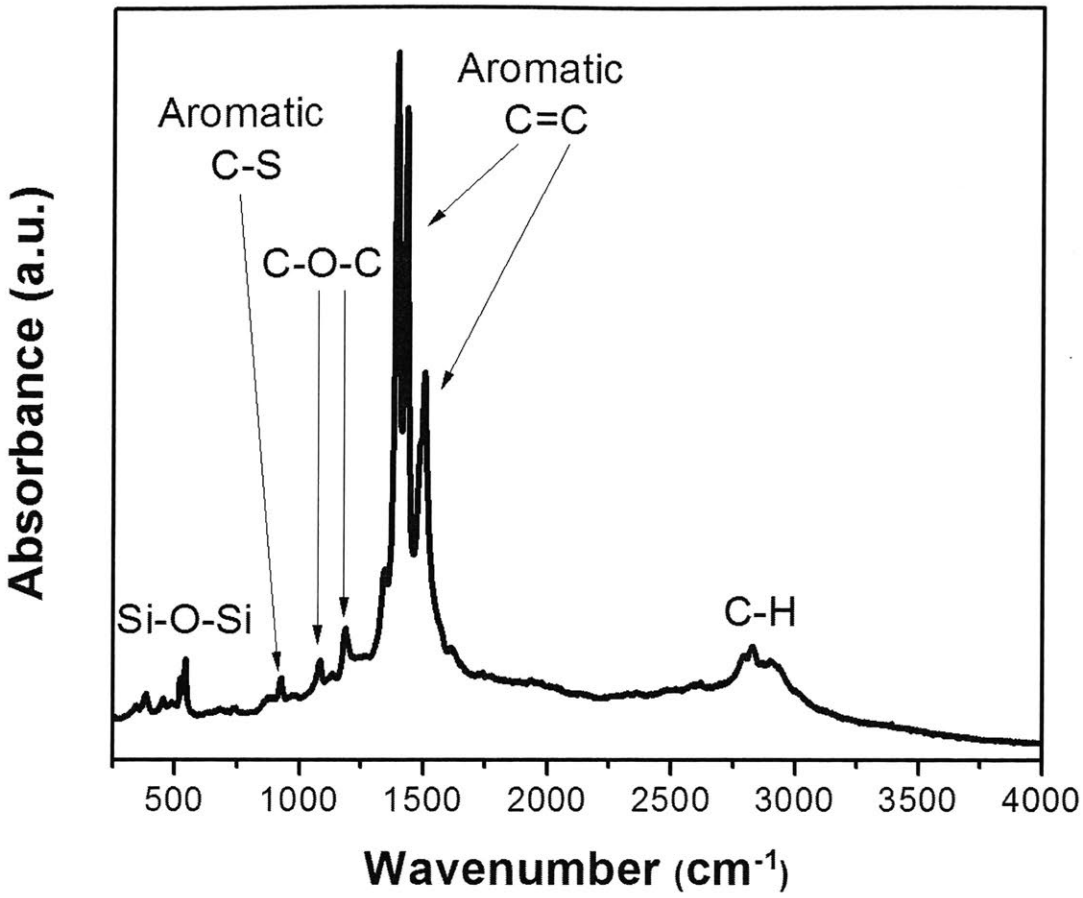

Figure 3-S1. Raman spectrum of oCVD-processed PDMT film

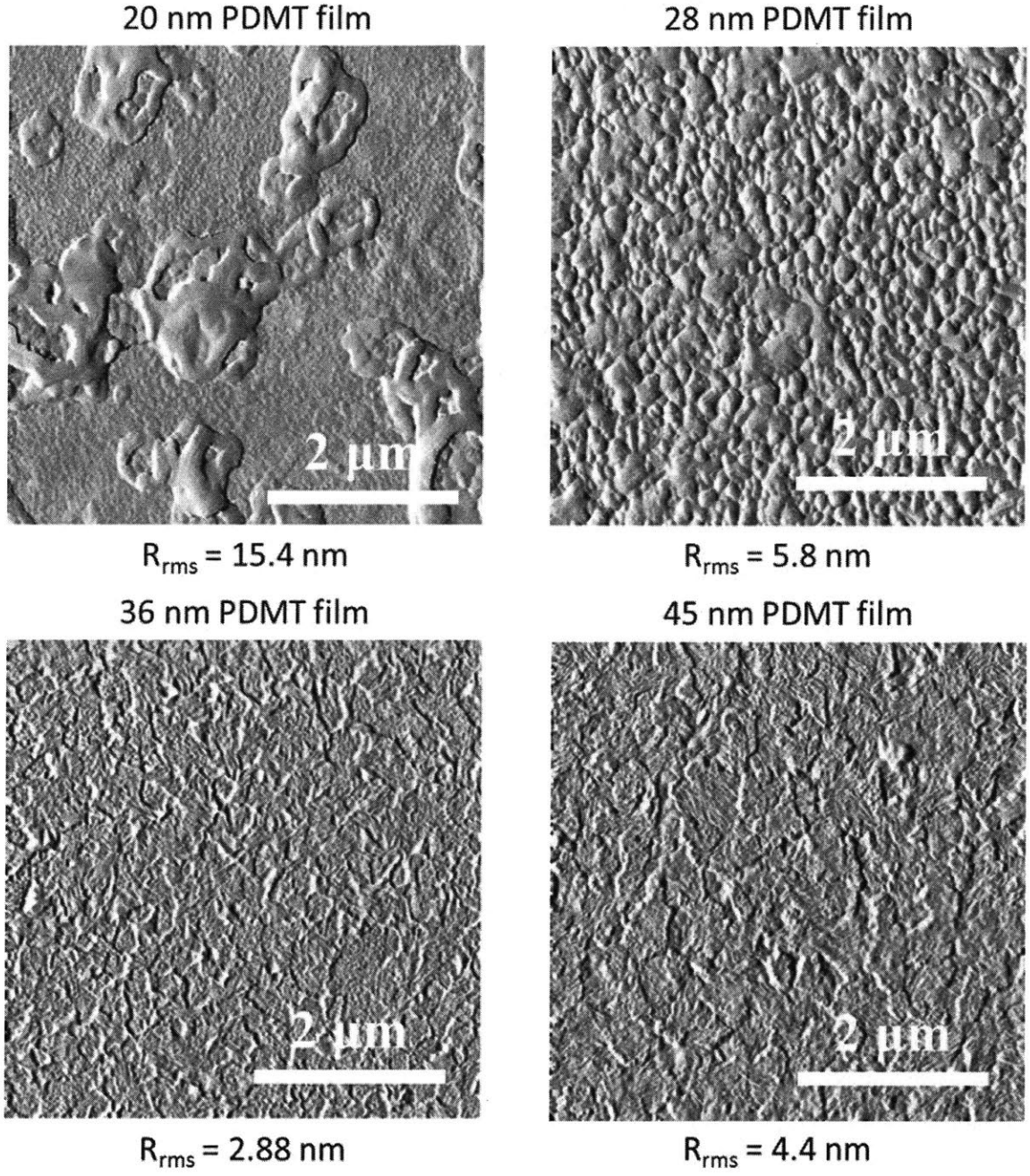

Figure 3-S2. AFM images of oCVD-processed PDMT thin films

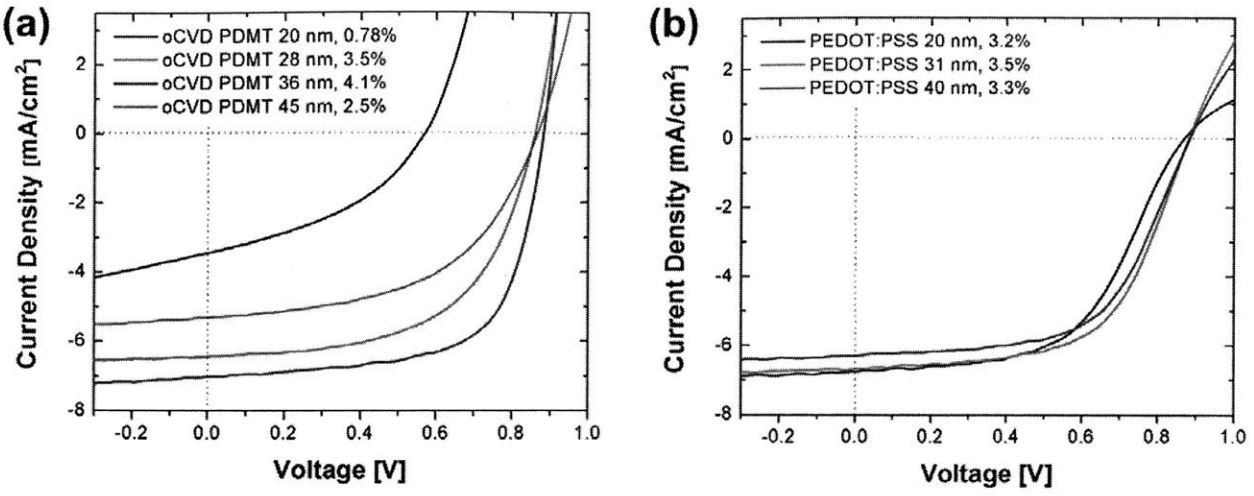

Figure 3-S3. a) Representativ J-V curves for varying PDMT HTL thickness, b) Representative J-V curves for varying PEDOT:PSS HTL thickness.

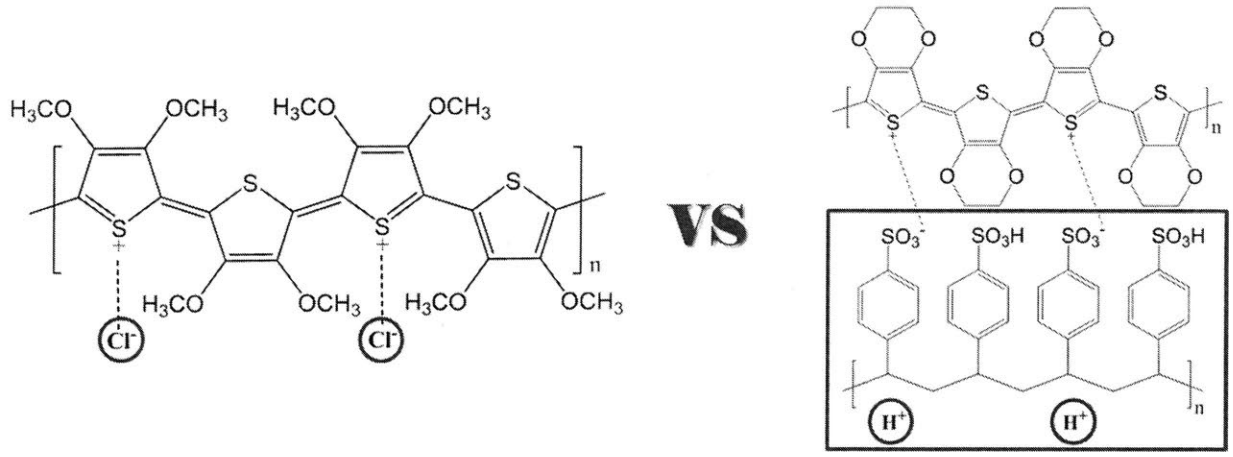

Figure 3-S4. Proton-free Cl^- anion dopants in oCVD-processed PDMT vs. Proton-generating PSS dopants in spin-coated PEDOT:PSS.

S	Cl	O	C
1 ± 0.053	1.01 ± 0.033	2.66 ± 0.5	7.456 ± 0.94

Table 3-S1. Atomic ratio (mean ± standard deviation) estimated using XPS

3.5.Conclusions

In conclusion, oCVD unlocks the potential of PDMT in organic electronics by securing a solvent-free facile path to fabricate conformally patterned PDMT thin films on diverse substrates for the first time. Here we have demonstrated PDMT thin films incorporated into DBP/C_{60} solar cells, as neutral HTLs create a suitable alternative to acidic PEDOT:PSS HTLs. The oCVD-processed PDMT HTL exhibits the highest reported J_{SC}, FF, and PCE of single-bilayer DBP/C_{60} solar cells as a result of its good conductivity, high transparency, appropriate energy levels, and neutrality. Notably, oCVD PDMT coating's conformal and dry nature with anion dopant injection capability creates a hole transport-favorable interface, minimizing dipoles/carrier traps, scattering effects, interfacial energy barrier, dewetting defects, carrier recombination, and thus leakage currents. Consequently, the high-quality ohmic contact with minimized R_S and maximized R_{Sh} is formed between DBP and ITO, to upgrade the J_{SC}, FF, and PCE. Furthermore, the neutral nature of oCVD-processed PDMT remarkably extends the solar cell lifetime. These outcomes represent the first example to substantiate the concept of a neutral hole transporting polymer, which is promising for achieving enhanced solar cell efficiency and lifetime. Finally, the findings from this study are also applicable for other categories of electronic devices with different architectures (e.g., inorganic solar cells, quantum dot solar cells, perovskite solar cells, organic light emitting diodes, thermoelectric devices, and photoelectrochemical cells), because

oCVD is a versatile polymer-coating technique, independent of material solubility and substrate properties.[21]

3.6.References

[1] T. R. Cook, D. K. Dogutan, S. Y. Reece, Y. Surendranath, T. S. Teets, D. G. Nocera, *Chem. Rev.* **2010**, *110*, 6474.

[2] W. J. Jo, J.-W. Jang, K. Kong, H. J. Kang, J. Y. Kim, H. Jun, K. P. S. Parmar, J. S. Lee, *Angew. Chem. Int. Ed.* **2012**, *51*, 3147.

[3] W. J. Jo, H. J. kang, K. Kong, Y. S. Lee, H. Park, Y. Lee, T. Buonassisi, K. K. Gleason, J. S. Lee, *Proc. Natl. Acad. Sci. U.S.A.* **2015**, *112*, 13774.

[4] J. Y. Kim, K. Lee, N. E. Coates, D. Moses, T. Nguyen, M. Dante, A. J. Heeger, *Science* **2007**, *317*, 222.

[5] M. Kim, J. H. Park, J. H. Kim, J. H. Sung, S. B. Jo, M. Jo, K. Cho, *Adv. Energy Mater.* **2015**, *5*, 1401317.

[6] J. Lee, R. Singh, D. H. Sin, H. G. Kim, K. C. Song, K. Cho, *Adv. Mater.* **2016**, *28*, 69.

[7] W. J. Jo, D. C. Borrelli, V. Bulović, K. K. Gleason, J. S. Lee, *Org. Electron.* **2015**, *26*, 55.

[8] Z. He, C. Zhong, S. Su, M. Xu, H. Wu, Y. Cao, *Nature Photon.* **2012**, *6*, 591.

[9] S. Lattante, *Electronics* **2014**, *3*, 132.

[10] H. Park, R. M. Howden, M. C. Barr, V. Bulović, K. Gleason, J. Kong, *ACS Nano* **2012**, *6*, 6370.

[11] J. W. Jung, C. Chueh, A. K. Jen, *Adv. Mater.* **2015**, *27*, 7874.

[12] J. P. Thomas, L. Zhao, D. McGillivray, K. T. Leung, *J. Mater. Chem. A* **2014**, *2*, 2383.

[13] E. Voroshazi, B. Verreet, A. Buri, R. Müller, D. Di, P. Heremans, *Org. Electron.* **2011**, *12*, 736.

[14] H. Park, S. Chang, J. Jean, J. J. Cheng, P. T. Araujo, M. Wang, M. G. Bawendi, M. S. Dresselhaus, V. Bulović, J. Kong, S. Gradečak, *Nano Lett.* **2013**, *13*, 233.

[15] M. P. de Jong, L. J. van IJzendoorn, M. J. A. de Voigt, *Appl. Phys. Lett.* **2000**, *77*, 2255.

[16] C. G. Overberger, J. Lal, *J. Am. Chem. Soc.* **1951**,

[17] M. Fall, L. Assogba, J.-J. Aaron, M. . Dieng, *Synth. Met.* **2001**, *123*, 365.*73*, 2956.

[18] A. Szkurlat, B. Palys, J. Mieczkowski, M. Skompska, *Electrochim. Acta* **2003**, *48*, 3665.

[19] G. Zotti, S. Zecchin, G. Schiavon, L. B. Groenendaal, *Chem. Mater.* **2000**, *12*, 2996.

[20] D. Bhattacharyya, K. K. Gleason, *J. Mater. Chem.* **2012**, *22*, 405.

[21] A. M. Coclite, R. M. Howden, D. C. Borrelli, C. D. Petruczok, R. Yang, J. L. Yagüe, A. Ugur, N. Chen, S. Lee, W. J. Jo, A. Liu, X. Wang, K. K.Gleason, *Adv. Mater.* **2013**, *25*, 5392.

[22] T. A. Skotheim, R. L. Elsenbaumer, J. R. Reynolds, *Handbook of Conducting Polymers*, Marcel Dekker Inc., New York, NY, USA **1998**.

[23] C. M. Cardona, W. Li, A. E. Kaifer, D. Stockdale, G. C. Bazan, *Adv. Mater.* **2011**, *23*, 2367..

[24] Y. Peng, L. Zhang, T. L. Andrew, *Appl. Phys. Lett.* **2014**, *105*, 083304.

[25] M. C. Barr, R. M. Howden, R. R. Lunt, V. Bulović, K. K. Gleason, *Adv. Energy Mater.* **2012**, *2*, 1404.

[26] Z. Yin, Q. Zheng, S. Chen, D. Cai, Y. Ma, *Adv. Energy Mater.* **2015**, 1501493.

CHAPTER FOUR

Phase Transition-Induced Band Edge Engineering of $BiVO_4$ to Split Pure Water under Visible Light

This chapter is adapted and reprinted with permission from: Won Jun Jo, Hyun Joon Kang, Ki-jeong Kong, Yun Seog Lee, Hunmin Park, Younghye Lee, Tonio Buonassisi, Karen K. Gleason, and Jae Sung Lee, *Phase Transition-Induced Band Edge Engineering of $BiVO_4$ to Split Pure Water under Visible Light,* **Proceedings of the National Academy of Sciences**, 112(45), 13774-13778 (2015).

4.1. Abstract

Through phase-transition induced band edge engineering via dual doping with In and Mo, a novel 'greenish' $BiVO_4$ ($Bi_{1-x}In_xV_{1-x}Mo_xO_4$) is developed that has a larger band-gap energy than usual 'yellow' scheelite-monoclinic $BiVO_4$ as well as higher (more negative) conduction band than H^+/H_2 potential (0 V_{RHE} at pH 7). Hence, it can extract H_2 from pure water via visible light-driven overall water splitting without using any sacrificial reagents. The density functional theory calculation indicates that In^{3+}/Mo^{6+} dual doping triggers partial phase transformation from pure *m*-$BiVO_4$ to a mixture of *m*-$BiVO_4$ and *t*-$BiVO_4$, which sequentially leads to unit-cell volume growth, compressive lattice-strain increase, conduction-band edge uplift, and band-gap widening.

4.2. Introduction

Photocatalytic water splitting, with a particulate semiconductor powered by sunlight, is an ideal route to large-scale renewable hydrogen production because of its extreme simplicity. Yet it is challenging because it requires a rare photocatalyst that carries a combination of suitable band-gap energy, appropriate band positions, and photochemical stability.[1-5] Thus, reproducible photocatalytic systems for visible light-driven overall water splitting (OWS) *via* one-step photoexcitation are also rare although there were several reports of such systems (4-6). In the best known successful case, Domen *et al.* reported in 2005 that a solid solution of GaN and ZnO, $(Ga_{1-x}Zn_x)(N_{1-x}O_x)$, was a stable photocatalyst that could split water into H_2 and O_2 under visible light when modified with a cocatalyst.[5] This system remains the most active and reproducible one-step OWS photocatalyst responsive to visible light so far.[4]

Scheelite-monoclinic $BiVO_4$ is a well-documented photocatalyst having suitable band-gap energy (E_g ~ 2.4 eV) for absorbing visible light,[7-10] and chemically stable in aqueous solution under light irradiation. Thus, it functions as an excellent photocatalyst for O_2 evolution under visible light in the presence of an appropriate electron acceptor (*e.g.* $AgNO_3$). But because the bottom of its conduction band is located at a

more positive potential than the potential of water reduction (0 V_{RHE} at pH 7), it is incapable of evolving H_2. In addition, it shows poor charge-transport characteristics[11] and weak surface adsorption properties[12] causing low photocatalytic activity. In order to overcome these weaknesses, a variety of strategies such as hetero-junction structure formation,[11,13,14] loading co-catalysts,[8,15-17] and impurity doping[1,7,12,18-23] has been attempted. These strategies were successful in improving $BiVO_4$'s oxidation capability for photo-electrochemical (PEC) water oxidation[1,11,13,15,19,24-28] as well as Z-scheme (two-photon excitation) water splitting system.[29] Also, co-catalyzed $Bi_xY_{1-x}VO_4$ (x~0.5)[7,8] and co-catalyzed $Bi_{0.5}La_{0.5}VO_4$[23] promoted OWS by raising the conduction band edge position, but OWS under visible light irradiation over $BiVO_4$-based photocatalysts has not been fully demonstrated

To meet this challenge, we developed 'greenish' $BiVO_4$ ($GBVO_x$, x = atom ratio of In and Mo), $Bi_{1-x}In_xV_{1-x}Mo_xO_4$, by simultaneously substituting In^{3+} for Bi^{3+} and Mo^{6+} for V^{5+} in the host lattice of monoclinic $BiVO_4$. The new $GBVO_x$ photocatalyst has a slightly larger band-gap energy than usual 'yellow' scheelite-monoclinic $BiVO_4$ as supported by the unique color change to green, and higher (more negative) conduction band than H^+/H_2 potential (0 V_{RHE} at pH 7). Consequently, as depicted in **Figure 4-1**, $GBVO_x$ is able to split water into H_2 and O_2 under visible-light irradiation without using any sacrificial reagents (*e.g.*, CH_3OH or $AgNO_3$). Herein, we report the dual metal doping effects on the optical absorption behavior, crystal structure, and band structure of $BiVO_4$, which led to one-photon OWS under visible-light irradiation. We elucidate the physical origin of the augmented photo-response behaviors of $GBVO_x$ through density functional theory (DFT) calculation of electronic structure as well as a variety of physical and electrochemical characterizations.

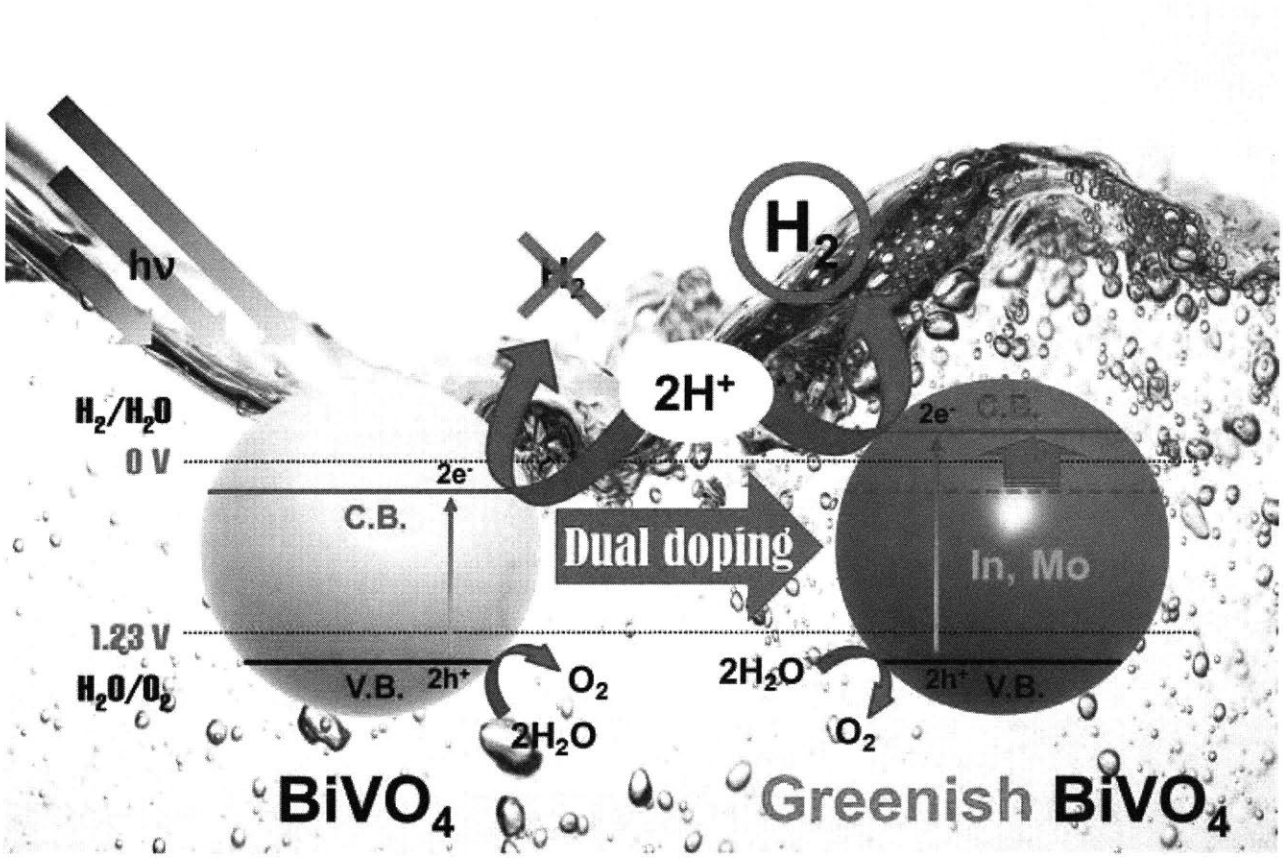

Figure 4-1. Overall water splitting reaction mechanism by greenish $BiVO_4$.

4.3.Experimental Methods

4.3.1. Sample Preparation

Powder samples of $GBVO_x$ were prepared via solid state reaction. Each stoichiometric amount of bismuth oxide (Aldrich, 99.999%), vanadium oxide (Aldrich, 98%), indium oxide (Alfa Aeser 99.9%) and molybdenum oxide (Aldrich, 99.99%) was mixed well by grinding in an agate mortar and manually pelletized under 2500 psi. All pellets were preheated at 873 K for 5 hours, and then they were vigorously reground and manually re-pelletized as mentioned earlier. These

pellets were heated again at 1073 K for 3 hours. After this main heating, they were thoroughly reground to get powder samples.

4.3.2. Modification of $GBVO_{0.10}$ with RuO_2

$GBVO_{0.10}$ was modified by photo-depositing 3 wt% RuO_2 (the loading had been optimized). Specifically, the photo-deposition was carried out at room temperature under atmospheric pressure in closed Pyrex glass vessel containing nitrogen purged suspension of $GBVO_{0.10}$ powder and $RuCl_36H_2O$ in 50 ml methanol and 50 ml distilled water under visible-light irradiation for 8 hours. The light source was a Hg-arc lamp (500W, Oriel) equipped with a UV cut-off filter ($\lambda \geq$ 420 nm). After this photo-deposition, RuO_2 loaded $GBVO_{0.10}$ was vacuum-filtered, washed with distilled water, and dried in an air oven at 70 °C for 12 hours. Finally, the dried powder sample was heated at 623 K for 1 hour.

4.3.3. Physicochemical Characterization

The structural properties of $GBVO_x$ were investigated by using powder X-ray diffraction (XRD, Phillips, X'pert Pro). Rietveld analysis was performed using X'pert Plus 3.0 software (PANalytical) to calculate the phase ratios of monoclinic structure to tetragonal structure in $GBVO_x$. The UV-visible diffuse reflectance spectra were measured with UV-visible spectrometer (UV-2401PC, Shimadzu Co.) equipped with integrated sphere method. The particle size and morphology was examined by field emission scanning electron microscopy (FESEM, JEOL JSM-6330F). The high-resolution transmission electron microscopy (HR-TEM) images, high-angle annular dark field (HAADF) images and corresponding elemental mapping images were obtained by using Cs-corrected high-resolution scanning transmission electron microscopy

(Cs-corrected HR-STEM, Jeol, JEM 2200FS, 200 kV) at the National Research Center for Nanomaterial Technology at POSTECH in Korea. The atomic ratios of bismuth to indium and vanadium to molybdenum in $GBVO_x$ were analyzed by utilizing inductively coupled plasma (ICP).

4.3.4. Photocatalytic Activity Measurement under Visible Light Irradiation

The structural properties of $GBVO_x$ were investigated by using powder X-ray diffraction The photocatalytic activities under visible light were investigated by measuring H_2 and O_2 evolution at room temperature under atmospheric pressure in closed Pyrex glass vessel (193.5 ml, 187 ml and 189 ml) containing nitrogen purged suspension of 0.3 g photocatalyst powder in 100 ml distilled water. The light source was a Hg-arc lamp (450W, Oriel) equipped with a UV cut-off filter ($\lambda \geq 420$ nm). The evolved amounts of H_2 and O_2 were analyzed by a gas chromatograph (HP5890) with a thermal conductivity detector (TCD) and a molecular sieve 5-A column.

4.3.5. Flat-band position and IPCE measurement with fabricated photoelectrodes

Photoelectrodes for flat-band potential and incident photon to charge carrier efficiency (IPCE) measurement were fabricated by typical electrophoretic deposition (EPD) method. The sample and iodine were added in acetone, and well dispersed by sonication and stirring. EPD was performed onto 1x1 cm^2 area of FTO glass (Pilkington, TEC 8, ~8Ω/square) at 55 V for 5 min with another FTO glass as a counter electrode. The photoelectrode was washed with absolute acetone after EPD and then sintered in a furnace at 400 °C for 30 min in the air. Copper wires

were attached with silver paste and all exposed conducting parts except deposited sample were covered with epoxy resin.

Mott-Schottky plot was obtained by using a potentiostat (IviumStat, Ivium Technologies) at applied frequency of 500 Hz under dark condition. The flatband potential (ϕ_{fb}) can be determined using the x-intercept of the following equation:

$$\frac{1}{C^2} = \left(\frac{2}{e\epsilon_0\epsilon_r N_d A^2}\right)\left(\phi - \phi_{fb} - \frac{kT}{e}\right)$$

where C is the differential capacitance of the space-charge region, ϵ_r is the relative dielectric constant of sample, ϵ_0 is the permittivity of the vacuum, N_d is the donor density, ϕ is the applied potential and k is the Boltzmann constant. The conduction band position is assumed to be same with the flatband potential for n-type semiconductor. The valence band position is induced by adding the band gap energy.

IPCE was evaluated utilizing a quantum efficiency measurement system (QEX7, PV Measurement) and potentiostat (Reference 600, Gamry) at 10 nm wavelength scanning rate with 5 second measurement. 3-electrode system was commonly used with Pt mesh, Ag/AgCl, and 0.5M Na_2SO_4 solution as a counter electrode, reference electrode, and electrolyte, respectively to estimate flat-band potential and IPCE.

4.3.6. Quantum yield measurements

The quantum yield of the 10% (In, Mo)-doped sample was calculated by the chemical actinometry of potassium ferrioxalate ($K_3(Fe(C_2O_4)_3)\cdot 3H_2O$) (33, 34). For the preparation of $K_3(Fe(C_2O_4)_3)\cdot 3H_2O$, 1.5M $K_2C_2O_4$ and 1M $FeCl_3$ in water solution were mixed and recrystallized two times resulting in green precipitate. The solution of 6 mM

$K_3(Fe(C_2O_4)_3)\cdot 3H_2O$ in 50 mM sulfuric acid solution was irradiated under the same condition as that for photocatalytic activity measurements for 2 minutes. The irradiated solution was mixed with $NaCH_3COO\cdot 3H_2O$ buffer solution and 0.1% 1,10-phenanthroline solution as a color indicator. Non-irradiated solution was also prepared for comparison. The absorbance at 510 nm of the final complex solution was measured by UV-Vis-NIR spectrophotometer (Cary 5000, Varian) with a cell of 1 cm length. Photon flux is given by:

$$q = \frac{\Delta A\, V_1\, V_3}{\Phi(\lambda)\varepsilon(\lambda)V_2\, l\, t}$$

where ΔA = absorbance difference between irradiated and non-irradiated solutions, V_1 = the irradiated volume, V_2 = the sampling volume for complexation with phenanthroline, V_3 = the final volume after the complexation, l = the optical pathlength of the irradiation cell, t = the irradiation time, $\Phi(\lambda)$ = the quantum yield of ferrous ion production (1.11 at 510nm), and $\varepsilon(\lambda)$ = absorption coefficient (11100 $dm^3\ mol^{-1}\ cm^{-1}$ at 510 nm). The final apparent quantum yield is given by:

$$\text{A. Q. Y. (\%)} = \frac{\text{Number of reacted electrons}}{\text{Number of incident photons}} \times 100$$

4.3.7. Turnover number calculations

We have evaluated the turnover number for visible light-driven overall water splitting reactions shown in **Figure 4-3** to justify the stability and durability of RuO_2 deposited on $GBVO_{0.10}$. Since it is difficult to define the active site exactly and to determine its number for photocatalytic reactions, the total number of species (RuO_2 or $GBVO_{0.10}$) is used for the calculation following the previous published reference.[35] Thus, the obtained turnover numbers (TON) are low limits of the real value.

	$GBVO_{0.10}$ (Phase I) for 10 hrs	$RuO_2/GBVO_{0.10}$ (Phase II-IV) for 30 hrs	Heated $RuO_2/GBVO_{0.10}$ (Phase V) for 10 hrs
Tot. moles of H_2 produced (μmol)	23.05	374	142
Tot. $GBVO_{0.10}$ moles (mol)	9.40×10^{-4}	9.12×10^{-4}	9.12×10^{-4}
Tot. RuO_2 moles (mol)	-	6.76×10^{-5}	6.76×10^{-5}
TON w.r.t. $GBVO_{0.10}$	**0.0490**	**0.820**	**0.312**
TON w.r.t. RuO_2	**-**	**11.1**	**4.21**
TOF w.r.t. $GBVO_{0.10}$ (h^{-1})	0.00490	0.0273	0.0312
TOF w.r.t. RuO_2 (h^{-1})	-	0.370	0.421

Table 4-1. Turnover number for Phase I, Phase II-IV, and Phase V

Turnover number (TON) = [the number of produced hydrogen atoms] / [the total moles of RuO_2 or $GBVO_{0.10}$]. Turnover frequency (TOF) = TON/time.

Hence, on the most reasonable basis (the moles of co-catalyst RuO_2), the continuous operation in Phase II-IV correspond to TON of 11.1 and a turnover frequency of 0.37 h^{-1}.

4.3.8. Lattice-strain evaluations

a. Volumetric strain method

The principle of volumetric strain method has already been described in detail elsewhere such as any relevant textbooks. The following description for volumetric strain is just a brief version of the contents from some lecture notes. Strain is related to change in dimensions and shape of a

material. When the deformation is along one axis, the most elementary definition of stain is as follows:

$$\text{strain} = \text{change in length} / \text{original length}$$

When a material is stretched, the change in length and the strain are positive. When it is stretched, the change in length and the strain are negative. This conforms with the signs of the stress which would accompany these strains, tensile stresses being positive and compressive stresses negative. Likewise, we define volumetric strain e as:

$$e = \text{change in volume} / \text{original volume}$$

The volumetric strain is simply related to the normal strains. Consider a rectangular solid, whose original volume is given by $V_0 = xyz$. When the solid is deformed, the resulting volume is given by

$$V = x(1 + \varepsilon_x)y(1 + \varepsilon_y)z(1 + \varepsilon_z) = xyz(1 + \varepsilon_x + \varepsilon_y + \varepsilon_z + \varepsilon_x\,\varepsilon_y + \varepsilon_x\,\varepsilon_z + \varepsilon_y\,\varepsilon_z + \varepsilon_x\,\varepsilon_y\,\varepsilon_z)$$

$$\text{If } |\varepsilon_x| < 1 \;\&\; |\varepsilon_y| < 1 \;\&\; |\varepsilon_z| < 1,$$

$$V \approx xyz(1 + \varepsilon_x + \varepsilon_y + \varepsilon_z) = V_0(1 + \varepsilon_x + \varepsilon_y + \varepsilon_z)$$

Now, the volumetric strain becomes

$$e = (V - V_0) / V_0 = \varepsilon_x + \varepsilon_y + \varepsilon_z$$

b. Williamson-Hall method

The crystallite size (D) can be calculated using the Scherrer's equation[36]:

$$D = k\lambda / (\beta_D \cos\theta)$$

where k is the shape coefficient (0.9), λ is the wavelength of the incident radiation (1.541874 nm), β_D is the peak broadening due to small crystallite size, and θ is the Bragg angle. β_D can be expressed as[37]

$$\beta_D^2 = \beta_{measures}^2 - \beta_{instrumental}^2$$

where $\beta_{measures}$ is the measured peak broadening from XRD patterns, $\beta_{instrumental}$ is the instrumental peak broadening. The peak broadening (β_S) due to lattice strain ($\varepsilon = \Delta d/(2d)$) can be estimated as (37)

$$\beta_S = 4\varepsilon \tan\theta$$

By using the Williamson-Hall plotting method, the contribution of crystallite size and lattice strain can be separated (38).

$$\beta\cos\theta = k\lambda/D + 4\varepsilon \sin\theta$$

where β is the sum of the peak broadenings due to the lattice strain and crystallite size ($\beta = \beta_D + \beta_S$).

4.4. Results and Discussion

4.4.1. Physical properties of greenish $BiVO_4$

The magnified X-ray diffraction (XRD) patterns of pristine $BiVO_4$ and four $GBVO_x$ samples with different target atom ratios (x = 0.02, 0.05, 0.10, and 0.15) are shown in **Figure 4-2a** (**Figure 4-S1a, b, c, and d** for more details) to identify the evolution of the crystal structure by doping. Split peaks around 35° are merged into one peak as the dopant ratio (x) increases, indicating phase change of $BiVO_4$ from monoclinic (*m*-) to tetragonal (*t*-) (11). Further, Rietveld analysis was performed using X'pert Plus 3.0 software (PANalytical) to determine the fraction of *m*- and *t*-phases, as illustrated in **Figure 4-2b** and **Figure 4-S2**. As the dopant ratio (x in $GBVO_x$) increases, the crystal structure evolves from almost pure m-$BiVO_4$ (clinobisvanite; space group: 12/a/(15), JCPDS card No. 014-0688) to a mixture of *m*- and *t*-$BiVO_4$, where *t*-$BiVO_4$ fraction reaches a maximum of 60% at x = 0.10. This doping-induced crystal structure evolution results

in unit-cell volume growth (**Figure 4-2b**) that generates compressive lattice strain, as discussed in S4 of SI and visualized in **Figure 4-S1e and f.** In particular, the compressive lattice strain is the key physical driving force to lift the conduction band of $GBVO_x$ over H^+/H_2 potential (0 V_{RHE} at pH 7), taking collectively both experimental (**Figure 4-S1e and f**) and theoretical findings (as discussed later).

The UV/Vis absorption spectra of all samples are demonstrated in **Figure 4-2c**. With higher x values of $GBVO_x$, the greater blue shift is observed, indicating that the optical band-gap energy of $GBVO_x$ increases with dopant level, whereas the blue shift is not caused by the single Mo doping into $BiVO_4$ (**Figure 4-S4f**). Actually, the blue-shift trend is consistent with the band-gap energy transition estimated by extrapolating the linear part of $(\alpha h\upsilon)^2$ *vs.* $h\upsilon$ plot to the energy axis (1) as shown in **Figure 4-S3**. According to the Tauc plot, the band-gap energy increases from 2.43 eV of pristine $BiVO_4$ to 2.50 eV of $GBVO_{0.10}$. Furthermore, the alteration in the optical band-gap energy corresponds to the color evolution of $GBVO_x$ powder samples from yellow to greenish as shown in **Figure 4-2c** (inset) and S4. Thus, the ultimate physical driving force for the apparent color evolution is also the compressive lattice strain that widens the band-gap by lifting the conduction band. The Mott-Schottky plot in **Figure 4-2d** displays that the conduction band of $GBVO_{0.10}$ is elevated to higher than 0 V (vs. RHE at pH 7) by 97.2 mV or *ca.* 151 mV from that of pristine $BiVO_4$ (See **Figure 4-S5** for more clear visualization of the contrast between schematic band structures of pristine $BiVO_4$ and $GBVO_{0.10}$). This finding indicates that photocatalytic water reduction, impossible with pristine $BiVO_4$, becomes possible with $GBVO_{0.10}$, as the dual doping lifts the conduction band edge above the proton reduction potential of 0 V_{RHE} (at pH 7). For the valance band of $GBVO_{0.10}$, it is 81 mV higher than that of pristine

$BiVO_4$, but it is still far below the water oxidation potential of 1.23 V_{RHE} (at pH 7) as shown in **Figure 4-S5**.

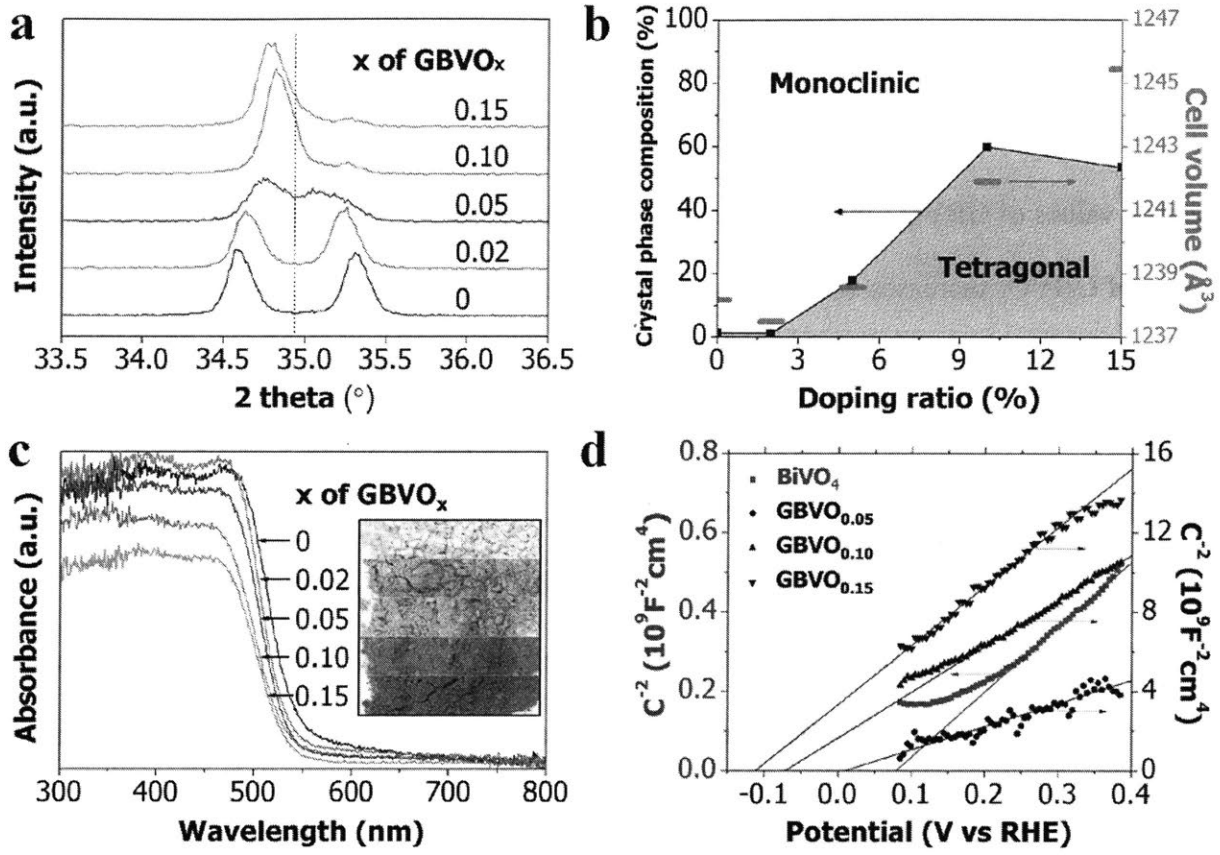

Figure 4-2. Photophysical characterization of $GBVO_x$. a) Magnified view of powder X-ray diffraction patterns of pristine $BiVO_4$ and all $GBVO_x$ samples. b) Crystal phase diagram with calculated unit cell volume for different x of $GBVO_x$. c) UV/Vis absorption spectra of pristine $BiVO_4$ and all $GBVO_x$ samples and inset demonstrating color change of the samples. d) Mott-Schottky plot of pristine $BiVO_4$, $GBVO_{0.05}$, $GBVO_{0.10}$, and $GBVO_{0.15}$.

The field emission scanning electron microscopy (FE-SEM) images in **Figure 4-S6** reveal that all samples consist of irregular polyhedrons of unsystematic size distribution, typical

of powder samples synthesized via solid-state reactions. The real atomic ratios in all $GBVO_x$ samples determined by the inductively coupled plasma (ICP) analysis in **Table 4-2** are close enough to the target values. The high resolution transmission electron microscopy (HR-TEM) and energy dispersive X-ray spectroscopy (EDS) elemental mapping in **Figure 4-S7, 8, 9, and 10** demonstrate that Bi, V, In, and Mo are homogeneously distributed within the $GBVO_x$ particle. All these characterization results univocally prove that In^{3+} and Mo^{6+} have been effectively inserted into the $BiVO_4$ lattice. The HR-TEM image in **Figure 4-S9f** illustrates the lattice spacing of 0.450 nm corresponding to the inter-planar spacing of (040) plane of $GBVO_{0.10}$. XPS binding energies in **Figure 4-S11** indicate that the involved elements are all in their stable oxidation states of Bi^{3+}, V^{5+}, Mo^{6+}, and In^{3+}.

4.4.2. Overall water splitting under visible light

The OWS reaction was carried out under visible-light irradiation ($\lambda \geq 420$ nm, 500 W Hg-arc lamp) with 0.3 g of photocatalyst powder dispersed in 100 ml of distilled water of pH 7. In phase 1 of **Figure 4-3**, $GBVO_{0.10}$ (the most active $GBVO_x$) demonstrated stoichiometric H_2/O_2 evolution even without modification by any co-catalyst. Hence, the greenish $BiVO_4$ can split pure water via visible light-driven OWS without any sacrificial reagents or additives. In particular, this represents the first example of pure water-splitting photocatalyst responding to visible light without any metal co-catalyst. Next we purged the system with N_2, and tested OWS reaction after photo-depositing 3 wt% RuO_2 on $GBVO_{0.10}$ as a co-catalyst. The photocatalytic activity was significantly improved by adding a RuO_2 co-catalyst that collects electrons/holes and provides active sites for catalytic water reduction and/or oxidation. The other common co-catalysts such as Pt, Rh, $Rh_xCr_yO_3$, and $Pt_xCr_yO_3$ (4-6) were much less effective on $GBVO_{0.10}$.

Phases II-IV present repeated runs of the same catalysts to demonstrate the stability of $GBVO_{0.10}$. In phase V, heat treatment (623 K in air for 1 h) further intensified the photocatalytic activity of RuO_2 co-catalyzed $GBVO_{0.10}$. This treatment was aimed at converting the photo-deposited $RuO_2 \cdot xH_2O$ on $GBVO_{0.10}$ into the more stable and active form of co-catalyst, *i.e.* RuO_2 (30).

The rate of hydrogen evolution (~17 μmol h^{-1}) from this 3 wt% RuO_2 on $GBVO_{0.10}$ could be compared with that of the best-known example (~56 μmol h^{-1}), *i.e.* 5 wt% RuO_2-loaded $(Ga_{1-x}Zn_x)(N_{1-x}O_x)$ under visible light irradiation ($\lambda \geq 400$ nm, 450 W Hg-arc lamp) (5). The activity of our photocatalyst corresponds to an apparent quantum yield (A.Q.Y.) of 3.2% under overall visible-light (420-800nm) irradiation, which was calculated from the amount of evolved hydrogen and photon flux measured by chemical actinometry with ferrioxalate (See S3 of SI for details). The value is also compared to 5.9% at 420-440 nm for $(Ga_{1-x}Zn_x)(N_{1-x}O_x)$ photocatalysts (31). Considering we used a longer wavelength filter ($\lambda \geq 420$ nm), we can state that the photocatalytic activity of $GBVO_{0.10}$ is comparable to that of the best known $(Ga_{1-x}Zn_x)(N_{1-x}O_x)$ photocatalyst. But this work represents the first report of visible light-driven OWS over modified $BiVO_4$ in pure water of pH 7 and without co-catalyst. This also represents the first OWS photocatalyst based on d(0) electron configuration (V^{5+}), whereas $(Ga_{1-x}Zn_x)(N_{1-x}O_x)$ is made of d(10) configuration (Zn^{2+}, Ga^{3+}). The incident photon to current conversion efficiency (IPCE) was measured for unmodified $GBVO_{0.10}$ film (See S2 for details). As shown in **Figure 4-S12**; IPCE of 0.5-2% is observed in 350-480 nm with the shape of its curve well reflecting the absorption spectrum in **Figure 4-2c**. It confirms that the photo-response of the material corresponds to light absorption by the band-to-band transition.

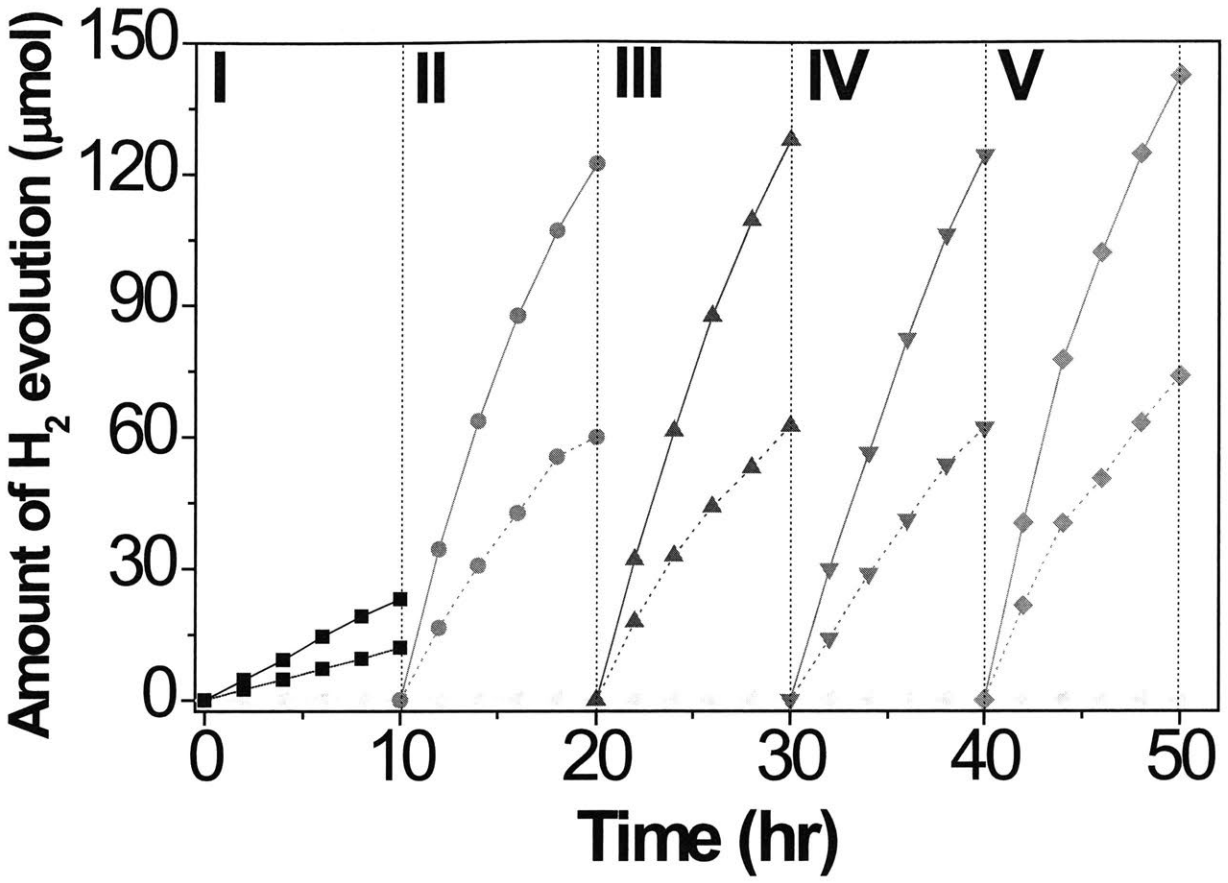

Figure 4-3. Overall water splitting by $GBVO_{0.10}$ under the visible-light ($\lambda \geq 420$ nm) irradiation. Phase I) Unmodified $GBVO_{0.10}$, Phase II-IV) 3 wt% $RuO_2/GBVO_{0.10}$, and Phase V) heat treated 3 wt% $RuO_2/GBVO_{0.10}$. Solid and dashed lines indicate evolved H_2 and O_2, respectively. Base line represents a control experiment by pristine $BiVO_4$.

In order to understand the nature of the photocatalytic water splitting with $GBVO_x$ in more detail, its half reactions were studied in the presence of sacrificial reagents. Namely, Ag^+ ions from $AgNO_3$ act as electron scavengers and CH_3OH acts as a hole scavenger:

$$2H_2O(l) + h\nu + 4Ag^+ \rightarrow O_2(g) + 4H^+ + 4Ag^0$$

$$H_2O(l) + h\nu + CH_3OH \rightarrow 3H_2(g) + CO_2(g).$$

In **Figure 4-S13a**, O_2 evolution rates increased greatly with the single Mo doping ($BiV_{0.98}Mo_{0.02}O_4$). This is due to the improved charge transfer properties of $BiVO_4$ as reported earlier (21). However, the dual metal doping improved the water oxidation activity much further showing a maximum at the low doping level of $GBVO_{0.02}$. According to the numerical data from **Figure 4-S13a**, $GBVO_{0.02}$ has dramatically increased photocatalytic water oxidation activity by a factor of about 20 and 5 relative to pristine $BiVO_4$ and single-doped $BiV_{0.98}Mo_{0.02}O_4$, respectively. **Figure 4-S14** shows that the single In doping did not induce any tetragonal phase formation. But it increased the rate of O_2 evolution in $Bi_{0.99}In_{0.01}VO_4$ and reduced the rate at higher In doping level of $Bi_{0.98}In_{0.02}VO_4$.

As **Figure 4-S13b** exhibits, the effects of doping on H_2 evolution were quite different from those of doping on O_2 evolution. Neither the single doping of Mo^{6+} or In^{3+}, nor the low level of dual doping (x = 0.02) produced H_2. The optimum doping level for H_2 evolution was found to be x = 0.10. This indicates that when 10% of In^{3+}/Mo^{6+} is inserted into the $BiVO_4$ lattice, the conduction band gains more negative (higher) potential than 0 V_{RHE} (at pH 7) to achieve photocatalytic water reduction. However, even with the appropriate In^{3+}/Mo^{6+} dopant concentration (x = 0.10), the H_2 evolution rate was two-orders-of-magnitude smaller than the O_2 evolution rate. This comparison reveals that water reduction using photo-generated electrons is the rate-determining step in OWS reaction by $GBVO_{0.10}$. In this sense, the main role of RuO_2 is most likely to provide augmented reaction sites for H_2 evolution (water reduction).

The stability of $GBVO_{0.10}$ is supported by **Figure 4-S15c**, revealing no difference in the XRD patterns of $GBVO_{0.10}$ before and after 40-hour OWS reaction. The stability is also confirmed by the turnover number of RuO_2 loaded on $GBVO_{0.10}$ (number of hydrogen atoms produced / number of Ru atoms in RuO_2 as shown in **Table 4-1**). The turnover number is

estimated to be 11 during the OWS reaction phase II-IV in **Figure 4-3**, guaranteeing sustainable catalytic cycles on $GBVO_{0.10}$. However, at 15% In^{3+}/Mo^{6+} dopant concentration ($GBVO_{0.15}$), the crystal structure is damaged after 40-hour OWS reaction, as demonstrated in **Figure 4-S15c**. This inferior crystal-structure stability of $GBVO_{0.15}$ is most likely due to the too-high In^{3+}/Mo^{6+} dopant concentration of 15%. According to volumetric strain method and Williamson-Hall method discussed in the section 4.3.8 and **Figure 4-S1e and f**, the conduction band edge position is proportional to the compressive (minus) lattice stain up to 10% dopant concentration. However, the proportional relation is not valid any more at 15% dopant concentration because of the inferior crystal-structure stability at the too-high In^{3+}/Mo^{6+} doping ratio.

4.4.3. First-principle, DFT calculations

Collectively taking into account all of the experimental results from a wide array of instruments and methods, this current study has found that there is a significant positive correlation between the compressive (minus) lattice-strain and the conduction band edge at least up to 10% In^{3+}/Mo^{6+} dopant concentration. This positive correlation provides the physical driving force to transform (only) O_2-evolving yellow $BiVO_4$ into (both) H_2/O_2-evolving greenish $BiVO_4$ by lifting the conduction band edge, widening the band-gap, and entailing the apparent color change. This finding based on a variety of experimental outcomes is also corroborated by the theoretical study using DFT calculations, as follows.

The effect of In^{3+}/Mo^{6+} dual doping was investigated by first-principle, DFT electronic structure calculation on scheelite type *m*-$BiVO_4$ (space group: I2/a) and *t*-$BiVO_4$ (space group: I41/amd). The detailed calculation procedures were based on those described in previous studies (1, 32). The lattice constants as well as atomic coordinates were simultaneously optimized, and

the obtained lattice parameters for a conventional cell were a = 7.306 Å, b = 11.747 Å, c = 5.167 Å, β = 135.003° for *m*-$BiVO_4$ and a = b = 7.307 Å, c = 6.587 Å for *t*-$BiVO_4$. In order to study the effect of In^{3+}/Mo^{6+} substitution into Bi^{3+}/V^{5+} sites, we used 96-atom $BiVO_4$ host super-cell of 2a×b×2c and conventional cell of $\sqrt{2}$a×$\sqrt{2}$b×2c for *m*-$BiVO_4$ and *t*-$BiVO_4$, respectively. We examined a single pair of In and Mo atoms' substitution, *i.e.*, the doping concentration x=0.0625 in $Bi_{1-x}In_xV_{1-x}Mo_xO_4$. The calculated electronic density of states (DOS) is shown in **Figure 4-4**, where the origin of energy is set to be the valence band edge (VBE) of pristine *m*-$BiVO_4$. The energy levels of *m*-$BiVO_4$ and *t*-$BiVO_4$ with and without doping are effectively compared by aligning the deep-lying O 2s orbital levels.

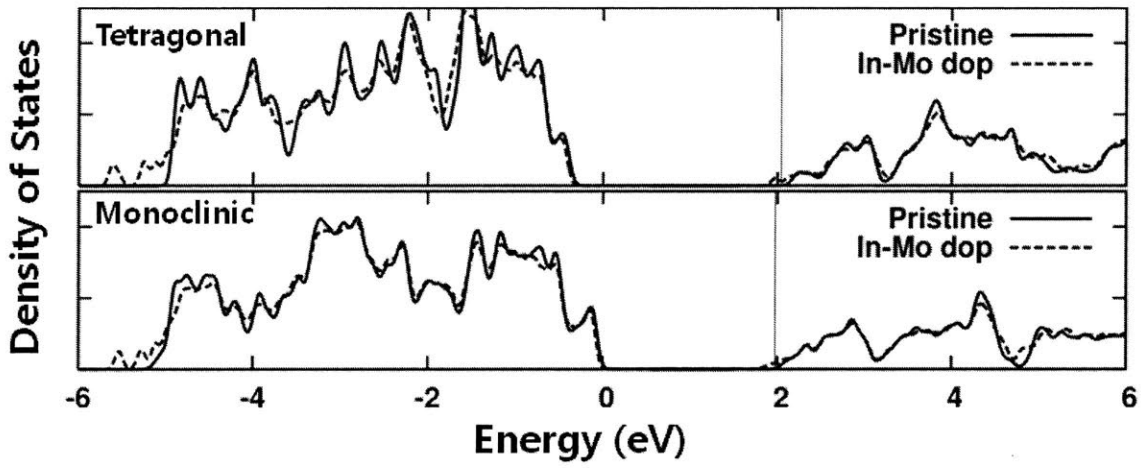

Figure 4-4. Density of states of the t-$BiVO_4$ and m-$BiVO_4$ system with and without In^{3+}/Mo^{6+} dual doping. The energy levels in different structures are aligned comparing the deep lying oxygen 2s orbital. The Fermi level of In^{3+}/Mo^{6+} doped structure lies near CBE, shown with vertical dotted lines. The VBE in tetragonal structure is -0.32 eV lower than in m-$BiVO_4$. In each crystal structure, doping causes band-gap narrowing.

For *m*-$BiVO_4$, the calculated band-gap energy is 2.02 eV without doping and 1.84 eV with doping. This means that the band-gap is slightly narrowed upon doping. The VBE of doped *m*-$BiVO_4$ is at the same energy level as that of pristine *m*-$BiVO_4$, and the conduction band edge (CBE) is 0.18 eV lower than pristine *m*-$BiVO_4$. Both of these calculations are contradictory to the experimental findings of increased band-gap energy and higher CBE induced by In^{3+}/Mo^{6+} doping. In the case of *t*-$BiVO_4$, the band-gap in the equilibrium cell volume is 2.47 eV without doping and 2.31 eV with dual doping. While the band-gap of *t*-$BiVO_4$ is larger (~0.45 eV) than that of *m*-$BiVO_4$, the CBE is slightly higher (~0.13 eV) than its counterpart, because the average electronic potential is deeper (work function is higher) in *t*-$BiVO_4$ compared with in *m*-$BiVO_4$. Like *m*-$BiVO_4$ mentioned above, the band-gap of *t*-$BiVO_4$ narrows upon doping, and the CBE of doped *t*-$BiVO_4$ is slightly lower than that of pristine *m*-$BiVO_4$, which are also contradictory to the experimental results.

This apparent inconsistency between calculation and experiments can be solved by considering the partial phase change of *m*-$BiVO_4$ to *t*-$BiVO_4$ upon dual doping. Indeed, the best performance water splitter, $GBVO_{0.10}$, contains *ca.* 60% of tetragonal phase (**Figure 4-2b**). As the synthesized $GBVO_x$ crystal has the mixed structure of varying-fraction monoclinic and tetragonal phases with respect to the doping concentration, each crystal structure would not have its equilibrium lattice constants. The conventional cell volume of *t*-$BiVO_4$ (351.68 $Å^3$) containing four $BiVO_4$ units is quite larger than that of *m*-$BiVO_4$ (313.54 $Å^3$). The energy level alignment and the total energy variation of *m*-$BiVO_4$ and *t*-$BiVO_4$ are illustrated with respect to the cell volume in **Figure 4-5**. For doped *m*-$BiVO_4$ with larger cell volume, the band-gap is smaller than that of pristine *m*-$BiVO_4$ with the equilibrium lattice constants. Thus, only the

energy level alignment of t-$BiVO_4$ is compared to the CBE and VBE of pristine *m*-$BiVO_4$, as shown in **Figure 4-5a**. According to the comparison, compressed *t*-$BiVO_4$ with In^{3+}/Mo^{6+} substitution has larger band-gap energy as well as higher CBE position than pristine *m*-$BiVO_4$.

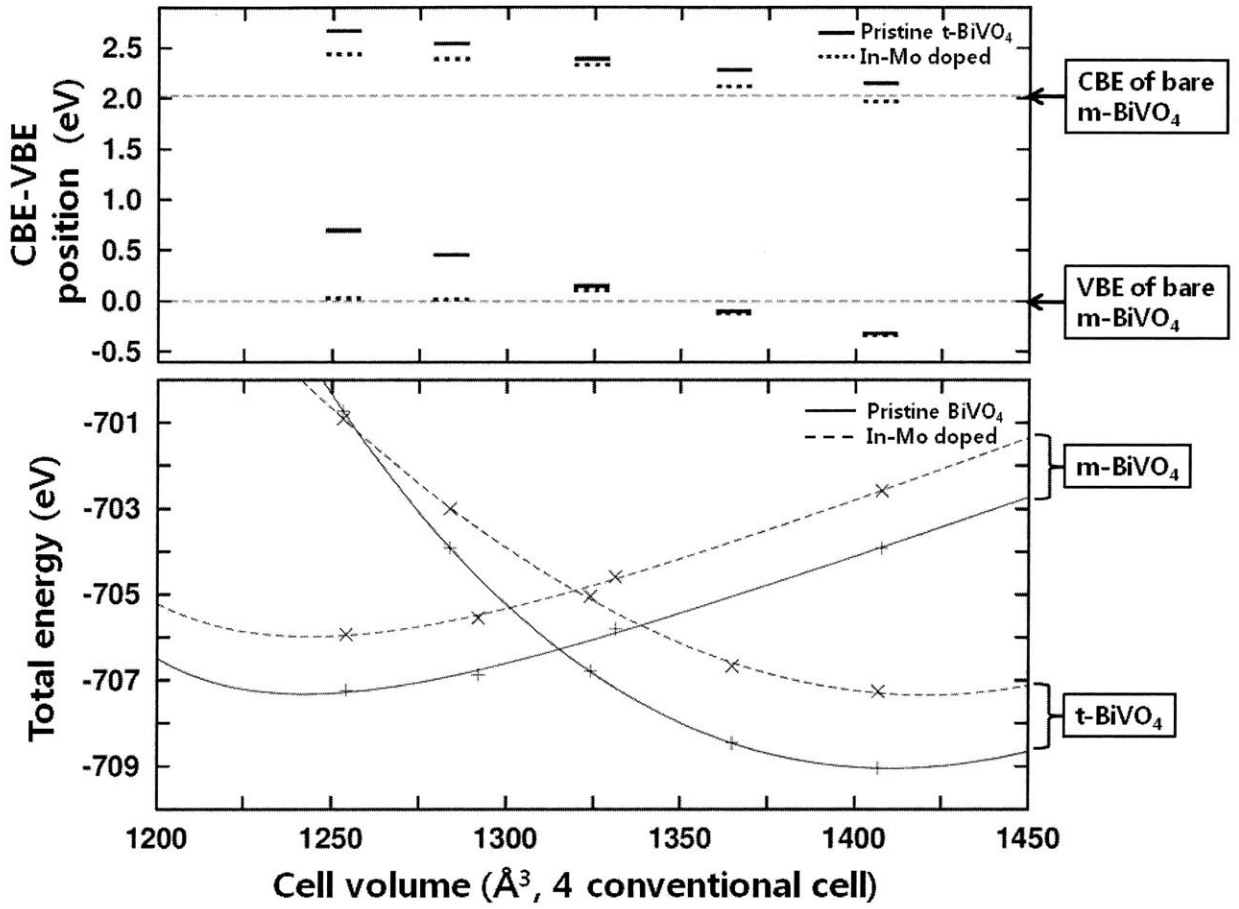

Figure 4-5. a) Cell volume dependency of CBE and VBE positions in t-$BiVO_4$ systems. The horizontal dashed lines indicate corresponding energy positions in pristine m-$BiVO_4$. b) Total energy versus cell volume plot of m-$BiVO_4$ and t-$BiVO_4$. The points are calculation results and lines stand for the Birch fit to the equation of state.

This DFT calculation outcome supports the experimental finding of higher CBE. To be more specific, In^{3+}/Mo^{6+} substitution causes partial phase transformation from pure *m*-$BiVO_4$ to a mixture of *m*-$BiVO_4$ and *t*-$BiVO_4$, and the phase transformation results in unit-cell volume growth and compressive lattice-strain increase. As a reuslt of the compressive lattice-strain increase, $GBVO_{0.10}$ (having the optimum mixed crystal structure of *ca.* 60% *t*-$BiVO_4$ and *ca.* 40% *m*-$BiVO_4$ to maximize the compressive lattice-strain) can take advantage of uplifted conduction-band edge to achieve overall water splitting under visible light without any additvies. The physical mechanism on how In^{3+}/Mo^{6+} dual doping triggers the partial phase transformation from pure *m*-$BiVO_4$ to a mixture of *m*-$BiVO_4$ and *t*-$BiVO_4$ is investigated in the following discussion.

To figure out the physical reason why tetragonal phase expands as doping concentration grows, we estimated the total energy of each case as demonstrated in **Figure 4-5b**. Based on that, we could also estimate the formation energy of In^{3+}/Mo^{6+} dual dopants, within *m*-$BiVO_4$ and *t*-$BiVO_4$ according to the cell volume, by calculating the total energy differences between pristine $BiVO_4$ and doped $BiVO_4$. There is no ambiguity to determine the chemical potentials, because the contributions of cation chemical potentials are compensated. The formation energy of In^{3+}/Mo^{6+} dopants in *m*-$BiVO_4$ is about 1.31 eV and independent of lattice strain, but that in *t*-$BiVO_4$ strongly depends on cell volume variation. The formation energy of In^{3+}/Mo^{6+} dopants in *t*-$BiVO_4$ is 1.79 eV in its equilibrium cell volume (1407 $Å^3$), which is about 0.48 eV higher than that in *m*-$BiVO_4$ at 1253 $Å^3$. However, as the cell volume goes down, the formation energy of In^{3+}/Mo^{6+} dopants in *t*-$BiVO_4$ decreases, and eventually gets smaller than that in *m*-$BiVO_4$ when the cell volume is smaller than ~1320 $Å^3$. In addition, the total energy of doped *t*-$BiVO_4$ gets smaller than that of undoped *t*-$BiVO_4$ when the cell volume is smaller than 1254 $Å^3$. This suggests that as the cell volume becomes smaller and smaller, the formation of In^{3+}/Mo^{6+} dopants

is more facilitated within t-$BiVO_4$ rather than within m-$BiVO_4$, and ultimately the compressed tetragonal crystal structure can be more stabilized with doping than without doping. This doping-induced phase change and the subsequent rise of the CBE represent a novel concept to create a visible light active OWS photocatalyst by the band structure engineering.

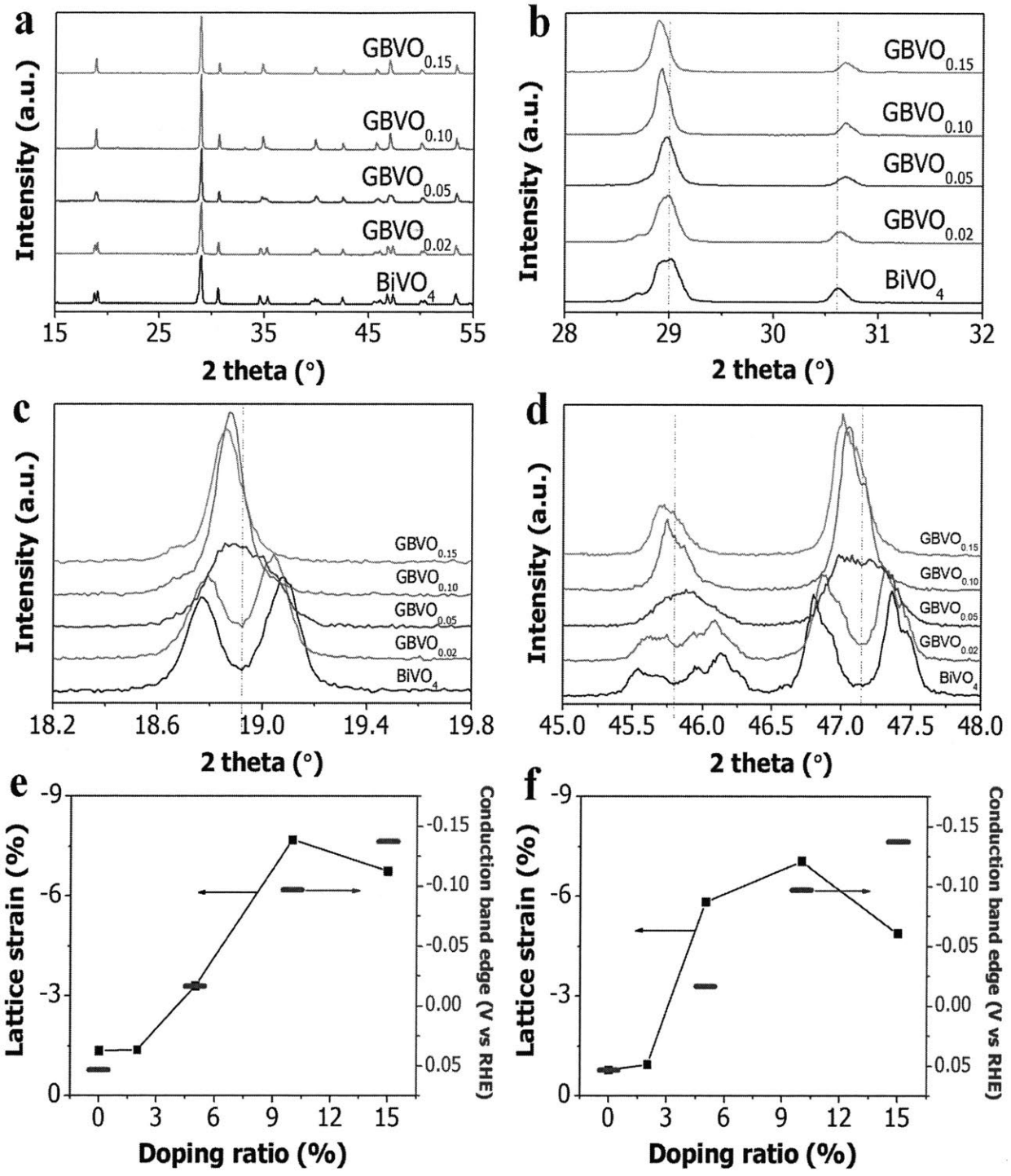

Figure 4-S1. Shifts and evolution of XRD peaks, and relationship between lattice strain and conduction band edge: a) Full range XRD patterns, b) Main peaks' shift, and c) & d) Mergence

of main peaks of pristine $BiVO_4$ and all $GBVO_x$ samples. e) Compressive (minus) lattice strain evaluated by volumetric strain method and conduction band edge position as a function of doping concentration. f) Compressive (minus) lattice strain evaluated by Williamson-Hall method and conduction band edge position as a function of doping concentration.

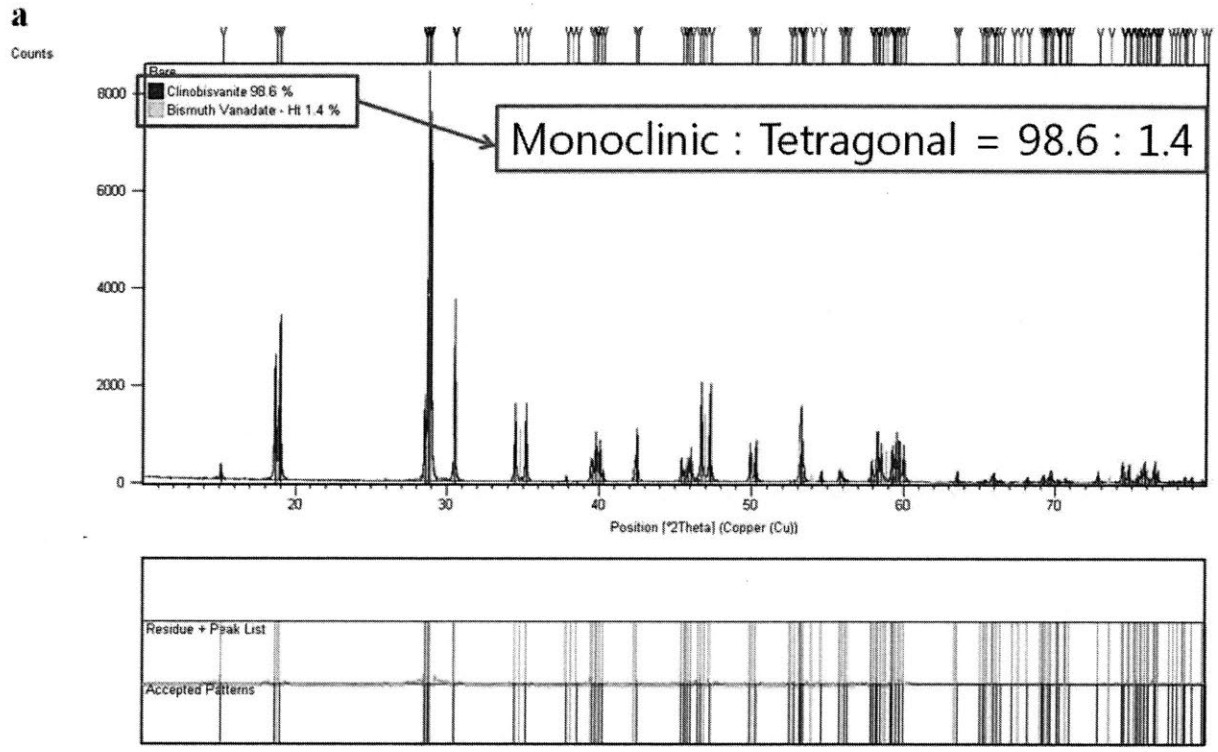
a
Counts
Clinobisvanite 98.6 %
Bismuth Vanadate - Ht 1.4 %
Monoclinic : Tetragonal = 98.6 : 1.4
8000
6000
4000
2000
0
20
30
40
50
60
70
Position [°2Theta] (Copper (Cu))
Residue + Peak List
Accepted Patterns

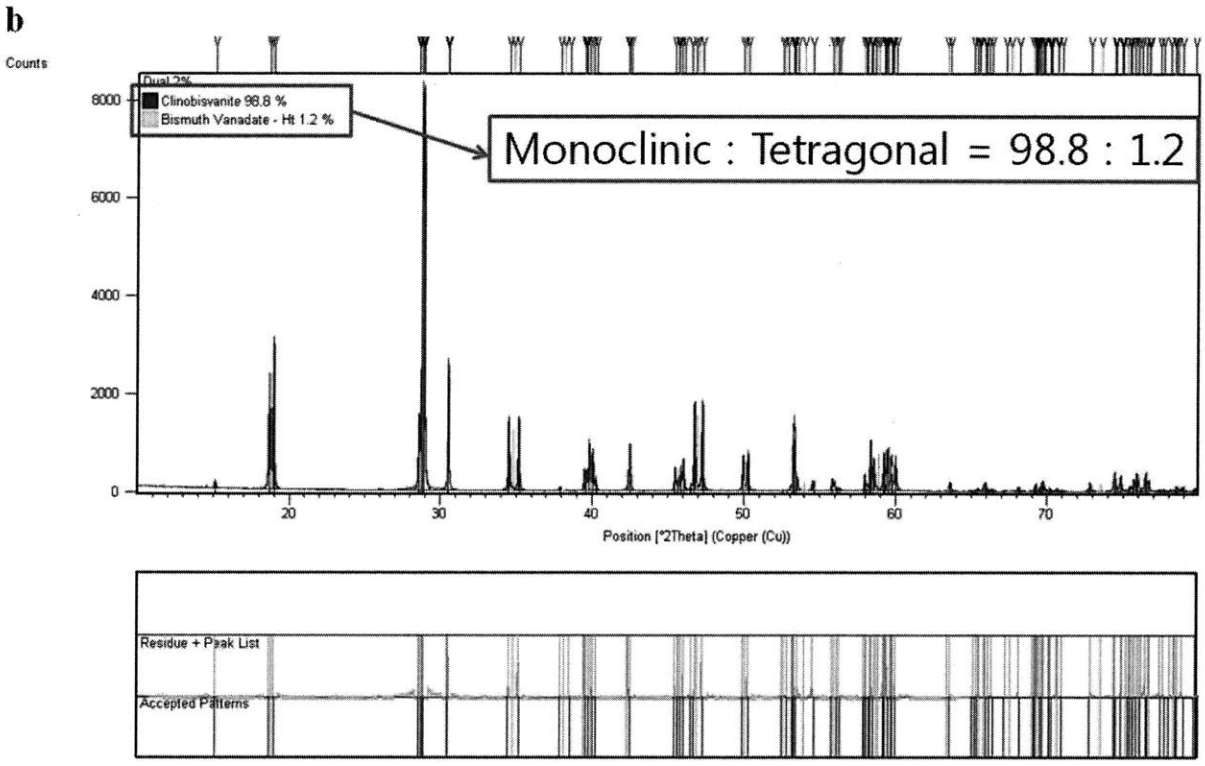
b
Counts
Clinobisvanite 98.8 %
Bismuth Vanadate - Ht 1.2 %
Monoclinic : Tetragonal = 98.8 : 1.2
8000
6000
4000
2000
0
20
30
40
50
60
70
Position [°2Theta] (Copper (Cu))
Residue + Peak List
Accepted Patterns

c

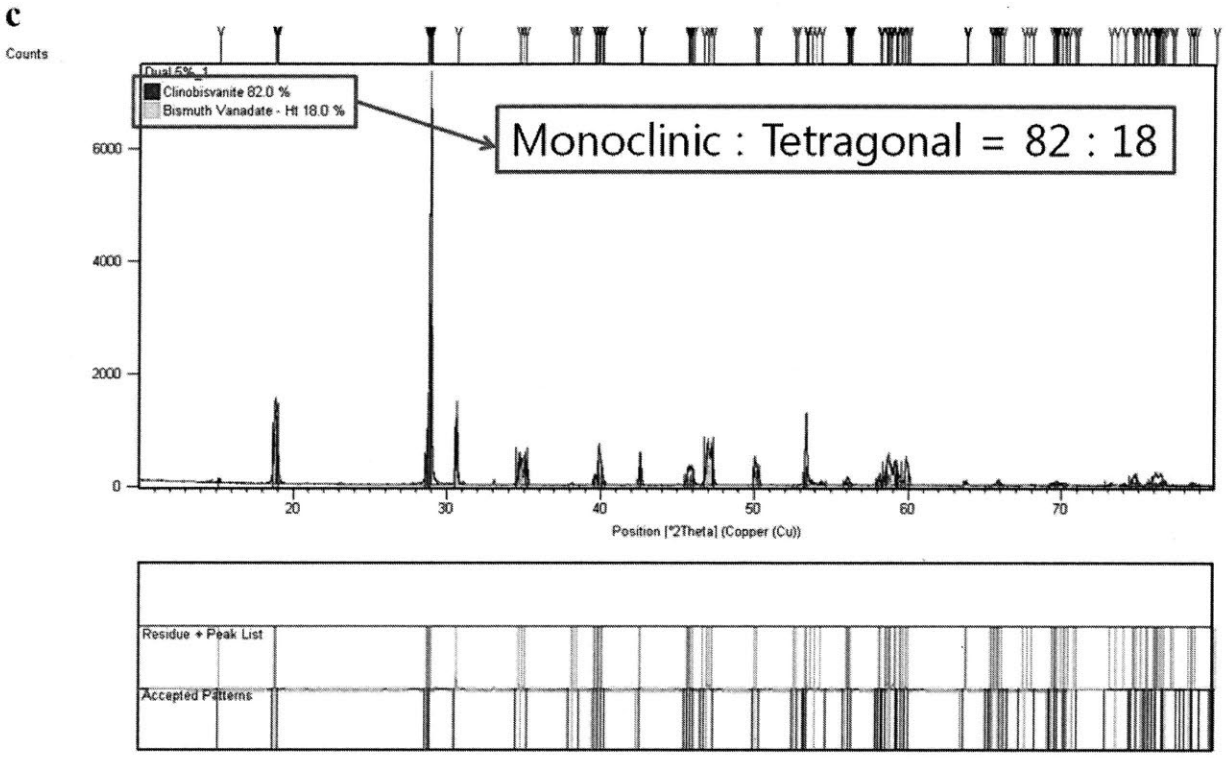
Counts
Clinobisvanite 82.0 %
Bismuth Vanadate - Ht 18.0 %
Monoclinic : Tetragonal = 82 : 18
6000
4000
2000
0
20
30
40
50
60
70
Position [°2Theta] (Copper (Cu))
Residue + Peak List
Accepted Patterns

d

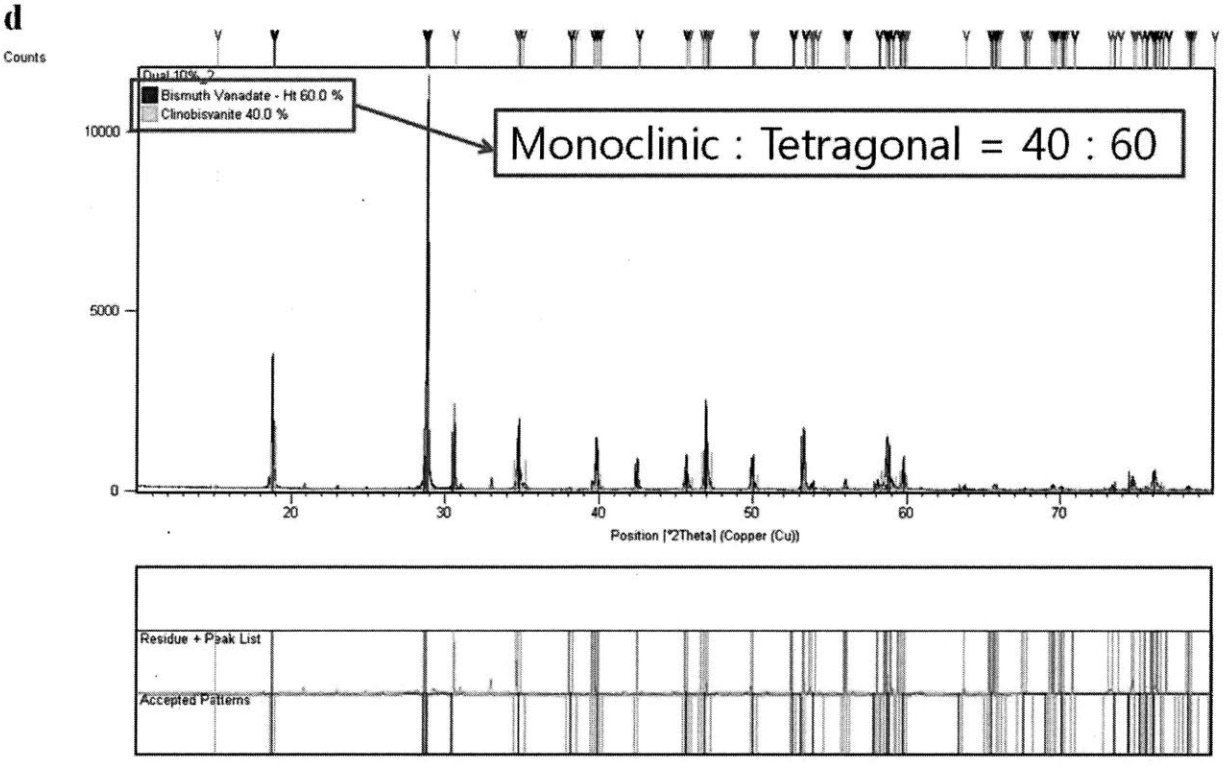
Counts
Bismuth Vanadate - Ht 60.0 %
Clinobisvanite 40.0 %
Monoclinic : Tetragonal = 40 : 60
10000
5000
0
20
30
40
50
60
70
Position [°2Theta] (Copper (Cu))
Residue + Peak List
Accepted Patterns

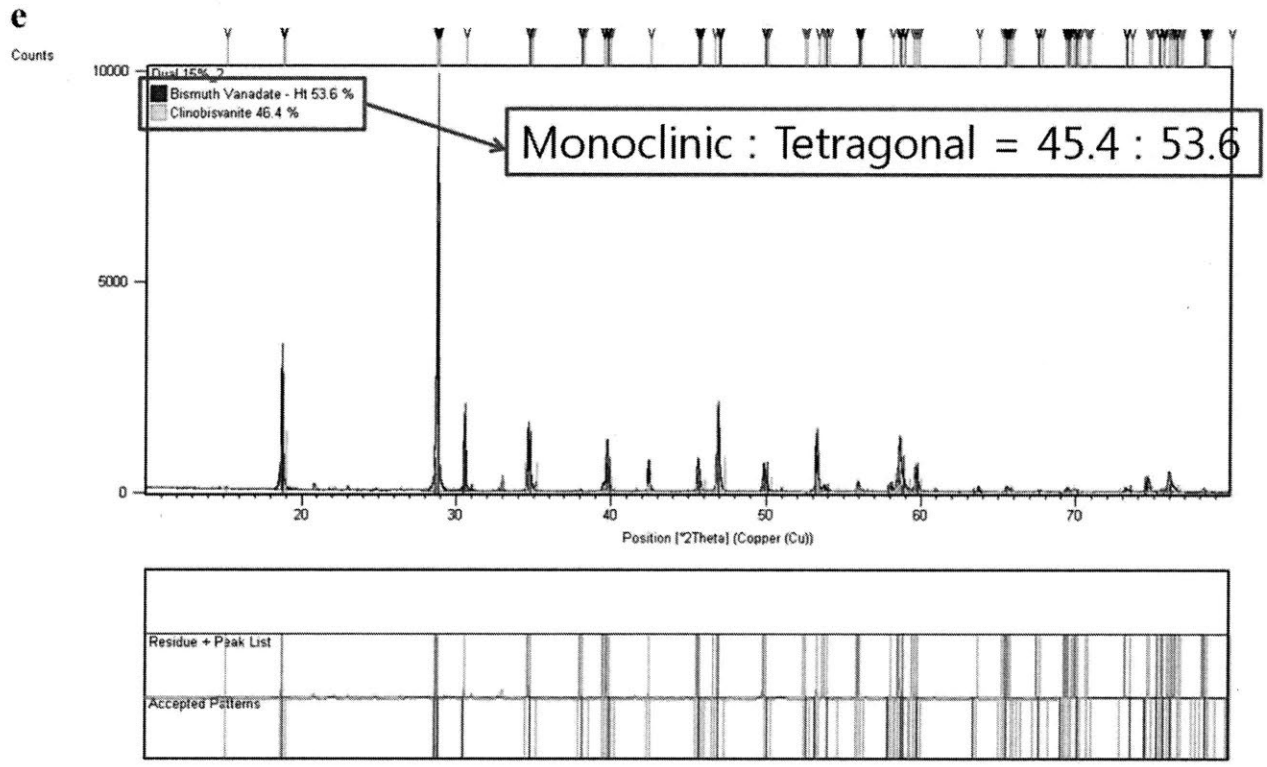

Figure 4-S2. Monoclinic to tetragonal ratios in pristine $BiVO_4$ and all $GBVO_x$ samples. Blue colored peaks: Scheelite-monoclinic-$BiVO_4$ reference peaks. Green colored peaks: Tetragonal-$BiVO_4$ reference peaks. Orange colored peaks: Prepared-samples' peaks. a) Pristine $BiVO_4$, b) $GBVO_{0.02}$, c) $GBVO_{0.05}$, d) $GBVO_{0.10}$, e) $GBVO_{0.15}$.

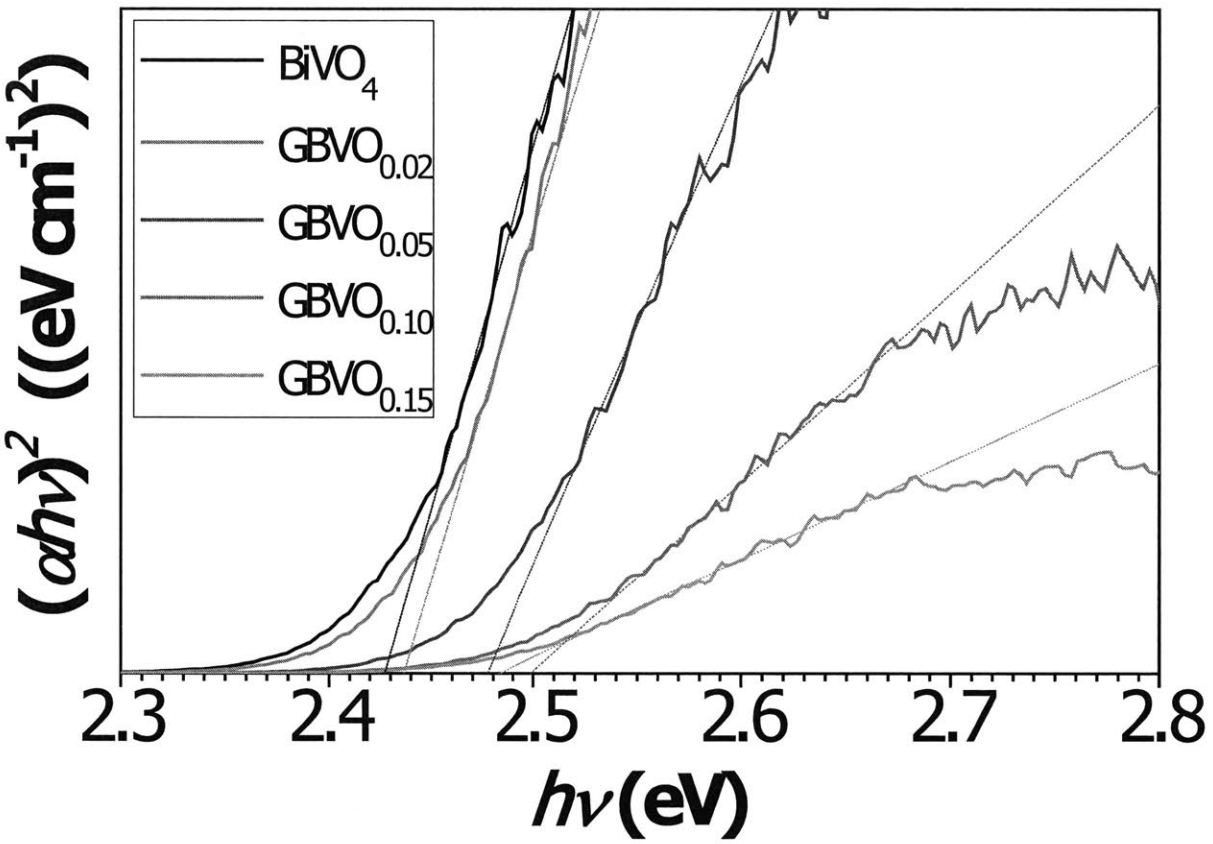

Figure 4-S3. Tauc plot of pristine $BiVO_4$ and all $GBVO_x$ samples.

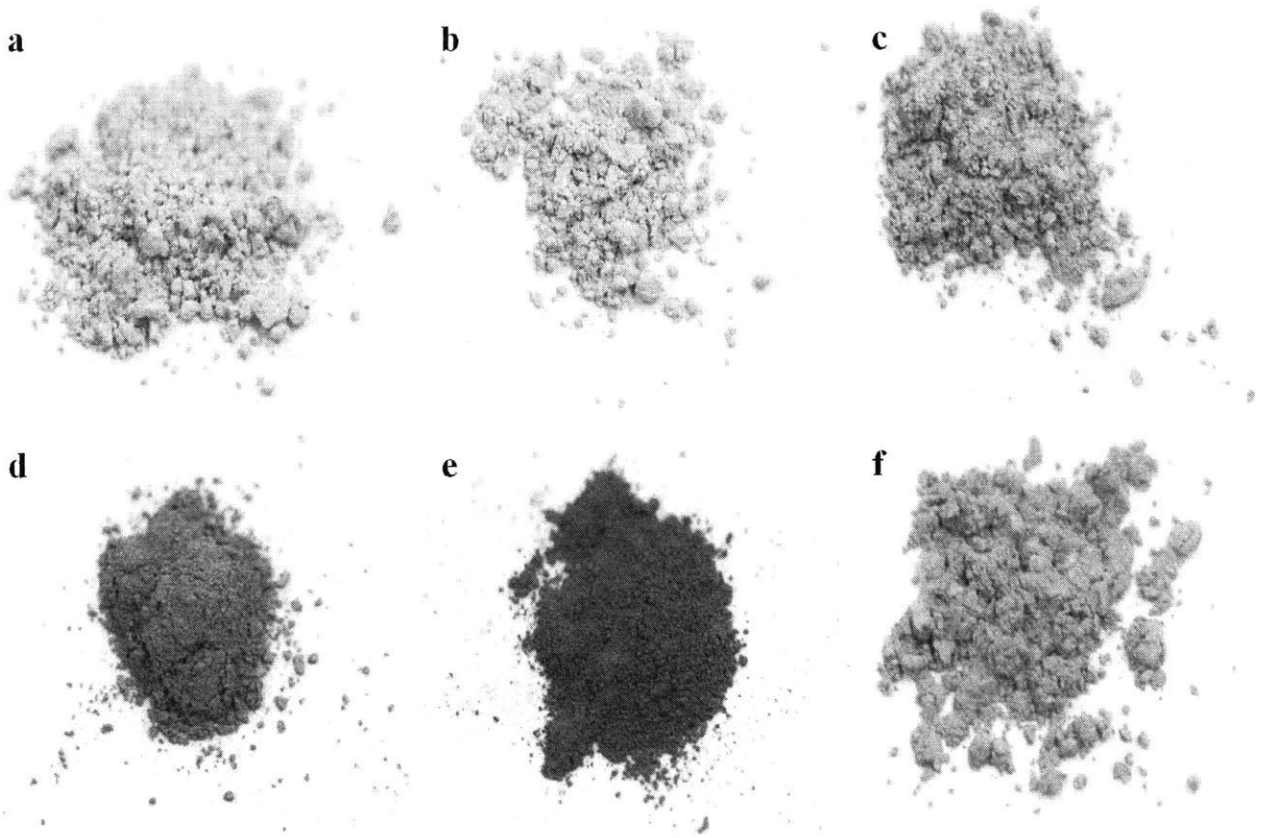

Figure 4-S4. Powder sample images of pristine $BiVO_4$ and all $GBVO_x$ samples. a) Pristine $BiVO_4$, b) $GBVO_{0.02}$, c) $GBVO_{0.05}$, d) $GBVO_{0.10}$, e) $GBVO_{0.15}$, f) $BiV_{0.98}Mo_{0.02}O_4$.

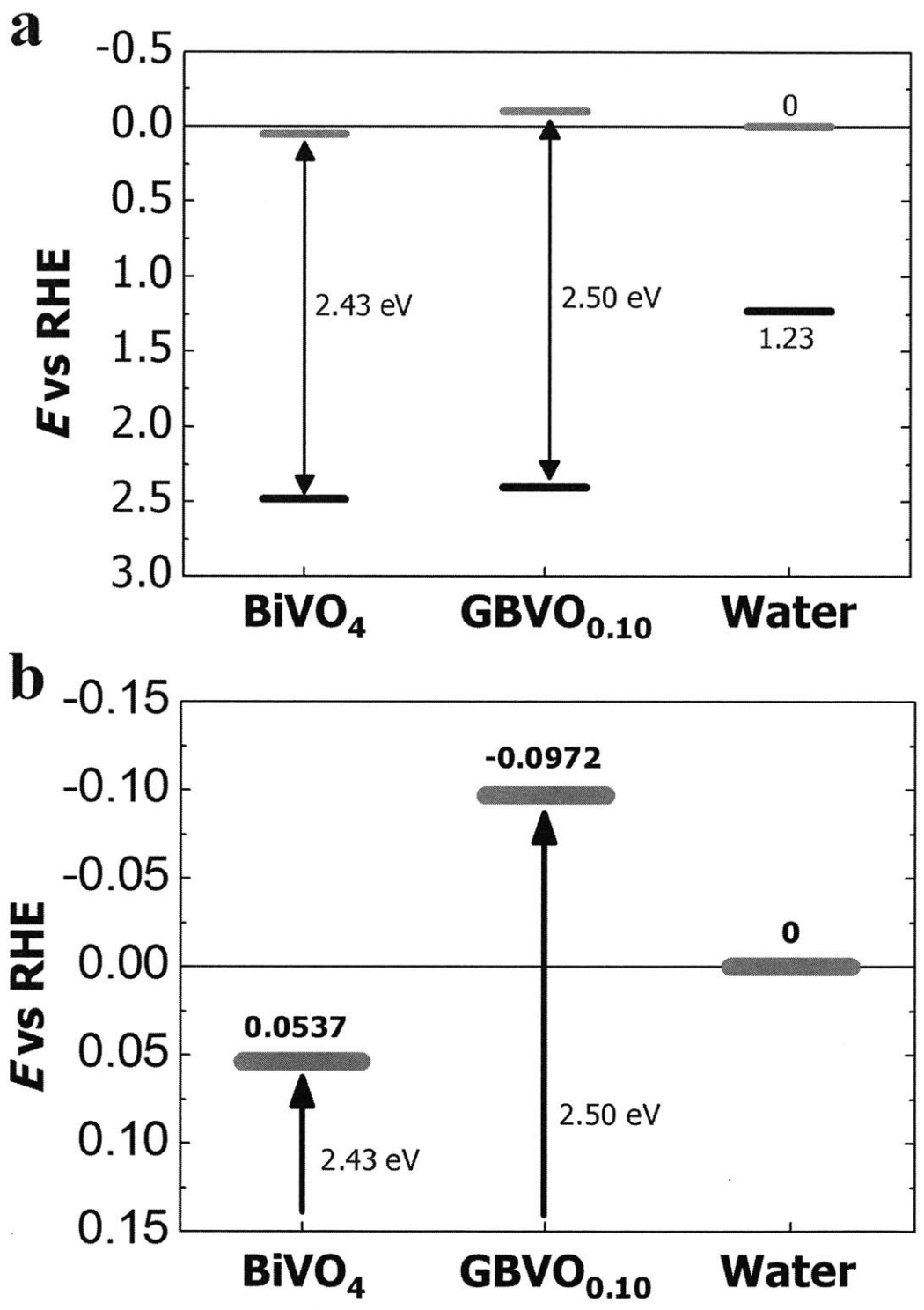

Figure 4-S5. Band structures determined by Tauc and Mott-Schottky plots for Pristine $BiVO_4$ and $GBVO_{0.10}$. a) Overall band structure, b) Blow-up near conduction band edge.

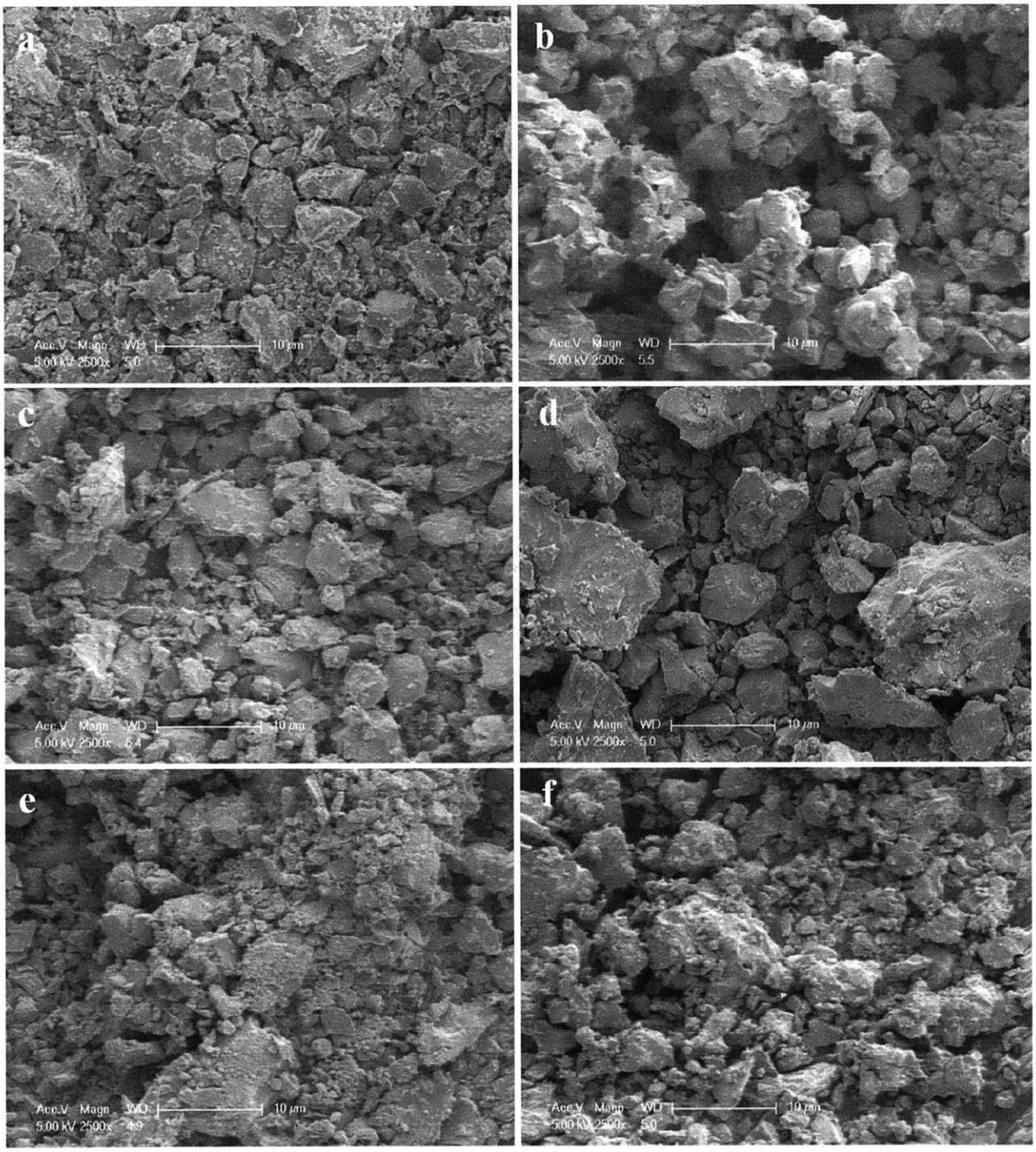

Figure 4-S6. FESEM images of pristine $BiVO_4$ and all $GBVO_x$ samples. a) Pristine $BiVO_4$, b) $GBVO_{0.02}$, c) $GBVO_{0.05}$, d) $GBVO_{0.10}$, e) $GBVO_{0.15}$, f) $BiV_{0.98}Mo_{0.02}O_4$.

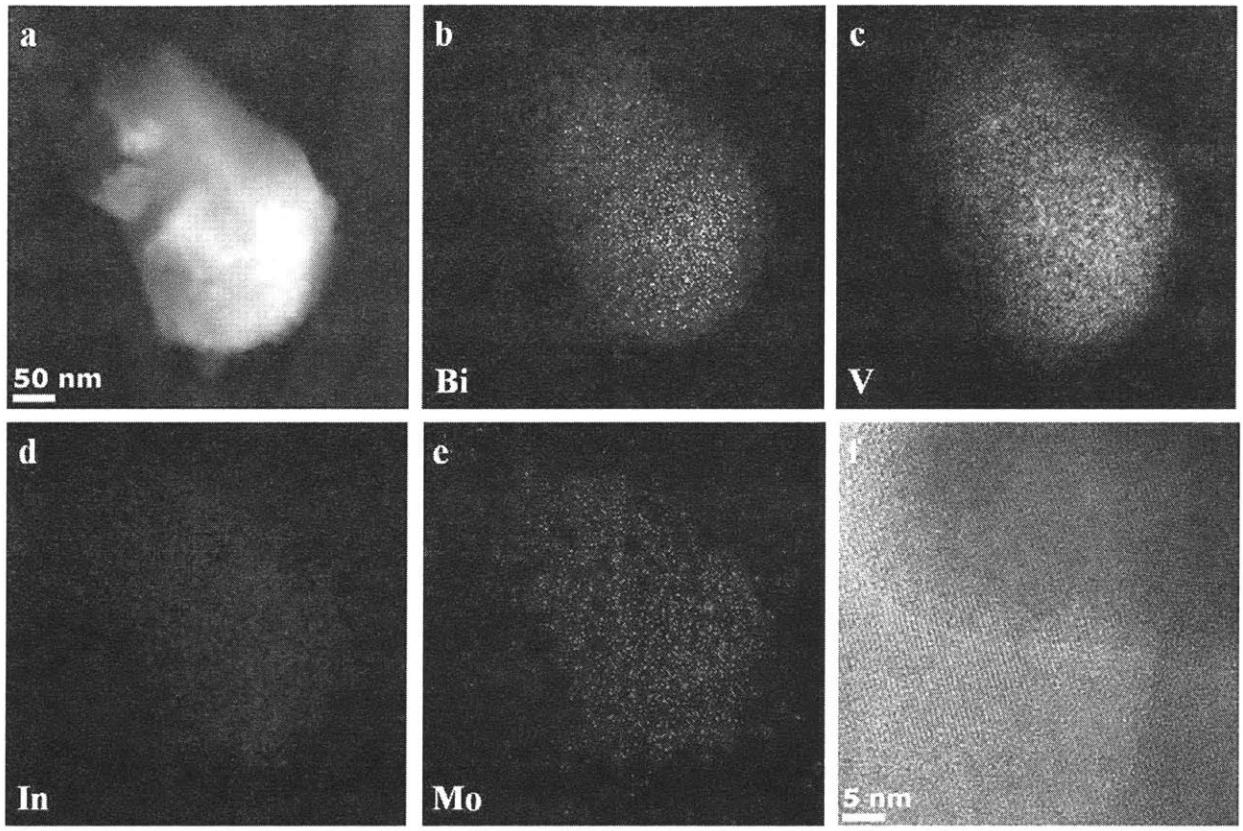

Figure 4-S7. HR-TEM EDS analysis of $GBVO_{0.02}$. a) High-angle annular dark-field (HAADF) image of $GBVO_{0.02}$ particle, b) Bi, c) V, d) In, and e) Mo detectred by elemental mapping. f) HR-TEM image of $GBVO_{0.02}$ particle.

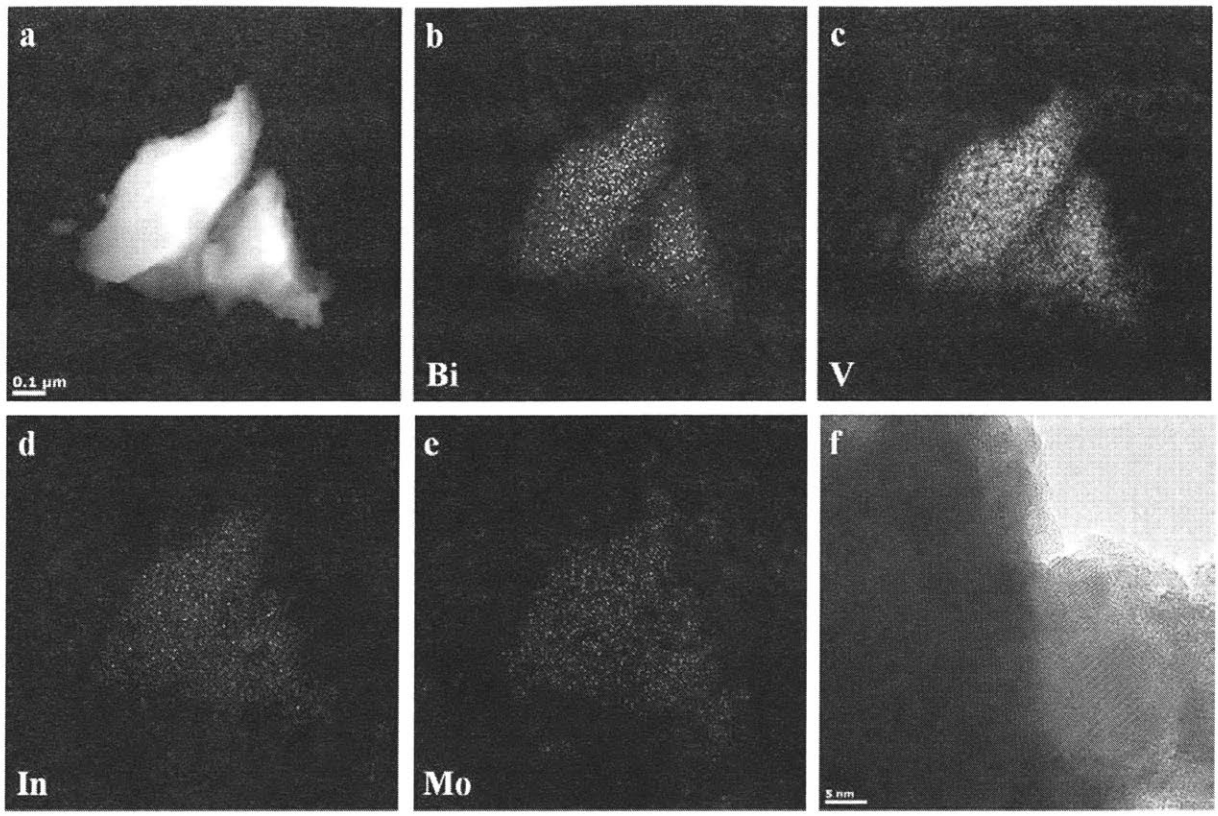

Figure 4-S8. HR-TEM EDS analysis of $GBVO_{0.05}$. a) High-angle annular dark-field (HAADF) image of $GBVO_{0.05}$ particle. b) Bi, c) V, d) In, and e) Mo detectred by elemental mapping. f) HR-TEM image of $GBVO_{0.05}$ particle.

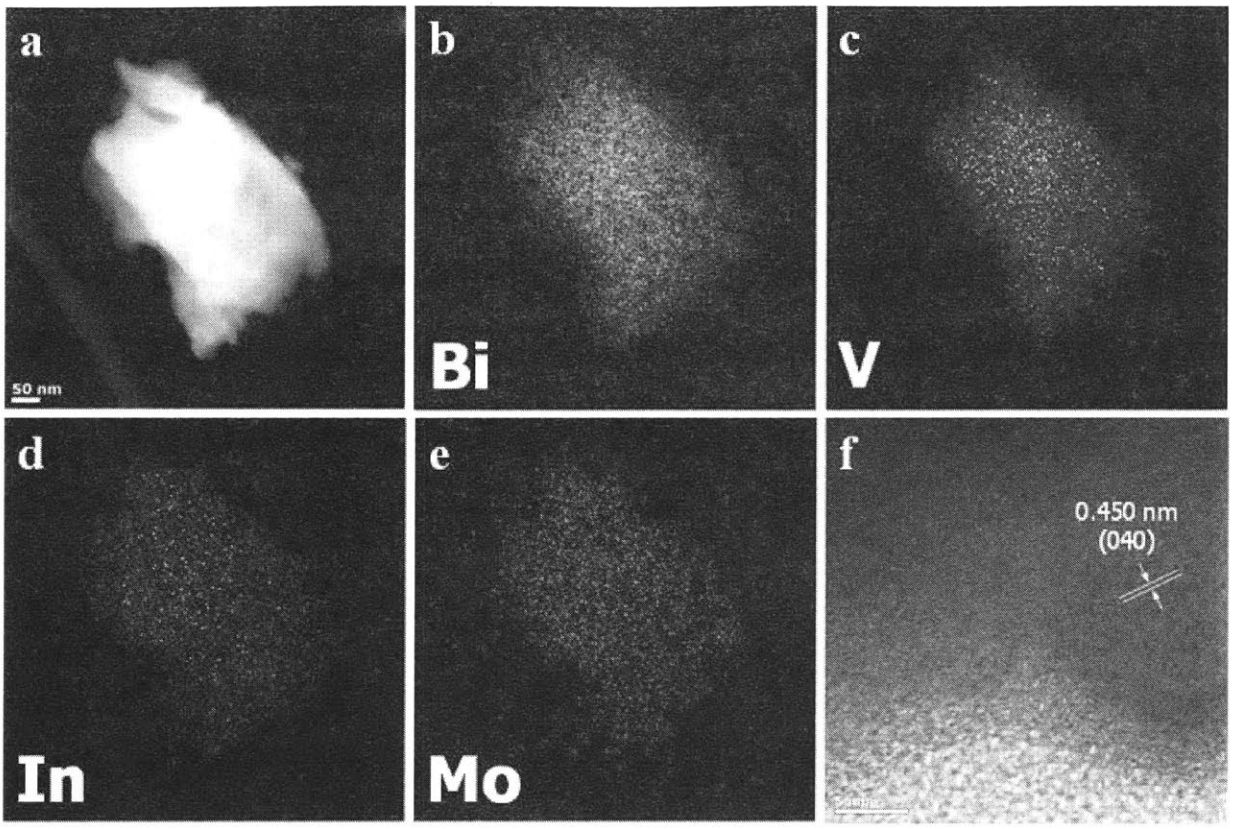

Figure 4-S9. HR-TEM EDS analysis of $GBVO_{0.10}$. a) High-angle annular dark-field (HAADF) image of $GBVO_{0.10}$ particle. b) Bi, c) V, d) In, and e) Mo detected by elemental mapping. f) HR-TEM image of $GBVO_{0.10}$ particle.

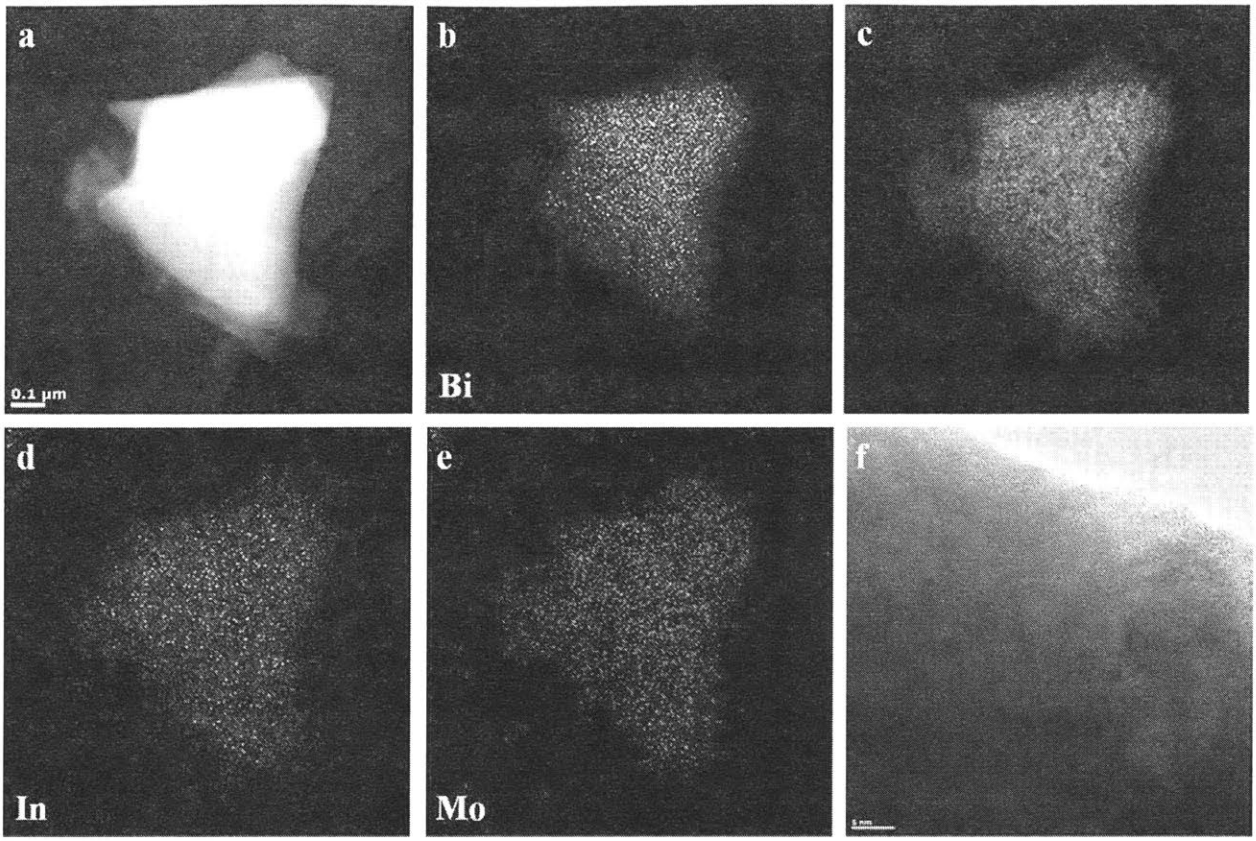

Figure 4-S10. HR-TEM EDS analysis of $GBVO_{0.15}$. a) High-angle annular dark-field (HAADF) image of $GBVO_{0.15}$ particle. b) Bi, c) V, d) In, and e) Mo detectred by elemental mapping. f) HR-TEM image of $GBVO_{0.15}$ particle.

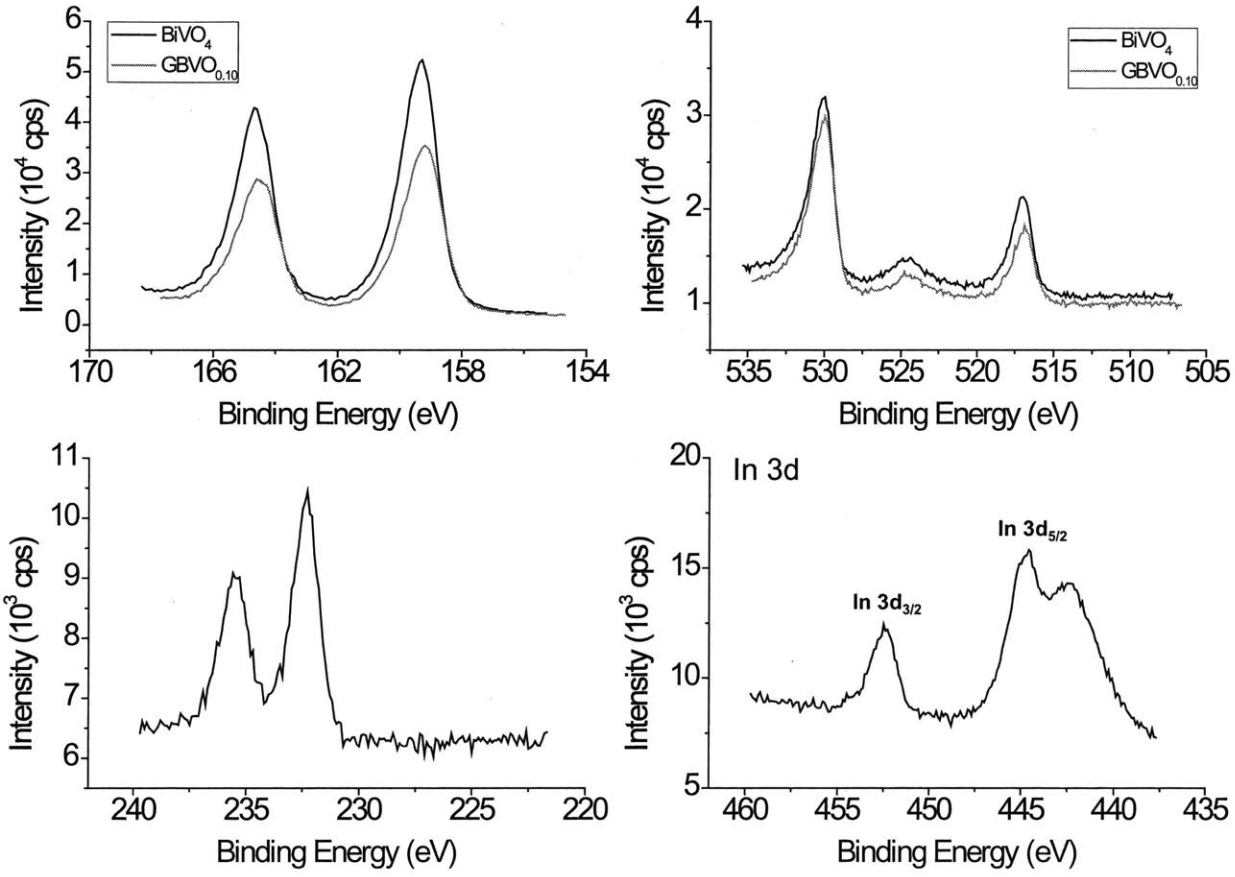

Figure 4-S11. XPS of $GBVO_{0.10}$. The binding energies indicate that the involved elements are all in their stable oxidation states of Bi^{3+}, V^{5+}, Mo^{6+}, and In^{3+}.

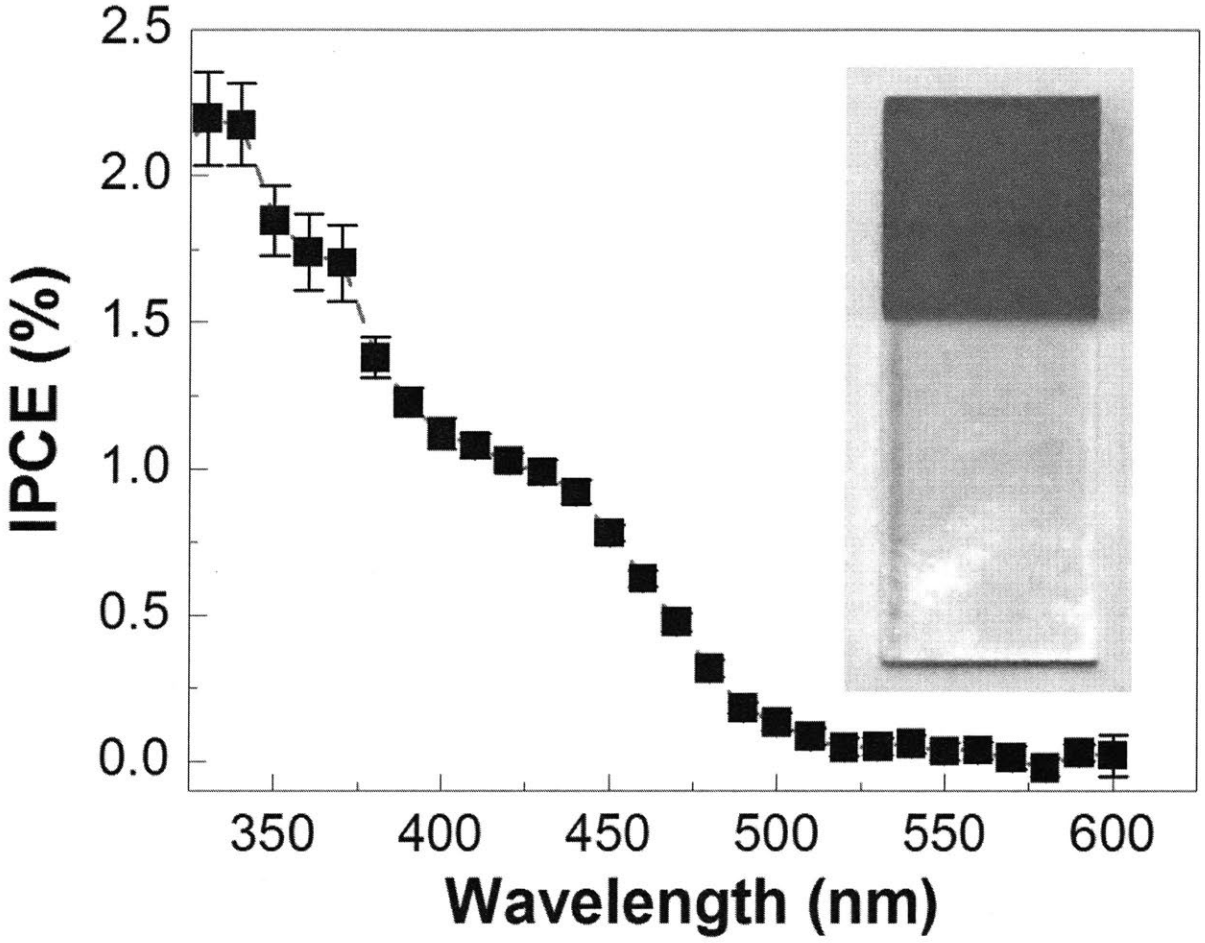

Figure 4-S12. IPCE of $GBVO_{0.10}$ film. IPCE of $GBVO_{0.10}$ photoelectrode was measured at 0.7 V (vs. Ag/AgCl) in 0.5M Na_2SO_4 solution. The backside of $GBVO_{0.10}$ photoelectrode was illuminated with QEX7 (PV Measurements, Inc.) calibrated by a NIST-certified Si photodidode.

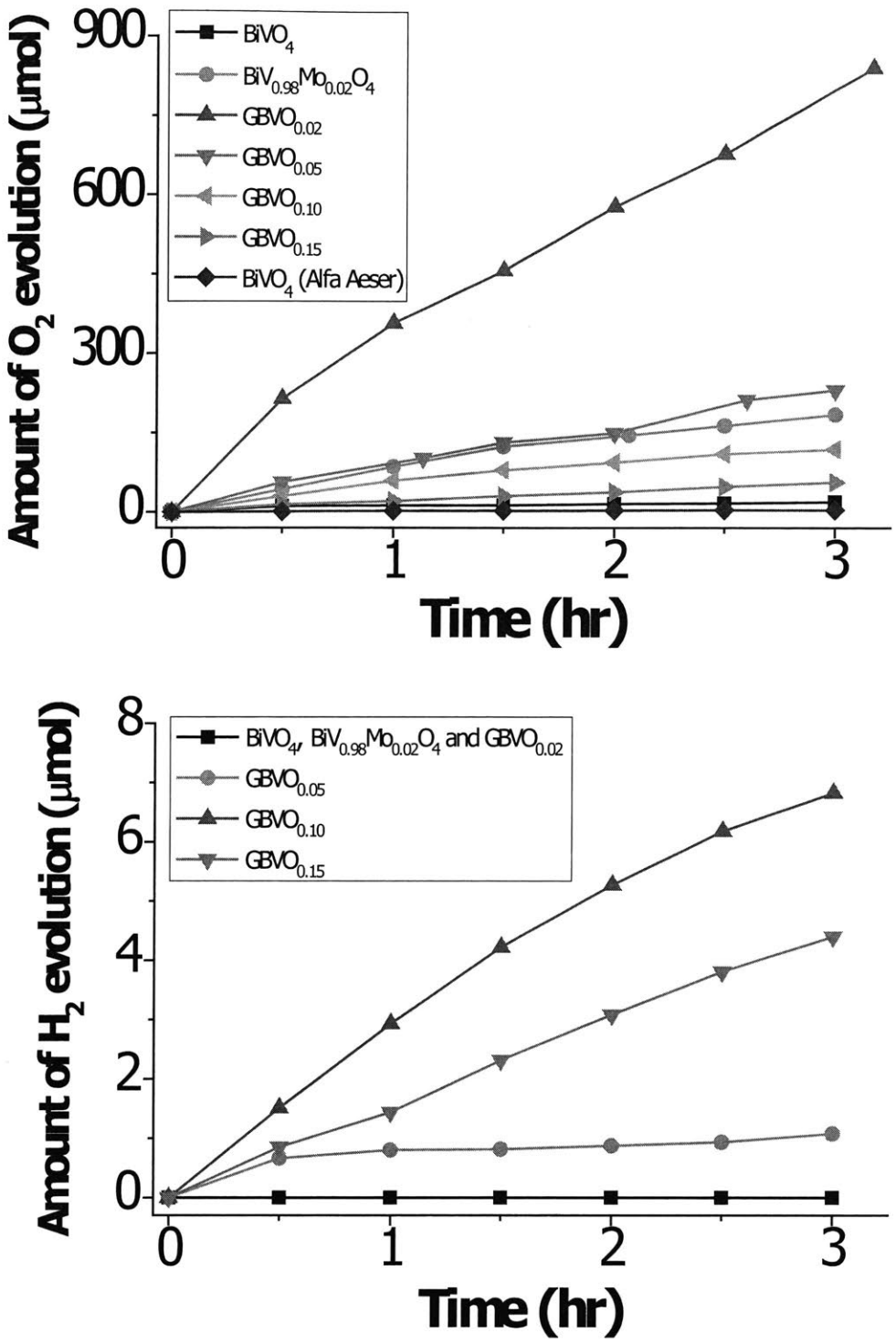

Figure 4-S13. Photocatalytic activities of $GBVO_x$ with sacrificial reagents. a) Photocatalytic water oxidation by pristine $BiVO_4$, $BiV_{0.98}Mo_{0.02}O_4$ and all $GBVO_x$ samples under the visible-

light ($\lambda \geq 420$ nm) irradiation. 0.1 g of photocatalyst powder was dispersed in 100 ml of aqueous $AgNO_3$ solution (50 mM) as an electron scavenger. b) Photocatalytic water reduction by pristine $BiVO_4$, $BiV_{0.98}Mo_{0.02}O_4$ and all $GBVO_x$ samples under the visible-light ($\lambda \geq 420$ nm) irradiation. 0.1 g of photocatalyst powder was dispersed in 80 ml of distilled water and 20 ml of CH_3OH as a hole scavenger.

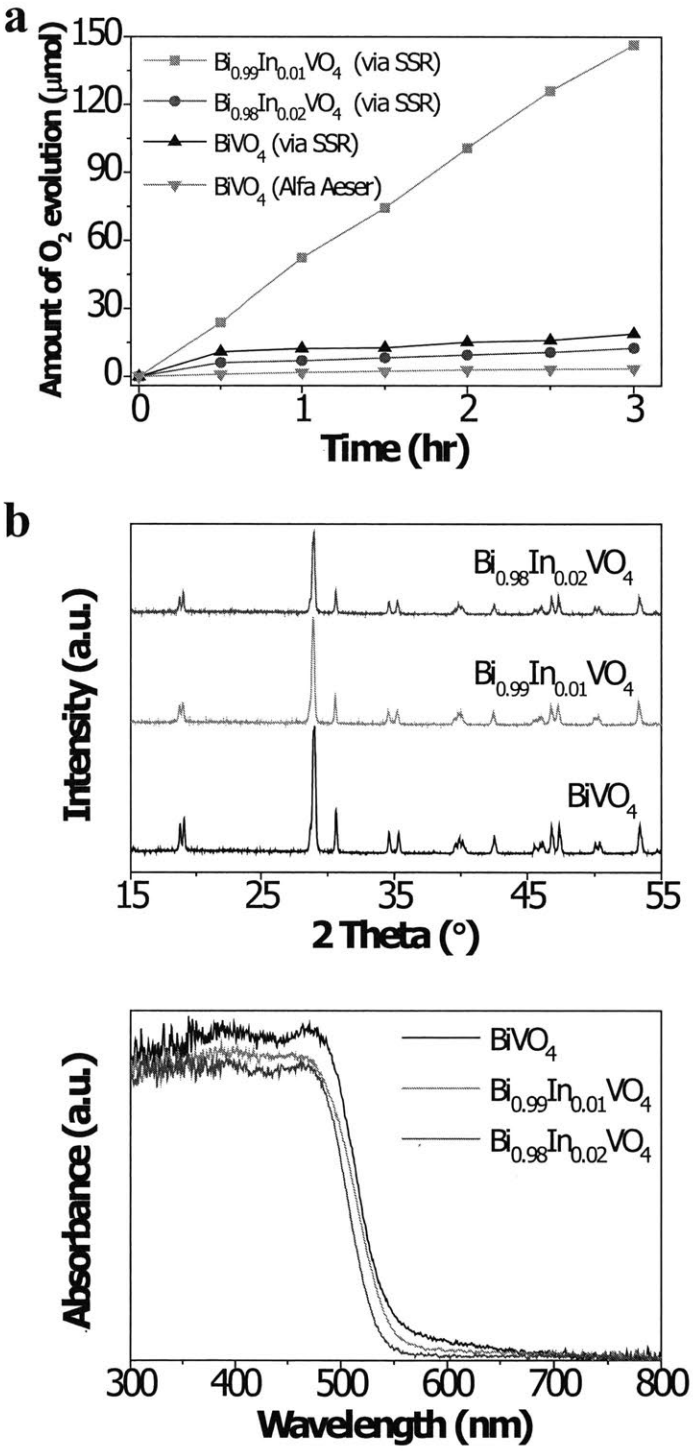

Figure 4-S14. Single In-doped $BiVO_4$, $Bi_{1-x}In_xVO_4$. a) Photocatalytic water oxidation under the visible-light ($\lambda \geq 420$ nm) irradiation. 0.1 g of photocatalyst powder was dispersed in 100 ml of

aqueous $AgNO_3$ solution (50 mM) as an electron scavenger. b) XRD patterns, c) UV-Vis absorption spectra.

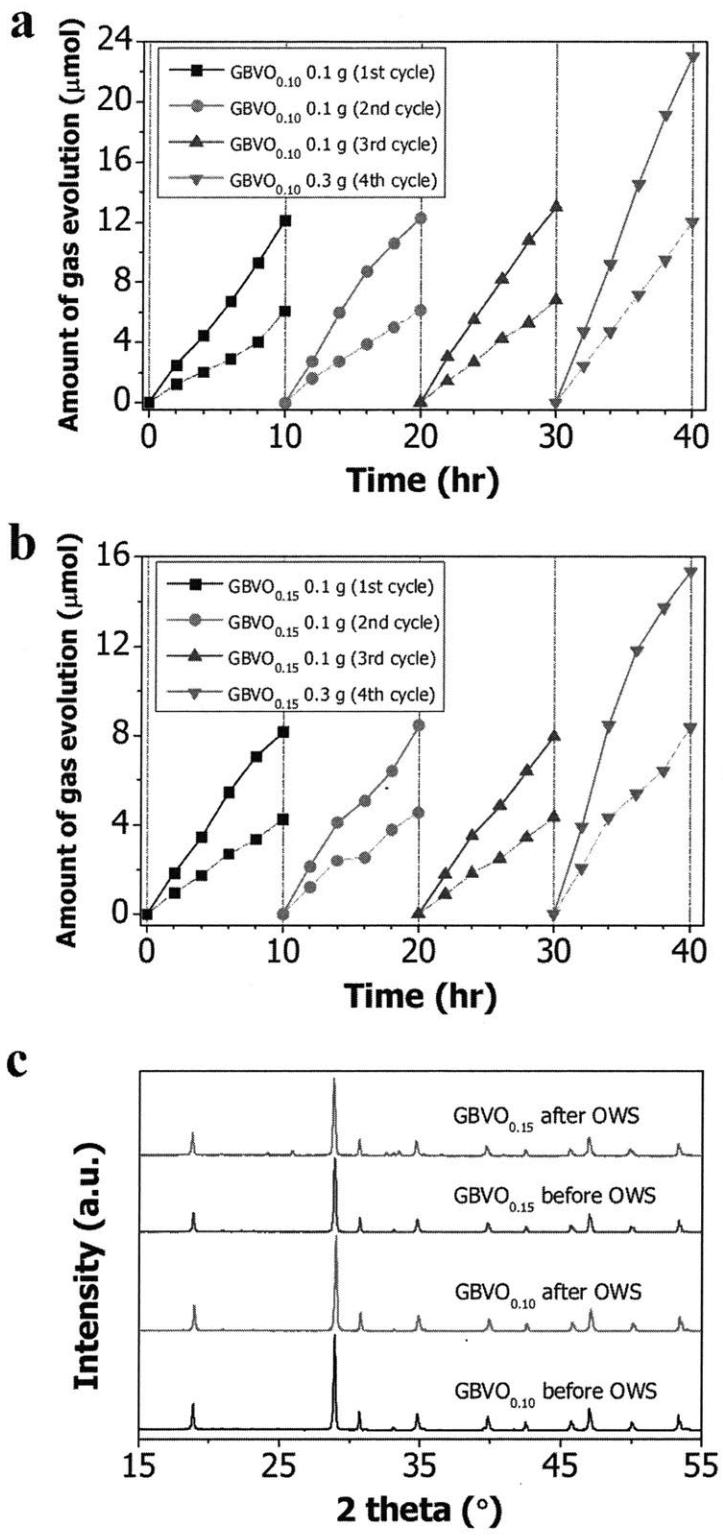

Figure 4-S15. 40-hour overall water splitting by unmodified $GBVO_{0.10 \text{ and } 0.15}$ under the visible-light ($\lambda \geq 420$ nm) irradiation in order to test photochemical stability. a) Overall water splitting

by unmodified $GBVO_{0.10}$, b) Overall water splitting by unmodified $GBVO_{0.15}$. Both overall water splitting reactions used N_2 purged suspension of 0.1 or 0.3 g photocatalyst powder in 100 ml distilled water. Solid and dashed lines indicate evolved H_2 and O_2, respectively. c) XRD patterns of $GBVO_{0.10 \text{ and } 0.15}$ before and after 40-hour overall water splitting reaction.

Sample	Element	Wt %	Atomic %	Composition
2% In, Mo doped $BiVO_4$	In	0.82	0.024	$\mathbf{Bi_{0.998}In_{0.024}V_{0.980}Mo_{0.020}O_4}$
	Mo	0.58	0.020	
5% In, Mo doped $BiVO_4$	In	1.84	0.055	$\mathbf{Bi_{0.945}In_{0.055}V_{0.949}Mo_{0.051}O_4}$
	Mo	1.42	0.051	
10% In, Mo doped $BiVO_4$	In	3.63	0.114	$\mathbf{Bi_{0.886}In_{0.114}V_{0.889}Mo_{0.111}O_4}$
	Mo	2.95	0.111	
15% In, Mo doped $BiVO_4$	In	5.52	0.181	$\mathbf{Bi_{0.819}In_{0.181}V_{0.823}Mo_{0.177}O_4}$
	Mo	4.51	0.177	

Table 4-2. ICP results of the four $GBVO_x$ samples.

Electrode material	N_D /cm^3
$BiVO_4$	1.285E+21
$GBVO_{0.05}$	1.810E+20
$GBVO_{0.10}$	9.155E+19
$GBVO_{0.15}$	7.080E+19

Table 4-3. The estimated carrier density (N_D) of $BiVO_4$ and $GBVO_{0.05, 0.10 \text{ and } 0.15}$ electrodes. The N_D values of BiVO4 and $GBVO_{0.05, 0.10 \text{ and } 0.15}$ electrodes are estimated by using previously reported method (20).

4.5. Conclusions

In summary, through In^{3+}/Mo^{6+} dual doping into the host lattice of monoclinic $BiVO_4$, we have created a novel visible light-responsive OWS photocatalyst. The resulting greenish $BiVO_4$ splits water into H_2 and O_2 via one-step photoexcitation because it has an up-shifted conduction band edge transforming (only) O_2-evolving yellow $BiVO_4$ into (both) H_2/O_2-evolving greenish $BiVO_4$, a one-photon OWS photocatalyst. The DFT calculation indicates that In^{3+}/Mo^{6+} dual doping triggers partial phase transformation from pure *m*-$BiVO_4$ to a mixture of *m*-$BiVO_4$ and *t*-$BiVO_4$, which sequentially leads to unit-cell volume growth, compressive lattice-strain increase, conduction-band edge uplift, and band-gap widening. This domino effect is also corroborated experimentally. The greenish $BiVO_4$ is an active and stable one-photon OWS photocatalyst made of earth-abundant elements and works in pure water without any additives.

4.6. References

1. Jo WJ, *et al.* (2012) Phosphate doping into monoclinic $BiVO_4$ for enhanced photoelectrochemical water oxidation activity. *Angew Chem Int Ed Engl* 51(13): 3147-3151.
2. Grätzel M (2005) Solar energy conversion by dye-sensitized photovoltaic cells. *Inorg Chem* 44(20): 6841-6851.
3. Bard AJ, Fox MA (1995) Artificial photosynthesis: Solar splitting of water to hydrogen and oxygen. *Acc Chem Res* 28(3): 141-145.
4. Maeda K, *et al.* (2006) Photocatalyst releasing hydrogen from water. *Nature* 440(7082): 295.
5. Maeda K, *et al.* (2005) GaN:ZnO solid solution as a photocatalyst for visible-light-driven overall water splitting. *J Am Chem Soc* 127(23): 8286-8287.
6. Chen X, Liu L, Yu PY, Mao SS (2011) Increasing solar absorption for photocatalysis with black hydrogenated titanium dioxide nanocrystals. *Science* 331(6018): 746-750.
7. Liu H, *et al.* (2011) Novel photocatalyst of V-based solid solutions for overall water splitting. *J Mater Chem* 21(41): 16535-16543.
8. Wang D, *et al.* (2012) Photocatalytic water oxidation on $BiVO_4$ with the electrocatalyst as an oxidation cocatalyst: Essential relations between electrocatalyst and photocatalyst. *J Phys Chem C Nanomater Interfaces* 116(8): 5082-5089.
9. Kudo A, Omori K, Kato H. (1999) A novel aqueous process for preparation of crystal form-controlled and highly crystalline $BiVO_4$ powder from layered vanadates at room temperature and its

photocatalytic and photophysical properties. *J Am Chem Soc* 121(49): 11459-11467.

10. Tokunaga S, Kato H, Kudo A (2001) Selective preparation of monoclinic and tetragonal $BiVO_4$ with scheelite structure and their photocatalytic properties. *Chem Mater* 13(12): 4624-4628.

11. Hong SJ, Lee S, Jang JS, Lee JS (2011) Heterojuction $BiVO_4/WO_3$ electrodes for enhanced photoactivity of water oxidation. *Energy Environ Sci* 4(5): 1781-1787.

12. Yao W, Iwai H, Ye J (2008) Effects of molybdenum substitution on the photocatalytic behavior of $BiVO_4$. *Dalton Trans* (11): 1426-1430.

13. Long M, Cai W, Kisch H (2008) Visible light induced photoelectrochemical properties of n-$BiVO_4$ and n-$BiVO_4$/p-$Co3O_4$. *J Phys Chem C Nanomater Interfaces* 112(2): 548-554.

14. Jiang HQ, Endo H, Natori H, Nagai M, Kobayashi K (2009) Fabrication and efficient photocatalytic degradation of methylene blue over CuO/$BiVO_4$ composite under visible-light irradiation. *Mater Res Bull* 44(3): 700-706.

15. Kim TW, Choi K-S (2014) Nanoporous $BiVO_4$ photoanodes with dual-layer oxygen evolution catalysts for solar water splitting. *Science* 343(6174): 990-994.

16. Kohtani S, Tomohiro M, Tokumura K, Nakagaki R (2005) Photooxidation reactions of polycyclic aromatic hydrocarbons over pure and Ag-loaded $BiVO_4$ photocatalysts. *Appl Catal B* 58(3-4): 265-272.

17. Kohtani S, *et al.* (2005) Adsorptive and photocatalytic properties of Ag-loaded $BiVO_4$ on the degradation of 4-*n*-alkylphenols under visible light irradiation. *Catal Commun* 6(3): 185-189.

18. Yao W, Ye J (2006) Photophysical and photocatalytic properties of $Ca_{1-x}Bi_xV_xMo_{1-x}O_4$ solid solutions. *J Phys Chem B* 110(23): 11188-11195.

19. Luo W, *et al.* (2011) Solar hydrogen generation from seawater with a modified $BiVO_4$ photoanode. *Energy Environ Sci* 4(10): 4046-4051.

20. Parmar KPS, *et al.* (2012) Photocatalytic and photoelectrochemical water oxidation over metal-doped monoclinic $BiVO_4$ photoanode. *ChemSusChem* 5(10): 1926-1934.

21. Asahi R, Morikawa T, Ohwaki T, Aoki K, Taga Y (2001) Visible-light photocatalysis in nitrogen-doped titanium oxides. *Science* 293(5528): 269-271.

22. Park HS, *et al.* (2011) Factors in the metal doping of $BiVO_4$ for improved photoelectrocatalytic activity as studied by scanning electrochemical microscopy and first-principles density-functional calculation. *J Phys Chem C Nanomater Interfaces* 115(36): 17870-17879.

23. Wang Q, Liu H, Yuan J, Shangguan W (2009) Synthesis and characterization of visible-light-responding $Bi_{0.5}La_{0.5}VO_4$ solid solution for photocatalytic water splitting. *Chin J Catal* 30(6): 565-569.

24. Sasaki Y, Nemoto H, Saito K, Kudo A (2009) Solar water splitting using powdered photocatalysts driven by Z-schematic inter-particle electron transfer without an electron mediator. *J Phys Chem C Nanomater Interfaces* 113(40): 17536-17542.

25. Seabold JA, Zhu K, Neale NR (2014) Efficient solar photoelectrolysis by nanoporous Mo:BiVO4 through controlled electron transport. *Phys Chem Chem Phys* 16(3): 1121–1131.

26. Park Y, McDonald KJ, Choi K-S (2013) Progress in bismuth vanadate photoanodes for use in solar water oxidation. *Chem Soc Rev* 42: 2321-2337

27. Zhong DK, Choi S, Gamelin DR (2011) Near-complete suppression of surface recombination in solar photoelectrolysis by "co-Pi" catalyst-modified W:BiVO4. *J Am Chem Soc* 133(45): 18370–18377.

28. Abdi FF, Krol RVD (2012) Nature and light dependence of bulk recombination in Co-Pi-catalyzed $BiVO_4$ photoanodes. *J Phys Chem C* 116(17): 9398–9404.

29. Abdi FF, Savenije TJ, May MM, Dam B, Krol RVD (2013) The Origin of Slow Carrier Transport in $BiVO_4$ Thin Film Photoanodes: A time-Resolved Microwave Conductivity. *J Phys Lett* 4: 2752–2757.

30. Mills A, Lee S-K (2003) Platinum group metals and their oxides in semiconductor photosensitization. *Platin Met Rev* 47(1): 2-12.

31. Maeda K, Teramura K, Domen K (2008) Effect of post-calcination on photocatalytic activity of $(Ga_{1-x}Zn_x)(N_{1-x}O_x)$ solid solution for overall water splitting under visible light. *J Catal* 254(2): 198-204.

32. Yin WJ, Wei SH, Al-Jassim MM, Turner J, Yan Y (2011) Doping properties of monoclinic BiVO4 studied by first-principles density-functional theory. *Phys Rev B - Condens Matter Mater Phys* 83(15): 1–11.

33. Kuhn HJ, Braslavsky SE, Schmidt R (2004) Chemical actinometry (IUPAC technical report). *Pure Appl Chem* 76(12): 2105-2146.

34. Montalti M, Credi A, Prodi L, Gandolfi MT (2006) Chemical Actinometry. *Handbook of Photochemistry* (Taylor & Francis Group LLC, Florida), 3rd Ed, pp 601-616.

35. Sasaki Y, Iwase A, Kato H, Kudo A (2008) The effect of co-catalyst for Z-scheme photocatalysis systems with an Fe^{3+}/Fe^{2+} electron mediator on overall water splitting under visible light irradiation. *J Catal* 259(1): 133-137.

36. Cullity BD (1978) Structure of Polycrystalline Aggregates. *Elements of X-ray diffraction* (Addison-Wesley, Massachusetts), 2nd Ed, pp 281-323.

37. Burton AW, Ong K, Rea T, Chan IY (2009) On the estimation of average crystallite size of zeolites from the Scherrer equation: A critical evaluation of its application to zeolites with one-dimensional pore systems. *Microporous Mesoporous Mater* 117(1-2): 75-90.

38. Williamson GK, Hall WH (1953) X-ray line broadening from filed aluminium and wolfram. *Acta Metallurgica* 1(1): 22-31.

CHAPTER FIVE

Conclusions

5.1. Findings from each chapter

Chapter 2: Photovoltaic Effect by Vapor-Printed Polyselenophene

In this work, we have successfully integrated polyselenophene donor layers into organic photovoltaic devices (OPVs) for the first time. By using oxidative chemical vapor deposition (oCVD), polyselenophene thin films are simultaneously synthesized and deposited at modest vacuum on various substrates without solubility, temperature, and substrate considerations. Bilayer heterojunction photovoltaic cells fabricated with the oCVD polyselenophene donor layers resulted in efficiencies up to 0.4%. This is the highest efficiency to date achieved by polyselenophene. In addition, this work investigates polyselenophene's nature closely linked to organic electronics for the first time. For example, we have illuminated polyselenophene's HOMO and LOMO levels as well as regiochemical defect generation mechanism.

Chapter 3: Oxidative Chemical Vapor Deposition of Neutral Hole Transporting Polymer for Enhanced Solar Cell Efficiency and Lifetime

This work represents the first example to realize the concept of a neutral hole transporting polymer, which is promising for achieving enhanced solar cell efficiency and lifetime. oCVD unlocks the potential of poly(3,4-dimethoxythiophene) (PDMT) in organic electronics by securing a solvent-free facile path to fabricate conformally patterned PDMT thin films on a wide range of substrates for the first time. The oCVD-processed PDMT hole transporting layer (HTL) exhibits the highest reported short-circuit current density (J_{SC}), fill factor (FF), and power conversion efficiency (PCE) of single-bilayer DBP/C_{60} solar cells as a result of its good conductivity, high transparency, appropriate energy levels, and neutrality. oCVD PDMT coating's conformal and dry nature with anion dopant injection capability creates a hole

transport-favorable interface, minimizing dipoles/carrier traps, scattering effects, interfacial energy barrier, dewetting defects, carrier recombination, and thus leakage currents. Consequently, the high-quality ohmic contact with minimized R_S and maximized R_{Sh} is formed between DBP and ITO, to upgrade the J_{SC}, FF, and PCE.

Chapter 4: Phase Transition Induced Band-edge Engineering of BiVO4 to Split Pure Water under Visible Light

In Chapter 4, We have discovered a novel visible light-responsive OWS photocatalyst through one-step photoexcitation by In^{3+}/Mo^{6+} dual doping into the host lattice of monoclinic $BiVO_4$. The resulting 'greenish' BiVO4 has an up-shifted conduction band edge transforming (only) O_2-evolving yellow $BiVO_4$ photocatalyst into (both) H_2/O_2-evolving OWS photocatalyst. The density functional theory calculation indicates that dual doping induces partial phase transition from pure monoclinic-$BiVO_4$ to a mixture of monoclinic and tetragonal $BiVO_4$, which accompanies increased unit cell volume, compressive lattice-strain increase, and lifted conduction band edge as observed experimentally. The greenish $BiVO_4$ is an active and stable one-photon OWS photocatalyst made of earth-abundant elements working in pure water without any additives.

5.2 Concluding remarks

In conclusion, oCVD is capable of printing a variety of conjugated polymers. The versatility of oCVD makes it a promising technique for surface modification as well as device fabrication. In this research, we were able to fabricate polyselenophene donor layers and neutral PDMT hole transporting layers, and integrate them into organic photovoltaics for the first time, by using

oCVD. As a result, we elucidated the impact of regiochemical defects in vapor-deposited polymers on the performance of OPVs, and created a new neutral hole transporting polymer (PDMT) as a suitable alternative to acidic commercial one (PEDOT:PSS). We will be able to take advantage of oCVD-conjugated polymers for perovskite solar cells and other electronic applications, as discussed in the following chapter.

5.3. Potential future work

The direction of potential future work can be described in two ways as follows.

5.3.1. N-type Semiconducting Polymers for Perovskite Solar Cells

Perovskite solar cells attract a great attention as a new emerging technology to convert sunlight energy into electricity with high PCE. Perovskite solar cells employ methyl-ammonium lead halides and TiO_2 as donor and acceptor, respectively. However, the LUMO level of TiO_2 is not high enough to maximize the PCE, and the intrinsic defects in TiO_2 are detrimental to their stability. To resolve this issue, high LUMO level n-type semiconducting polymers can be synthesized in the nanostructured thin-film form using oCVD, and applied to perovskite solar cells as brand-new acceptor materials. Subsequently, the interfacial properties of the n-type semiconducting polymers will be studied and optimized by constructing bulk-heterojunction via the co-deposition of controlling of methyl-ammonium lead halides and n-type polymers.

5.3.2. Polymer Structure Engineering for Thermoelectric Devices and Organic Field-Effect Transistor (OFET)

In order to simultaneously enhance the charge carrier mobility and reduce thermal conductivity in polymer thin films, polymer structure engineering will be accomplished by modulating the

polymer's size, geometry, and process history. Moreover, this work will be focused on developing a novel method to connect the thermoelectric properties and nanostructured morphology of polymers by taking advantage of oCVD, X-ray diffraction spectroscopy, and high-resolution microscopy. If the resulting amorphous polymer films exhibit high charge carrier mobility and low thermal conductivity at the same time, they will be uniquely exploited to realize high-efficiency thermoelectric devices for conversion of waste heat to electricity and temperature control. However, if they have only high charge carrier mobility, they can be used for making high-performance OFET.